Department of Physics and Astronomy

University of Heidelberg

Master thesis

in Physics

submitted by

Simon Stemmle

born in Heidelberg

September 2015

Measurement of the time-integrated CP asymmetry in prompt $D^0 \to K^-K^+$ decays with the LHCb experiment

This Master thesis has been carried out by

Simon Stemmle

at the

Physikalisches Institut Heidelberg

under the supervision of

Prof. Dr. Ulrich Uwer

and

Dr. Evelina Gersabeck

Abstract

This thesis presents a measurement of the time-integrated CP asymmetry in the Cabibbo-suppressed decay $D^0 \to K^-K^+$. For this study, the full data sample of proton-proton collisions, recorded with the LHCb experiment is used, corresponding to an integrated luminosity of $3\,\text{fb}^{-1}$. The data was recorded in 2011 and 2012 at a centre-of-mass energy of 7 TeV and 8 TeV, respectively. The D^0 mesons used for this analysis originate from the decays $D^{*+} \to D^0\pi^+$ and $D^{*-} \to \overline{D}^0\pi^-$. Thereby, the flavour of the neutral charm meson at production is determined by the charge of the pion. In order to evaluate the additional production and detection asymmetry arising from the D^{*+} meson and the pion, three Cabibbo-favoured charm meson decays are used as calibration channels. In these channels, CP violation is assumed to be negligible. In order to extract the raw asymmetries present in each of the four channels, simultaneous binned maximum likelihood fits are performed to the two flavour categories. By combining the measured raw asymmetries, the time-integrated CP asymmetry is found to be:

$$A_{CP}(K^-K^+) = (0.08 \pm 0.16(stat) \pm 0.11(syst))\%.$$

This result is consistent with the hypothesis of no CP violation and with the value measured in a previous LHCb analysis, $A_{CP}(K^-K^+) = (-0.06 \pm 0.15(stat) \pm 0.10(syst))\%$, using semileptonic b-mesons.

Kurzfassung

In dieser Arbeit wird eine Messung der zeitintegrierten CP-Asymmetrie in dem Cabibbo-unterdrückten Zerfall $D^0 \to K^-K^+$ vorgestellt. Hierfür wird der komplette Datensatz aus Proton-Proton Kollisionen, der einer integrierten Luminosität von $3\,\text{fb}^{-1}$ entspricht und mit LHCb Experiment aufgezeichnet wurde, benutzt. Diese Daten wurde in den Jahren 2011 und 2012 bei einer Schwerpunktsenergie von 7 TeV beziehungsweise 8 TeV aufgezeichnet. Die für diese Analyse verwendeten D^0 Mesonen stammen aus den Zerfällen $D^{*+} \to D^0\pi^+$ und $D^{*-} \to \overline{D}^0\pi^-$. Dadurch ist der anfängliche Flavour durch die Ladung des Pions bestimmbar. Um die zusätzliche Produktions- und Detektionsasymmetrie, welche durch das D^{*+} Meson und das Pion entstehen, auszuwerten, werden drei Cabibbo-bevorzugte D-Meson-Zerfälle als Kalibrationskanäle benutzt. Es wird angenommen, dass in diesen Zerfällen CP-Verletzung vernachlässigbar ist. Mithilfe von simultanen gebinnten Maximum Likelihood Fits an beide Flavour-Kategorien, wird die rohe Asymmetrie aller vier Zerfallskanäle bestimmt. Durch die Kombination dieser gemessenen Asymmetrien, wird die zeitintegrierte CP-Asymmetrie berechnet:

$$A_{CP}(K^-K^+) = (0.08 \pm 0.16(stat) \pm 0.11(syst))\%.$$

Dieses Ergebnis stimmt mit der Hypothese keiner CP-Verletzung und dem Wert einer früheren Analyse, $A_{CP}(K^-K^+) = (-0.06 \pm 0.15(stat) \pm 0.10(syst))\%$, welche semileptonische Zerfälle von B-Mesonen benutzt, überein.

Contents

Chapter 1

Introduction

Although the fundamental theory of elementary particles and their interactions was developed decades ago, this Standard Model (SM) of particle physics has withstood nearly all experimental tests. With the electromagnetic, the weak and the strong force it combines three fundamental interactions. For a long time, the only particle predicted by the SM but not observed was the Higgs boson which belongs to the mechanism of electroweak symmetry breaking. The discovery of this Higgs boson in 2012 completed the picture of the SM [1],[2].

Despite its tremendous success, there are several phenomena in nature that are not described by the SM. The large matter-antimatter asymmetry of the universe and the presence of dark energy and dark matter are such phenomena. Also gravity which is the fourth fundamental interaction can not be described by the SM. Therefore, the search for new physics in the sector of fundamental particle physics is a central and necessary step towards a better understanding of nature.

The Large Hadron Collider (LHC) is at the moment the largest and most powerful proton-proton collider. Direct searches for new particles being produced in these collisions is one possibility to search for physics beyond the SM. The LHCb experiment uses the particles produced at the LHC for an alternative indirect way of searching for new physics. These indirect searches are based on the influence of new heavy particles which are introduced via quantum loops on quantities like decay rates or lifetimes. LHCb is specialised on precise measurements of processes with hadrons containing b- and c-quarks which are likely to be affected by physical processes beyond the SM. The charge-parity (CP) asymmetry describes the difference between the behaviour of particles and anti-particles. To first order, the SM is symmetric under CP transformation. Therefore, observables related to this asymmetry are very sensitive to quantum corrections due to new physics, and are therefore precisely measured. An example of such an observable is the asymmetry A_{CP} of decay rates. Whereas sizeable CP asymmetry was measured in the kaon and b-hadron system, it is expected to be very small for hadrons containing a c-quark. Thus, precise measurements in the charm sector constitute a powerful way of probing physics effects beyond the SM.

In the past, the LHCb collaboration published a first evidence for a non-zero difference, ΔA_{CP}, of the time-integrated CP asymmetries of the decays $D^0 \to K^-K^+$ and $D^0 \to \pi^-\pi^+$ [3]. Although a new measurement using an independent data-set

does not confirm this evidence [4], further studies are still ongoing. The topic of this thesis is the measurement of the time-integrated CP asymmetry $A_{CP}(K^-K^+)$ of the decay $D^0 \to K^-K^+$. This quantity is more sensitive to indirect CP violation than ΔA_{CP}, but it is experimentally more challenging to measure. In order to determine $A_{CP}(K^-K^+)$, there are several nuisance detection and production asymmetries which have to be taken into account by combining different additional charm meson decays.

For this measurement, D^0 mesons originating from prompt $D^{*+} \to \pi^+ D^0$ decays are used. The charge of the pion is used to determine the flavour of the neutral charm meson at production. Together with an ongoing LHCb analysis which measures ΔA_{CP} using the same prompt charm datasets, the value obtained by this thesis can be combined to measure the asymmetry $A_{CP}(\pi^-\pi^+)$. These three values are important to extract CP violation parameters in the charm system.

The quantity $A_{CP}(K^-K^+)$ was already measured by the LHCb collaboration using data collected in 2011 and 2012 [4]. There, semileptonic B-meson to D-meson decays were used to determine the flavour of the $D^0(\overline{D}^0)$ mesons. Thus, this thesis presents a complementary measurement of $A_{CP}(K^-K^+)$. Anyhow, the methods developed for the analysis of the semileptonic data which are presented in detail in [5], can be analogously applied the the prompt charm dataset. This includes for example the usage of similar calibration channels in order to cancel the nuisance detection and production asymmetries.

This thesis is organized as follows: In chapter 2 and 3 the theory of CP violation in the charm sector and the LHCb experiment are introduced. Chapter 4 provides an overview of the analysis and chapter 5 presents the occurring nuisance asymmetries and the analysis strategy. The selection requirements for all used decay channels are presented in chapter 6. In order to extract the asymmetries, binned likelihood fits are performed, which are presented in chapter 7. A crucial aspect of this analysis is the weighting of kinematic distributions of the individual channels which is discussed in detail in chapter 8. After that, the asymmetry of neutral kaons, which is relevant for one of the calibration channels, is calculated in chapter 9. The values for all measured asymmetries are presented in chapter 10. In chapter 11, several systematic studies are performed to estimate possible biases of the main result. Finally, a summary and a discussion of the results can be found in chapter 12.

Chapter 2

Theory

This chapter provides a short introduction into the theory of *CP* violation in the neutral charm meson system. Firstly, the SM of particle physics and especially the flavour changing charged currents of the weak interaction are presented. This leads to the discussion of neutral meson mixing and possible *CP* violation in these systems. Since it is an important part of this thesis to correct for possible detector asymmetries, this chapter concludes with a short discussion on asymmetries in material interactions.

2.1 Standard Model

The SM of particle physics[1] is the most successful approach to describe all elementary particles and their interactions. It is able to describe nearly all observed phenomena in this field. High precision tests of the SM predictions are the experimental foundations of the modern particle physics. The SM is a quantum field theory and the fundamental interactions between the particles are described by requiring it to be invariant under the local gauge transformation of $\mathrm{SU}(3)\otimes\mathrm{SU}_L(2)\otimes\mathrm{U}(1)$. These symmetries generate the three fundamental interactions: electromagnetic, weak and strong. Gravity, as the fourth known fundamental interaction is not described.

The SM classifies the elementary particles into bosons and fermions. All so called matter fields or particles of the SM are fermions with spin 1/2. They can be divided into quarks and leptons, which both come in three families or generations. For the leptons, each family consists out of a charged particle (e^-, μ^- and τ^-) and its neutrino (ν_e, ν_μ and ν_τ). The quarks build families of an up-type quark (u, c, t) with charge $+2/3e$ and an down-type quark (d, s, b) which have an electric charge of $-1/3e$. Figure 2.1 shows this structure of the fermions on the left side. For each fermion, its corresponding anti-particle is also part of the standard model.

All matter fields have their specific charges under each of the symmetry transformations. According to these charges, they couple to the so called gauge bosons which are the generators of the symmetry groups. These bosons are spin 1 particles and are also listed in figure 2.1. The electroweak interaction is generated by $\mathrm{SU}_L(2)\otimes\mathrm{U}(1)$ and splits up into a weak and an electromagnetic part. The massless

[1] For a introduction to the Standard Model see for example [6].

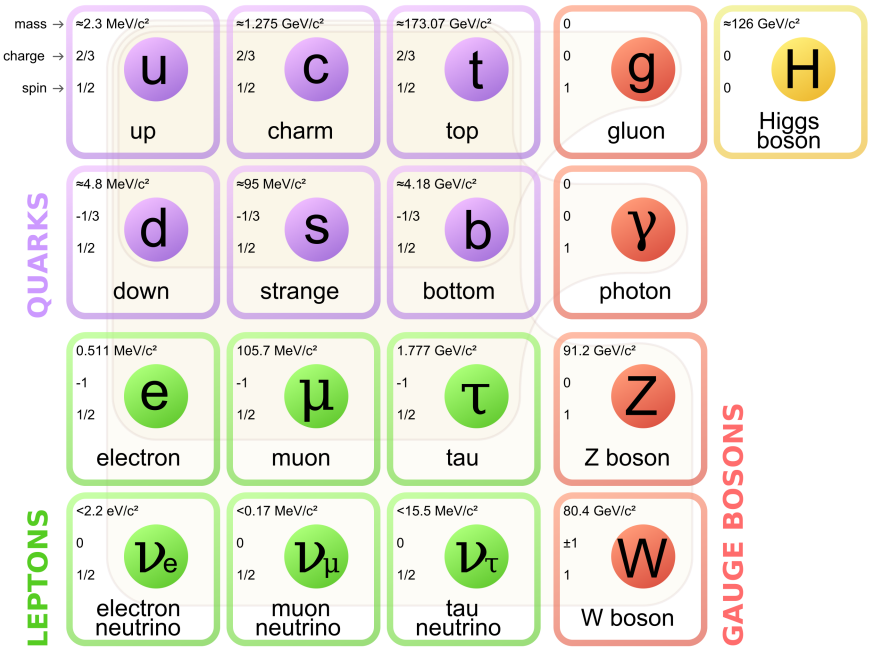

Figure 2.1: Elementary fermions and bosons of the standard model. Figure taken from Ref. [7].

photon is the mediating particle of the electromagnetic interaction and couples to all particles with an electric charge. There are three more electroweak gauge bosons, W^+, W^- and Z which represent the weak interaction and are massive. Additionally, the SU(3) group generates the strong interaction which is propagated by eight massless bosons called gluons. The three charges of the strong interaction are called colors.

The gluons and therefore the strong interaction couples only to coloured objects. Beside the gluons themselves, only quarks carry a color. A crucial property of the strong force is the so called confinement. This effect describes the fact that the strong force becomes infinitely large at large distances. Therefore, only colourless bound systems of several quarks, called hadrons, can exist independently. A quark can form together with an antiquark of opposite charge a meson. Baryons are colorless systems of three quarks. Recently also observations consistent with exotic hadrons consisting out of four quarks and an antiquark or out of two quarks and two antiquarks were made at the LHCb experiment [8], [9].

The weak interaction couples to all matter fields but discriminates between left-handed and right-handed particles. As indicated by the name, the weak interaction is by orders of magnitude weaker than the strong force or the electromagnetic force. This is the reason for the relatively long lifetime of particles which can only decay via a weak process.

Another important part of the SM is the Higgs-mechanism. It is essential for the SM as it explains the generation of the masses of the matter field and the weak gauge

bosons. Via symmetry breaking and the introduction of an additional scalar field, a new particle, the Higgs boson is introduced. The coupling to this new field and therefore also to the Higgs boson is proportional to the thereby generated masses. Besides the neutrinos, gluons and the photon which are massless, all fermions and bosons in the SM acquire their masses via this mechanism.

Despite the great success of the SM it cannot explain some fundamental aspects of our universe. For example it lacks a candidate for the dark matter, which accounts for approximately 26% of the whole energy content of the universe [10].

2.2 Charged currents of the weak interaction

The charged currents of the weak interaction are of special interest when talking about CP violation. In this section, a general theoretical introduction[2] is followed by a more specific description of weak charged currents in the charm meson system.

Lagrangian and CKM mechanism

The gauge bosons W^+ and W^- mediate the charge and flavour changing currents of the weak interaction. Their coupling to the fermions is described by the following part of the SM Lagrangian:

$$\mathcal{L} = -\frac{g}{2\sqrt{2}}\left[\sum_i W_\mu^+ \overline{\phi_i^u}\gamma^\mu(1-\gamma^5)\phi_i^d + \sum_i W_\mu^- \overline{\phi_i^d}\gamma^\mu(1-\gamma^5)\phi_i^u\right]. \tag{2.1}$$

Here, g is the coupling constant of the $\mathrm{SU}(2)_L$ gauge group and ϕ^u/ϕ^d are the fields of up and down type quarks or leptons:

$$\phi^u = \begin{pmatrix} u' \\ c' \\ t' \end{pmatrix}, \phi^d = \begin{pmatrix} d' \\ s' \\ b' \end{pmatrix} \quad or \quad \phi^u = \begin{pmatrix} \nu_e \\ \nu_\mu \\ \nu_\tau \end{pmatrix}, \phi^d = \begin{pmatrix} e^- \\ \mu^- \\ \tau^- \end{pmatrix}. \tag{2.2}$$

γ^μ and γ^5 are the Dirac matrices and the operator $1/2(1-\gamma^5)$ projects out the left-handed part of the fermion fields. This reflects that $\mathrm{SU}(2)_L$ gauge bosons, and therefore also the W-bosons, couple only to left-handed quarks and leptons and right handed antiquarks and anti-leptons.

So far, the quarks are given as electroweak eigenstates (u_i', d_i') which do not have to be the same as the mass eigenstates. After symmetry breaking, the quarks and charged leptons obtain their mass via the Higgs-mechanism. Neutrino masses are ignored at this point, since they are not relevant for this study. The quark mass eigenstates (u_i, d_i) are then given by mixtures of the interaction eigenstates. In the

[2] An introduction to the electroweak sector of the SM can be found in [11].

weak interaction this is reflected by a unitary matrix V when writing the Lagrangian in terms of mass eigenstates:

$$\mathcal{L}_{quark} = -\frac{g}{2\sqrt{2}} \left[\sum_{i,j} W_\mu^+ \overline{u_i} \gamma^\mu (1-\gamma^5) V_{ij} d_j + \sum_{i,j} W_\mu^- \overline{d_j} \gamma^\mu (1-\gamma^5) V_{ij}^\dagger u_i \right]. \quad (2.3)$$

By convention, the up-type quarks are chosen to be the same in both bases:

$$u_i^{'} = u_i. \quad (2.4)$$

For the down-type quarks the two bases are related via:

$$d_i^{'} = \sum_j V_{ij} d_j. \quad (2.5)$$

The matrix V is called Cabibbo-Kobayashi-Maskawa matrix (V_{CKM}) [12] and is discussed in more detail in this chapter.

Now, this Lagrangian is used to introduce the concepts of parity and charge transformation. The Parity operator P flips the spacial coordinates:

$$P\overrightarrow{x} = -\overrightarrow{x}. \quad (2.6)$$

Objects like $\overline{\phi}\gamma^\mu\phi$ also change sign and therefore transform as vector under parity transformation. Adding an additional γ^5 changes the transformation behaviour which is why $\overline{\phi}\gamma^\mu\gamma^5\phi$ transforms as axial vector and flips no sign. This reflects the V-A structure of the weak interaction which maximally violates parity. Also under charge transformation (C), which flips all charge-like quantum numbers, the vector and axial vector parts obtain a relative minus sign. Therefore, C is also maximally violated. From equation 2.3 one can derive that the combination of C and P (CP) can only be violated if $V_{CKM} \neq V_{CKM}^\dagger$.

The CKM mechanism represented by the CKM-matrix allows for transitions between different quark generations. These transitions are described by the elements of V_{CKM}:

$$\begin{pmatrix} d^{'} \\ s^{'} \\ b^{'} \end{pmatrix} = \begin{pmatrix} V_{ud} & V_{us} & V_{ub} \\ V_{cd} & V_{cs} & V_{cb} \\ V_{td} & V_{ts} & V_{tb} \end{pmatrix} \begin{pmatrix} d \\ s \\ b \end{pmatrix}. \quad (2.7)$$

Since the matrix is unitary, it has nine free parameters, but by absorbing unobservable phases of the quark fields this number is reduced to four. Three of these parameters are rotation angles and one is a complex phase which leads to $V_{CKM} \neq V_{CKM}^\dagger$ and is the only source of CP violation occurring in the SM. A useful parametrization of the CKM matrix was given by Wolfenstein [13]:

$$V_{CKM} = \begin{pmatrix} 1-\frac{1}{2}\lambda^2 & \lambda & A\lambda^3(\rho - i\eta) \\ -\lambda & 1-\frac{1}{2}\lambda^2 & A\lambda^2 \\ A\lambda^3(1-\rho-i\eta) & -A\lambda^2 & 1 \end{pmatrix} + \mathcal{O}(\lambda^4), \quad (2.8)$$

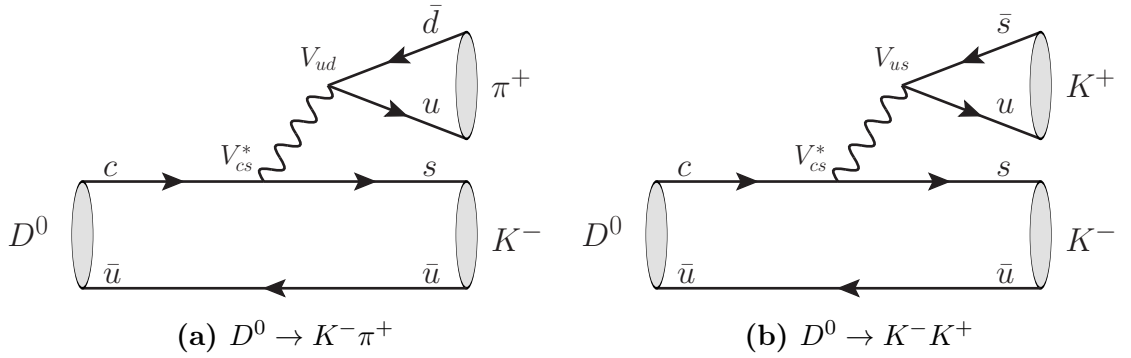

(a) $D^0 \to K^-\pi^+$ **(b)** $D^0 \to K^-K^+$

Figure 2.2: Lowest order Feynman diagrams of D^0 meson decays to two body final states relevant for this analysis.

where $\lambda \approx 0.23$, is the sine of the rotation angle between the first two generations. The other parameters are of order $0.1 - 1$. In this parametrization, one can directly see the nearly diagonal structure of the matrix which is the reason for suppressed transitions between different quark families. This effect is called Cabibbo-suppression and examples follow when discussing the charm meson decays. Up to $\mathcal{O}(\lambda^4)$, the only elements with a non-zero complex phase are V_{ub} and V_{td} which are the furthest away from the diagonal. Therefore, any kind of CP-violating effect is expected to be small in the SM.

Charm Mesons

All mesons which contain a charm quark as its heaviest parton are summarized as charm mesons. For this analysis, only charm mesons which contain a second quark out of the first generation are of interest. The ground states are then given by the mesons D^0 ($c\overline{u}$), $\overline{D}^0$ ($\overline{c}u$), D^+ ($c\overline{d}$) and D^- ($\overline{c}d$). As there are no lighter particles containing a charm quark, all these mesons decay via the weak interaction.

The neutral charm mesons D^0 and $\overline{D}^0$ mostly decay to a kaon and other lighter mesons. The decay $D^0 \to K^-\pi^+(\overline{D}^0 \to K^+\pi^-)$[3] is one of the most probable decays of the neutral charm meson. Figure 2.2a depicts the tree-level process for this decay and its measured branching ratio is $(3.88 \pm 0.05) \times 10^{-2}$ [11]. Since no transition between different quark families is necessary, this decay is called **Cabibbo-favoured**. The decays to a symmetric final state like $D^0 \to K^-K^+$ or $D^0 \to \pi^-\pi^+$ contain a $(u \leftrightarrow s)$ or $(c \leftrightarrow d)$ transition and are therefore **singly Cabibbo-suppressed**. Their branching ratios are measured to be $(3.96 \pm 0.08) \times 10^{-3}$ for the decay $D^0 \to K^-K^+$ and $(1.402 \pm 0.026) \times 10^{-3}$ for the decay $D^0 \to \pi^-\pi^+$ [11]. The tree-level Feynman diagram of the decay relevant for this analysis, $D^0 \to K^-K^+$, is shown in figure 2.2b. There are also **doubly Cabibbo-suppressed** decays like $D^0 \to K^+\pi^-$ which are not relevant for this analysis.

The charged charm meson D^+ also most commonly decay into a kaon and one or

[3] CP conjugated decays are always implied in the following if not stated otherwise.

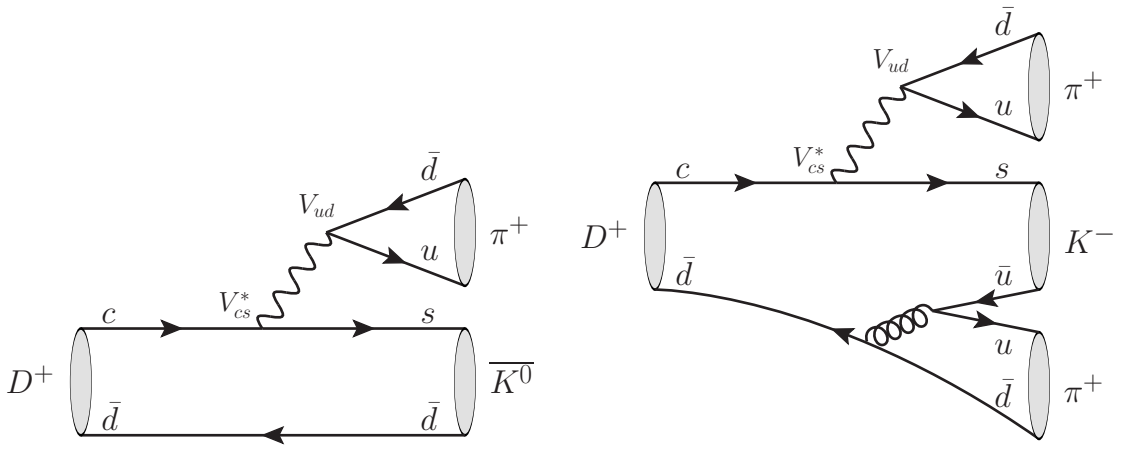

(a) $D^+ \to \overline{K}^0\pi^+$ **(b)** $D^+ \to K^-\pi^+\pi^+$

Figure 2.3: Lowest order Feynman diagrams of, for this analysis relevant, D^+ decays.

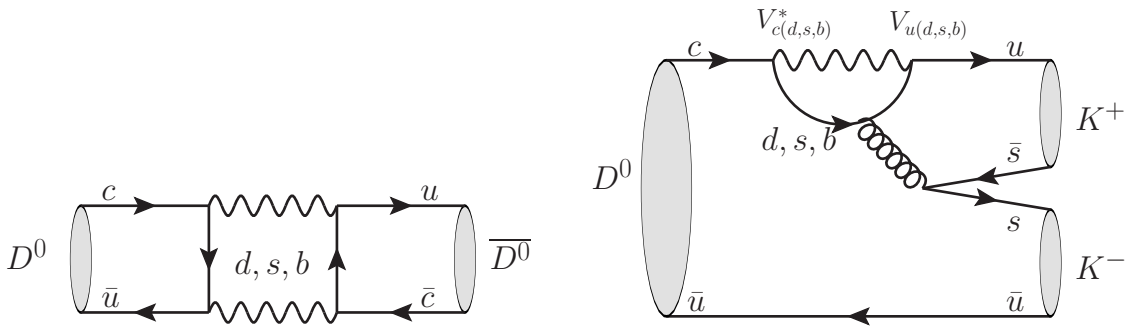

(a) $D^0 \leftrightarrow \overline{D}^0$ box-diagramm. **(b)** Penguin diagram for $D^0 \to K^-K^+$.

Figure 2.4: Higher order Feynman diagrams in the neutral charm meson system.

more pions. For this study, the decay channels $D^+ \to K^-\pi^+\pi^+$ and $D^+ \to \overline{K}^0\pi^+$ are used for calibration purposes. Figure 2.3 shows the lowest order Feynman diagrams for these decays. They both contain $(c \leftrightarrow s)$ transitions and are Cabibbo-favoured.

Beside the already described tree-level decays, there are two more processes which are needed for the description of CP violation in D^0 decays. The first is the **mixing** between D^0 and $\overline{D}^0$ mesons. There are two ways how a D^0 meson can transform into its antiparticle and both include weak charged currents. Diagram 2.4a shows one possible so-called box-diagram. Since there occur no on-shell intermediate states, this process is also referred to as the short distance part of the D^0 meson mixing. Due to the GIM-mechanism [14] suppression, the contributions from the down and strange quarks in the box-diagram mostly cancel. The contribution from the bottom quark is strongly suppressed by $|V_{cb}|\,|V_{ub}| \propto \lambda^5$. The transition from a D^0 meson to a $\overline{D}^0$ meson can also happen via an on-shell state which is a common final state of both, D^0 and $\overline{D}^0$ mesons. This process is then called the long range part and is

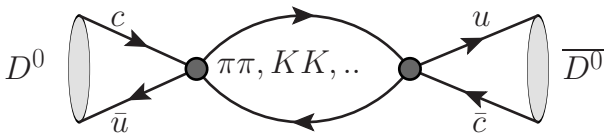

Figure 2.5: Schematic Feynman diagram for the transition between D^0 and $\overline{D}^0$ mesons via on-shell states.

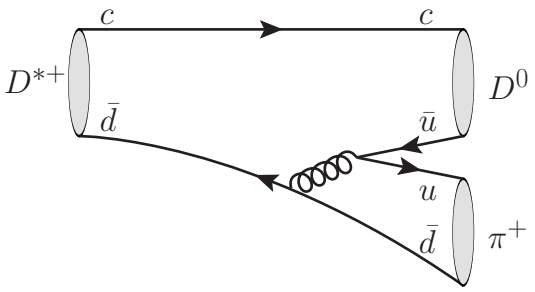

Figure 2.6: Feynman diagram of the strong decay of the excited charged charm meson: $D^{*+} \to D^0\pi^+$.

pictured in figure 2.5. The above mentioned states K^-K^+ and $\pi^-\pi^+$ are examples for such intermediate particles.

Processes of higher order, like **penguin decays** are the second type of processes which can generate CP violation. Taking only the above mentioned tree-level decays into account, any phase of the occurring V_{CKM} elements would cancel in the final decay rate. Differences between D^0 and $\overline{D}^0$ decays need therefore interference with higher order processes which lead to the same final state. Figure 2.4b shows such a penguin contribution which is highly Cabibbo-suppressed. The contributions of diagrams with a down or a strange quark in the loop are again cancelled by the GIM-mechanism.

For this analysis, the excited D^{*+} is another important charm meson. The strong decay $D^{*+} \to D^0\pi^+$ has a measured branching ratio of 0.677 ± 0.005 [11] and it is the origin of all neutral charm mesons used for this analysis. Figure 2.6 shows the relevant tree-level Feynman diagram. Since the mass difference between the D^{*+} and the D^0 meson is only $145.4\,\mathrm{MeV}/c^2$ and the charged pion has a mass of $139.5\,\mathrm{MeV}/c^2$, the latter is hereafter also called a slow pion. Its charge is used to determine the flavour of the $D^0/\overline{D}^0$ mesons at production.

2.3 Neutral meson phenomenology

In the following section the phenomenology of neutral meson mixing and CP violation in such systems is discussed[4]. Although the focus lies on the charm mesons, the presented formalism is valid for other neutral mesons.

2.3.1 Mixing

The neutral charm mesons, D^0 and $\overline{D}^0$, as introduced above, are flavour eigenstates and therefore eigenstates of the strong and electromagnetic interaction. In contrast, the presence of box diagrams like in figure 2.4a shows that transitions between the flavour states are possible via the weak interaction. This means that they are no eigenstates of the weak interaction. Therefore, the physical mass eigenstates of the full effective Hamiltonian are a mixture of D^0 and $\overline{D}^0$ states: $|\Psi(t)\rangle = a(t)\,|D^0\rangle + b(t)\,|\overline{D}^0\rangle$.

The full effective Hamiltonian, as any complex matrix, can be written as

$$\boldsymbol{H} = \boldsymbol{M} - \frac{i}{2}\boldsymbol{\Gamma}, \tag{2.9}$$

where $\boldsymbol{M}$ and $\boldsymbol{\Gamma}$ are 2x2 hermitian matrices. This leads to the following Schrödinger equation:

$$i\frac{d}{dt}\begin{pmatrix} a(t) \\ b(t) \end{pmatrix} = \left(\boldsymbol{M} - \frac{i}{2}\boldsymbol{\Gamma}\right)\begin{pmatrix} a(t) \\ b(t) \end{pmatrix}. \tag{2.10}$$

The off-diagonal elements of $\boldsymbol{M}$ and $\boldsymbol{\Gamma}$ represent ($D_0 \leftrightarrow \overline{D}^0$) transitions via off-shell (short distance, figure 2.4a) and on-shell (long distance, figure 2.5) processes, respectively. The eigenstates are typically labelled according to their mass as D^0_H (heavy) and D^0_L (light) which have the masses M_H,M_L and total decay widths Γ_H,Γ_L:

$$|D^0_H\rangle = p\,|D^0\rangle + q\,|\overline{D}^0\rangle\,, \tag{2.11}$$

$$|D^0_L\rangle = p\,|D^0\rangle - q\,|\overline{D}^0\rangle\,, \tag{2.12}$$

with

$$\left(\frac{q}{p}\right)^2 = \left(\frac{M^*_{12} - \frac{i}{2}\Gamma^*_{12}}{M_{12} - \frac{i}{2}\Gamma_{12}}\right)^2. \tag{2.13}$$

They evolve in time as:

[4]This chapter is based on Ref. [11] and [15].

$$|D^0_{H/L}(t)\rangle = e^{-iM_{H/L}t-\Gamma_{H/L}t/2}\,|D^0_{H/L}\rangle\,. \tag{2.14}$$

Important quantities describing the mixing behaviour are

$$\Delta m = M_H - M_L, \qquad m = \frac{M_H + M_L}{2}, \tag{2.15}$$

$$\Delta\Gamma = \Gamma_H - \Gamma_L, \qquad \Gamma = \frac{\Gamma_H + \Gamma_L}{2}, \tag{2.16}$$

and especially

$$x = \frac{\Delta m}{\Gamma}, \qquad y = \frac{\Delta\Gamma}{2\Gamma}. \tag{2.17}$$

Using these variables, and the equations 2.14, 2.11 and 2.12, one can derive the time evolution of the two flavour eigenstates [16]:

$$|D^0(t)\rangle = g_+(t)\,|D^0\rangle + \frac{q}{p}g_-(t)\,|\overline{D}^0\rangle\,, \tag{2.18}$$

$$|\overline{D}^0(t)\rangle = \frac{p}{q}g_-(t)\,|D^0\rangle + g_+(t)\,|\overline{D}^0\rangle\,. \tag{2.19}$$

Where $g_+(t)$ and $g_-(t)$ are given by:

$$g_+(t) = e^{-imt}e^{-\Gamma t/2}\left(\quad \cosh\frac{y\tilde{\tau}}{2}\cos\frac{x\tilde{\tau}}{2} - i\sinh\frac{y\tilde{\tau}}{2}\sin\frac{x\tilde{\tau}}{2}\right), \tag{2.20}$$

$$g_-(t) = e^{-imt}e^{-\Gamma t/2}\left(-\sinh\frac{y\tilde{\tau}}{2}\cos\frac{x\tilde{\tau}}{2} + i\cosh\frac{y\tilde{\tau}}{2}\sin\frac{x\tilde{\tau}}{2}\right), \tag{2.21}$$

with $\tilde{\tau} = \Gamma t$. Given that a $D^0(\overline{D}^0)$ meson was produced at time $t = 0$, the probability that it has mixed to a $\overline{D}^0(D^0)$ meson after time t is given by:

$$\left|\langle\overline{D}^0|D^0(t)\rangle\right|^2 = \left|\frac{q}{p}\right|^2 |g_-(t)|^2 \tag{2.22}$$

$$\left|\langle D^0|\overline{D}^0(t)\rangle\right|^2 = \left|\frac{p}{q}\right|^2 |g_-(t)|^2 \tag{2.23}$$

$$|g_-(t)|^2 = \frac{e^{-\Gamma t}}{2}\left(\cosh y\tilde{\tau} - \cos(x\tilde{\tau})\right). \tag{2.24}$$

This shows on the one hand the oscillation between the two states, which strongly depends on the values of x and y. For the charm mesons both are of order 10^{-2} and, therefore, the oscillation is strongly suppressed. On the other hand, the mixing probability is not symmetric under CP conjugation if $\left|\frac{q}{p}\right| \neq 1$. This is called CP violation in mixing. Other categories are discussed in the following section.

2.3.2 CP violation in neutral meson systems

One can combine the above formalism with the decay of the neutral meson into the final state f. The four different decay amplitudes are given by:

$$A_f = \langle f|\mathcal{H}|D^0\rangle\,, \qquad \bar{A}_f = \langle f|\mathcal{H}|\overline{D}^0\rangle\,, \tag{2.25}$$

$$A_{\bar{f}} = \langle \bar{f}|\mathcal{H}|D^0\rangle\,, \qquad \bar{A}_{\bar{f}} = \langle \bar{f}|\mathcal{H}|\overline{D}^0\rangle\,. \tag{2.26}$$

Using these amplitudes the CP violation in neutral meson systems can be classified according to it's origin. **Direct CP violation** denotes the case that $\Gamma(D^0 \to f)$ is different from $\Gamma(\overline{D}^0 \to \bar{f})$, which is equivalent to

$$\left|\frac{A_f}{\bar{A}_{\bar{f}}}\right| \neq 1. \tag{2.27}$$

As mentioned in the previous section, **CP violation in mixing** describes the case that

$$\left|\frac{q}{p}\right| \neq 1 \tag{2.28}$$

and is independent of the final state f.

In case of D^0 and $\overline{D}^0$ decays to a common final state f, **CP violation in the interference** between the decays with and without mixing can occur. It is characterized by

$$\mathrm{Im}\lambda_f = \mathrm{Im}\left(\frac{q}{p}\frac{\bar{A}_f}{A_f}\right) \neq 0. \tag{2.29}$$

The simplest case for such a final state is a CP eigenstate where $f = \bar{f}$. $D^0 \to K^-K^+$ is such a decay to a CP even final state.

2.3.3 Formalism and Predictions for the neutral charm meson

Here, the above formalism is extended and used to describe CP violation in the neutral charm meson system.

For singly Cabibbo-suppressed decays of the D^0 meson, like the decay to K^+K^-, the tree-level contribution dominates the decay amplitude. Therefore, the amplitudes can be written as

$$A_f = A_f^T\left[1 + r_f e^{i\left(\delta_f + \phi_f\right)}\right], \tag{2.30}$$

$$\bar{A}_f = \eta_f^{CP} A_f^T\left[1 + r_f e^{i\left(\delta_f - \phi_f\right)}\right], \tag{2.31}$$

where A_f^T is the tree-level amplitude whose phase is chosen to be zero. r_f is the ratio between the higher order and tree-level contributions, while $\delta_f(\phi_f)$ describes the

weak(strong) phase difference between these contributions. η_f^{CP} is the CP eigenvalue of the final state which is 1 for $f = \pi^+\pi^-/K^+K^-$. According to figure 2.2b and 2.4b, r_f is proportional to $|V_{cb}^* V_{ub}/V_{cs}^* V_{us}^*|$ for $f = K^+K^-$ and, therefore, of order $\lambda^4 \approx 0.002$. Neglecting r_f, and assuming a CP-even final state, one can drop η_f^{CP} and λ_f becomes independent of the final state:

$$\lambda_f = -\left|\frac{q}{p}\right| e^{i\phi_D}, \tag{2.32}$$

with ϕ_D being the phase of q/p. Combining 2.18-2.21 and 2.25 yields:

$$\begin{aligned}\Gamma(D^0 \to f)(t) = e^{-\tilde{\tau}} |A_f|^2 \Big[&\left(1 + |\lambda_f|^2\right) \cosh x\tilde{\tau} + \left(1 - |\lambda_f|^2\right) \cos x\tilde{\tau} \\ &+2\mathrm{Re}(\lambda_f) \sinh y\tilde{\tau} - 2\mathrm{Im}(\lambda_f) \sin x\tilde{\tau}\Big],\end{aligned} \tag{2.33}$$

$$\begin{aligned}\Gamma(\overline{D}^0 \to f)(t) = e^{-\tilde{\tau}} \left|\bar{A}_f\right|^2 \Big[&\left(1 + \left|\lambda_f^{-1}\right|^2\right) \cosh x\tilde{\tau} + \left(1 - \left|\lambda_f^{-1}\right|^2\right) \cos x\tilde{\tau} \\ &+2\mathrm{Re}(\lambda_f) \sinh y\tilde{\tau} - 2\mathrm{Im}(\lambda_f) \sin x\tilde{\tau}\Big].\end{aligned} \tag{2.34}$$

In the $D^0 - \overline{D}^0$ mixing, the mixing parameters are measured to be $x = (0.37 \pm 0.16) \times 10^{-2}$ and $y = (0.66^{+0.07}_{-0.10}) \times 10^{-2}$ [17]. This means that mixing is strongly suppressed in this system. Since x, y, r_f are small, the above equations can be rewritten with equation 2.32 as:

$$\Gamma(D^0 \to f)(t) = |A_f|^2 e^{-[1+|q/p|(y\cos\phi_D - x\sin\phi_d)]\tilde{\tau}} = |A_f|^2 e^{-\hat{\Gamma}t}, \tag{2.35}$$

$$\Gamma(\overline{D}^0 \to f)(t) = \left|\bar{A}_f\right|^2 e^{-[1+|p/q|(y\cos\phi_D + x\sin\phi_d)]\tilde{\tau}} = \left|\bar{A}_f\right|^2 e^{-\hat{\bar{\Gamma}}t}. \tag{2.36}$$

This introduces the effective lifetimes $\hat{\Gamma}$ and $\hat{\bar{\Gamma}}$ of the D^0 and $\overline{D}^0$ mesons. The time dependent CP asymmetry

$$a_{cp}(t) = \frac{\Gamma(D^0 \to f)(t) - \Gamma(\overline{D}^0 \to f)(t)}{\Gamma(D^0 \to f)(t) + \Gamma(\overline{D}^0 \to f)(t)} \tag{2.37}$$

can then be split in the three parts of CP violation categories. The direct CP violation part is constant over time, whereas the CP violation due to mixing and interference depend linearly on it:

$$a_{cp}(t) = a_{cp}^{dir} + a_{cp}^{int}\tilde{\tau} + a_{cp}^{mix}\tilde{\tau}. \tag{2.38}$$

In this approximation, the CP violation in the decay,

$$a_{cp}^{dir} = 2r_f \sin\phi_f \sin\delta_f, \tag{2.39}$$

depends on the final state, whereas the interference and mixing parts,

$$a_{cp}^{int} = \frac{1}{2}\left(\left|\frac{q}{p}\right| + \left|\frac{p}{q}\right|\right) x \sin\phi_D, \tag{2.40}$$

$$a_{cp}^{mix} = -\frac{1}{2}\left(\left|\frac{q}{p}\right| - \left|\frac{p}{q}\right|\right) y \cos\phi_D, \tag{2.41}$$

are universal.

The angle ϕ and the ratio $\left|\frac{q}{p}\right|$ show so far no deviation from 0 and 1 [17]. Since also the mixing parameters x and y are small, the indirect CP violation is expected to be smaller than $\mathcal{O}(10^{-3})$. Also the direct CP violation, proportional to r_f, is naively expected to be of order $O(10^{-3})$ for the SM. Up to now, no precise theoretical predictions can be made whether this limit has to held for the SM. There are several effects potentially leading to enhanced penguin amplitudes, and further studies will have to be done to determine the amount of direct CP violation allowed in the SM [18].

In order to disentangle the direct and indirect asymmetries, the effective lifetime asymmetry

$$A_\Gamma = \frac{\hat{\Gamma} - \hat{\bar{\Gamma}}}{\hat{\Gamma} + \hat{\bar{\Gamma}}}, \tag{2.42}$$

and

$$\Delta A_{CP} = A_{CP}(D^0 \to K^- K^+) - A_{CP}(D^0 \to \pi^- \pi^+), \tag{2.43}$$

are combined [17]. Since the indirect part of the CP asymmetry is independent of the final state, it largely cancels for ΔA_{CP}. The direct CP asymmetry of $D^0 \to \pi^-\pi^+$ and $D^0 \to K^-K^+$ decays are expected to be of opposite sign and to have the same absolute value. Therefore, ΔA_{CP} is a good measure of the direct CP violation. In contrast to that, A_Γ is more sensitive to the indirect part.

The current world averages obtained in this way are [17]:

$$a_{CP}^{ind} = (0.058 \pm 0.040)\% \tag{2.44}$$

$$\Delta a_{CP}^{dir} = (-0.257 \pm 0.104)\%. \tag{2.45}$$

In the past there was a strong evidence for direct CP violation [19] which is now reduced by new measurements, as for example in [5].

2.4 Asymmetries in material interaction

In order to measure the above mentioned CP asymmetries, one has to take into account different sources of nuisance asymmetries. They are discussed in detail in chapter 5.1 but the theoretical background of an asymmetric interaction of final states particles with the detector is given here.

In general, there are different mechanisms how leptons and hadrons interact with a detector. Since in this analysis all final state particles are hadrons, only they are discussed. There are three different ways in which hadrons interact with material. In general, charged particles can loose part of their energy by colliding with electrons. The associated atoms get either excited or ionized. Instead of the interaction with electrons of the atomic shell, charged particles can change their trajectory as a

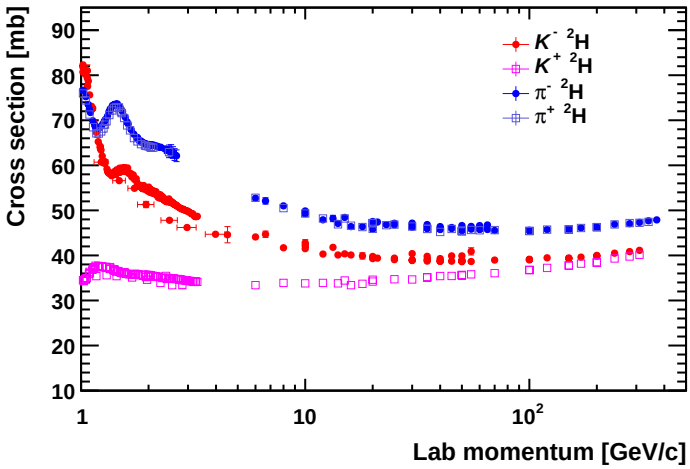

Figure 2.7: Charged kaon deuterium cross-section as a function of the laboratory momentum. The data are taken from the COMPAS Group [11].

result of the interaction with the nuclei. This can happen several times when a particle transverses material and is called multiple scattering. As a result of this, the direction of the momentum of the particle is changed which limits the possible momentum resolution of a detector.

Additionally, neutral, as well as charged, hadrons interact strongly with the detector. This can happen either elastically or inelastically. In contrast to the previously discussed types of interaction the latter can be asymmetric with respect to particles and their antiparticles. The LHCb detector contains approximately the same number of protons and neutrons. This means that there are the same number of up and down valence quarks. Beside these valence quarks, protons and neutrons contain also sea quarks which always appear as quark antiquark pairs. Positively and negatively charged pions have the quark content $(u\overline{d})$ and $(\overline{u}d)$, respectively. The $\overline{u}$- and $\overline{d}$-quarks can annihilate with the valence u- and d-quarks of the neutrons and protons of the detector. Since they occur in the same amount, the interaction of pions with the detector material is symmetric.

This is not the case for charged kaons which have the quark content $u\overline{s}$ and $\overline{u}s$, respectively. Whereas the $\overline{u}$-quark of the K^- can annihilate with the valence u-quarks of the protons and neutrons, the u-quark of the K^+ can only strongly interact with sea quarks. Also the interaction $K^-(\overline{u}s) + n(udd) \rightarrow \Lambda(uds) + \pi^-$ is only possible for negatively charged kaons. Therefore, the K^- meson is expected to interact more likely with the detector than the K^+ meson.

The higher the energy of the particle colliding with the proton or neutron, the more likely it is, that sea quarks take part in the interaction. Therefore, it is expected that the difference between positively and negatively charged kaons is reduced with increasing momenta of the kaons.

Figure 2.7 shows the measured cross-section of positively and negatively charged pions and kaons with deuterium as function of the momenta of the mesons. Since

deuterium consists of the same amount of protons and neutrons, it is a good approximation of the detector material. As expected, there is no difference between the two pions, whereas a significant asymmetry between the two kaons is visible. This effect is of the order of 20% for kaons with a momentum of $10\,\mathrm{GeV}/c$ and leads to an asymmetric detection of charged kaons. Neutral kaons can be treated analogously and are discussed in more detail in chapter 9.

Chapter 3

The LHCb experiment

In this chapter, the LHCb experiment located at the LHC is briefly presented. Thereby, only the relevant aspect for this analysis are discussed in more detail.

3.1 The Large Hadron Collider

The LHC, located at the European Organization for Nuclear Research laboratory (CERN) in Geneva, Switzerland, is up to now, the world largest cyclic hadron collider [20]. Its main purpose is to collide protons with protons, but some of the operation time is also spend for proton-lead and lead-lead collisions. The accelerator ring has a circumference of 26.7 km and it contains two proton beams of the same energy but opposite circulation direction. In each beam, the protons are grouped as bunches and they are brought to collision at four different interaction points, belonging to the main experiments ALICE [21], ATLAS [22], CMS [23] and LHCb [24].

The LHC was designed to contain 2808 bunches of 1.1×10^{11} protons per beam, and the beams can collide with a centre-of-mass energy of up to 14 TeV. In 2011 and 2012, the LHC was operated with an energy of 3.5 and 4 TeV per beam, respectively. Whereas the number of bunches was chosen to be only 1374, each bunch contained up to 1.7×10^{11} protons. After a shutdown period used for upgrading to higher beam energies, in June 2015 the LHC re-started recording data at a centre-of-mass energy of 13 TeV. For this analysis, only the proton-proton collisions recorded in 2011 and 2012 are used. For the LHCb experiment, this results in an integrated luminosity of approximately $3\,\mathrm{fb}^{-1}$.

3.2 The LHCb detector

In contrast to the general purpose detectors like ATLAS and CMS, the LHC beauty (LHCb) experiment is dedicated for the investigation of heavy mesons and baryons containing a bottom or a charm quark. At the LHC energies, these heavy quarks are dominantly produced by the interaction of two gluons. Due to the large centre-of-mass energy of the colliding protons, it is possible and likely that the participating gluons carry different fractions of the proton momenta. Therefore, most of the

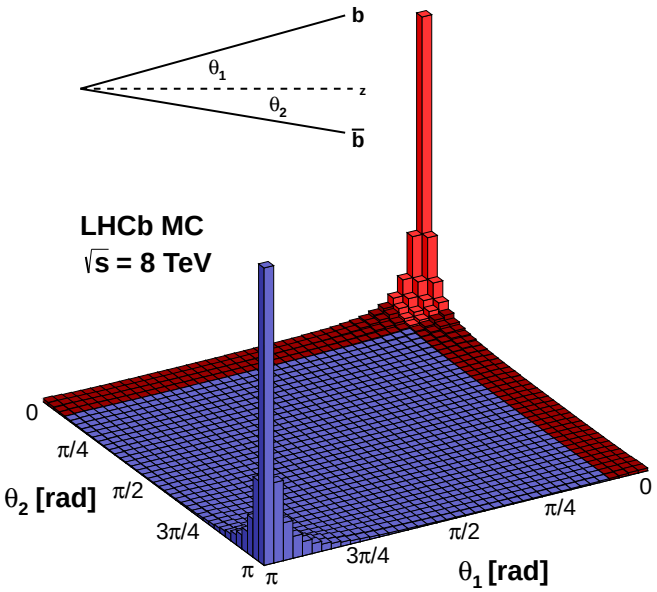

Figure 3.1: Simulated distribution of the polar angles of produced $b - \bar{b}$ pairs at a centre-of-mass energy of 8 TeV. The angles are defined with respect to the beam axis. Regions covered by the LHCb detector are shown in red. Figure taken from Ref. [25].

produced B- and D-hadrons show a strong boost in either of the beam directions. Figure 3.1 shows the simulated direction distribution of produced $b - \bar{b}$ pairs at a centre-of-mass energy of 8 TeV. In order to account for this distribution, the LHCb detector is build as a single-arm forward spectrometer. In figure 3.2, a vertical cross section through the detector is shown. All different sub-detectors are explained in the following sections.

The nominal LHC interaction point defines the origin of the LHCb coordinate system and the z-axis points along the beam axis into the direction of the detector. The y-axis of the LHCb coordinate system is chosen to be in vertical direction. Finally, the x-axis is chosen to form a perpendicular right handed xyz coordinate system with the other two axes. This coordinate system also defines the azimuthal angle ϕ in the x-y plain as: $\phi = 0 \equiv x$-direction and $\phi = \pi/2 \equiv y$-direction. The polar angle θ with respect to the z-axis is often transformed into the pseudorapidity $\eta = -\ln[\tan(\theta/2)]$. The geometry of the detector results in coverage of the polar angle between 10 mrad and 300 mrad in the xz-plane, and between 10 mrad and 250 mrad in the yz-plane, respectively. This corresponds to pseudorapidities between 2 and 5.

In the following, the different substructures of the detector are discussed. They

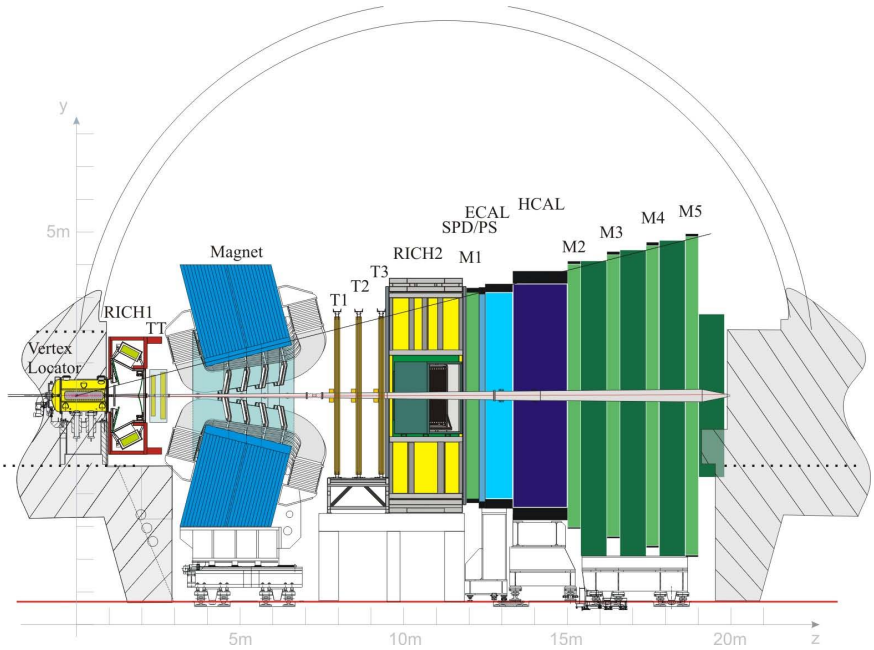

Figure 3.2: Schematic vertical cross section through the LHCb detector. The different sub-detectors are shown and explained in the text. Figure taken from Ref. [25].

can be grouped into the tracking system and the particle identification system. After that, the trigger structure and the particle reconstruction are briefly discussed.

3.2.1 The tracking system

In order to reconstruct and combine particles passing through the detector, their trajectories and momenta have to be measured. For charged particles, this is done by the tracking system. Going downstream the proton beam, it consists of the VErtex LOcator (VELO), the Tracking Turiencies (TT) before a dipole magnet, and the Inner and Outer Tracker (IT and OT) after the magnet. IT and OT form the Tracking (T) stations. The magnet is needed to determine the momenta of charged particles which are bent in its magnetic field.

Vertex Locator

The VErtex LOcator (VELO) surrounds the interaction region and is used to measure the tracks of charged particles with a high precision. With these tracks, the proton-proton vertex and possible secondary vertices can be measured. Since many heavy hadrons have a relatively long lifetime of the order of 1 ps and are strongly boosted, they fly a few millimetres. It is crucial to measure this separation from the primary interaction vertex in order to select the heavy hadron decays.

The VELO consists out of 21 stations each build out of two different silicon-strip

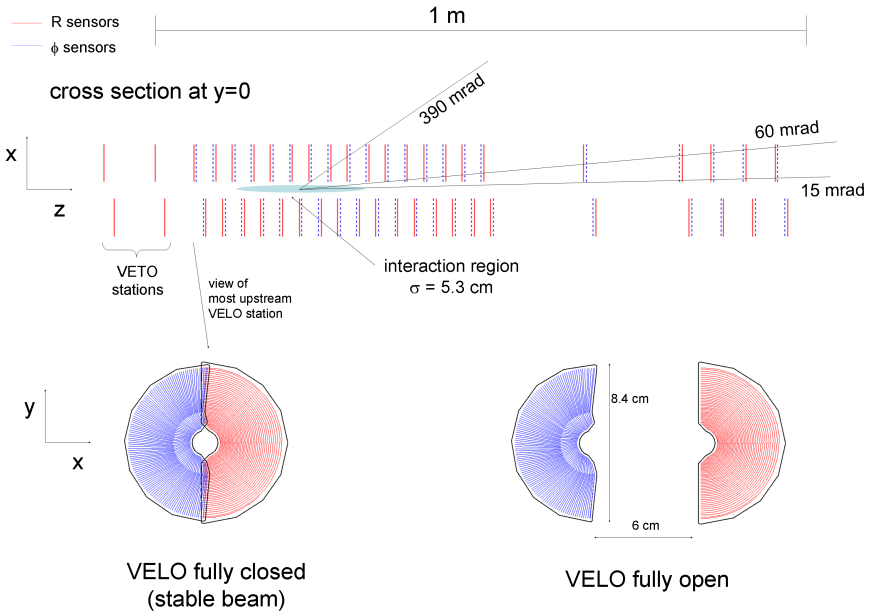

Figure 3.3: Schematic structure of the VELO (top) and a single station with radial and circular sensors. The overlap region between the two halves is shown bottom left. The pileup VETO stations are used for trigger decisions. Figure taken from Ref. [25].

sensors. One of these sensors has radial stripes and can, therefore, measure the azimuthal position whereas the other sensor has a circular structure and is used to determine the radial coordinate. Figure 3.3 shows how the stations are arranged around the beam pipe. They are grouped in two halves which can be moved away from the beam pipe when new proton beams are filled into the LHC and get adjusted. The two halves have an overlap region along the y-axis and a minimal distance to the beam of 8 mm. Inside the VELO, the beam vacuum is only maintained by the so-called RF foil made out of aluminium. Due to multiple scattering, it reduces the possible resolution of the reconstructed tracks. For an average primary vertex with 25 associated tracks, the vertex resolution is 13 μm in transversal direction and 71 μm along the beam axis.

Magnet

The magnetic field of the dipole magnet is aligned with the y-axis of the detector coordinate system. Therefore, charged particles are bent in the x-direction. Figure 3.4 depicts the magnet field as a function of the z-position. In total, an integrated magnet field of approximately 4 Tm bends the trajectories of the particles transversing the whole tracking system. Tracks can be categorized according to their extend in the tracking system. If a track has only hits in the VELO it is called a VELO

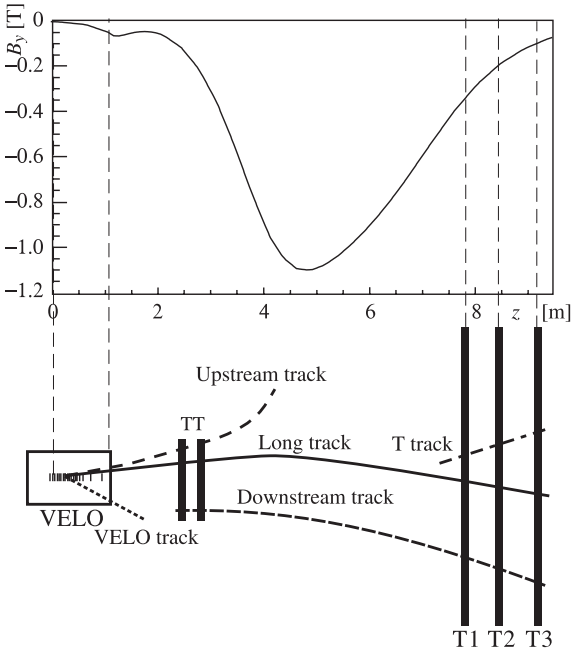

Figure 3.4: Main component of the magnetic field as a function of the z-position (top). Additionally, the different track categories and the tracking system are schematically shown (bottom). The different categories are explained in the text. Figure taken from Ref. [26].

track. If it also extends to the TT and is bend out of the detector afterwards it is called an Upstream track. Only if the OT or IT is involved in addition, the track is labelled as a Long track. Downstream tracks are not detected by the VELO and can origin for example from daughter particles of long living particles decaying outside the VELO. Finally, T tracks only have a signature in the T stations. For this analysis only Long tracks are used. The different track categories are shown in figure 3.4.

The polarity of the magnet can be reversed, which is regularly done during data taking. This helps to estimate and control effects originating from an asymmetric detector.

Silicon Tracker

Both, the TT and the IT are silicon micro-strip detectors. The pitch between the single strips is chosen to be $183\,\mu$m and $197\,\mu$m for the TT and IT, respectively, which results in a single hit resolution of approximately $50\,\mu$m. The TT is located directly before the magnet and covers the whole detector acceptance. It is build up out of four layers grouped as pairs. In the two outer layers, the stripes are oriented vertically, whereas the two inner ones are oppositely tilted by 5° with respect to the vertical ones. Thereby, the resolution in y-direction is improved. Figure 3.5a shows these four layers and their relative position and orientation. Due to its position

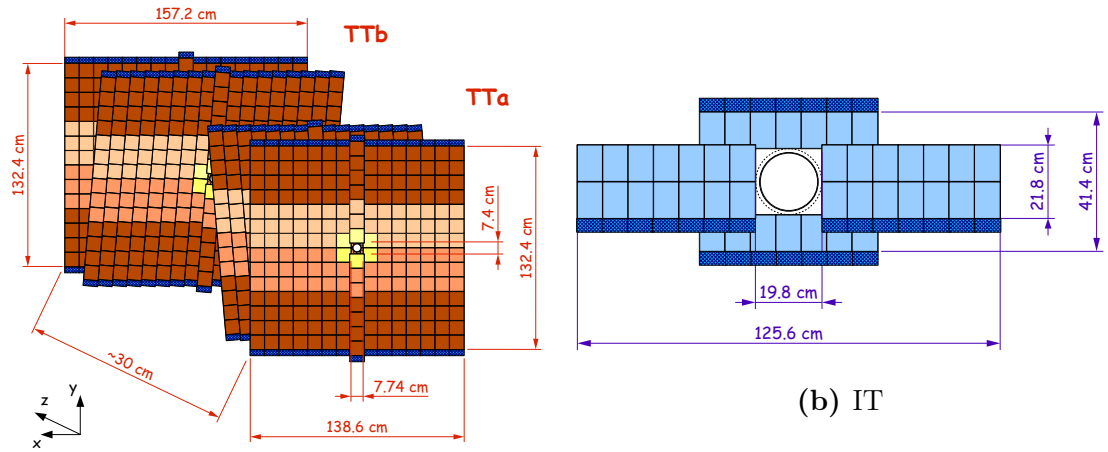

(a) TT

(b) IT

Figure 3.5: Schematic view of the two different silicon detectors. In (a) the TT and in (b) one layer of the inner tracker is shown. The dark blue regions represent the read out electronics and the individual modules are indicated by the black lines.Figures taken from Ref. [27] and [24].

in front of the magnet, the TT is used to reconstruct particles being bent out of the detector acceptance by the magnet. Additionally, it is used in the trigger and improves the track resolution of the VELO and the T stations.

The IT forms the inner part of the T stations as can be seen in figure 3.6a. There are three of these stations each one of which contains a cross-shaped inner part build up out of silicon strip sensors.

The IT covers the very high occupancy region close to the beam pipe. The high multiplicity of the particles in this central region is the reason for having a fine resolution silicon strip detector in the central part, and an Outer tracker with a coarser granularity in the region with a lower activity. For each station, the IT consists of four layers having the same relative orientation as the TT layers. As the T stations are located behind the magnet, they contribute dominantly to the momentum measurement. For the whole tracking system, a momentum resolution of 0.4% for small momenta, and 0.6% for 100 GeV/c is achieved.

Outer Tracker

In contrast to the IT the OT is realized as a gas detector with straw tubes. It makes up the outer part of the T stations. Each of the T stations contains four layers arranged in the orientation described above. These layers are build out of two rows of gas tubes with a diameter of 4.9 mm. This results in an single hit resolution of about 210 μm. In Figure 3.6b, a schematic view of such a double layer is shown. The tubes extend in vertical direction over one half of the OT respectively. In total,

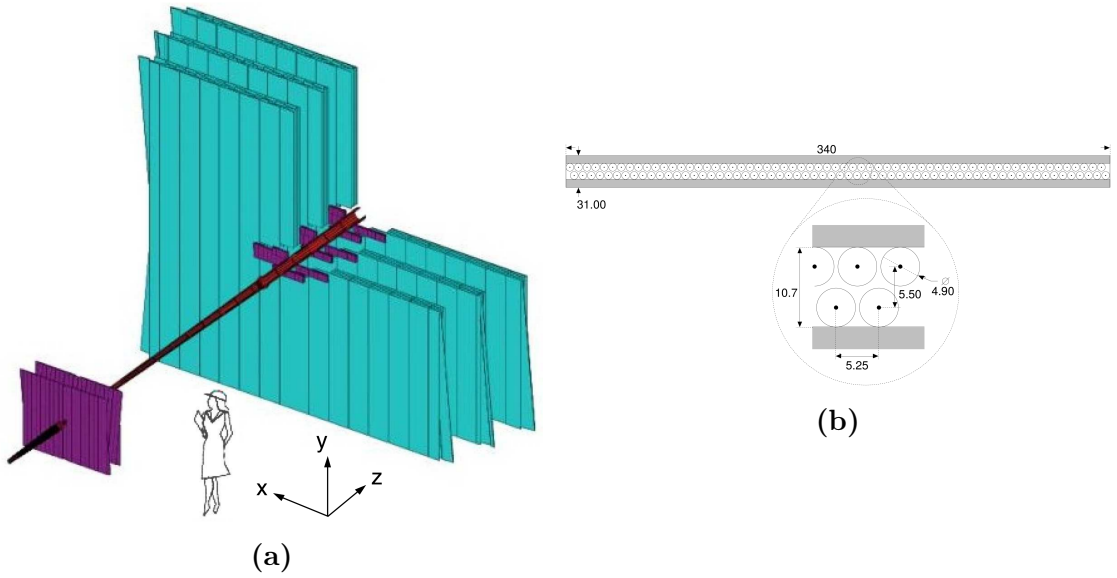

Figure 3.6: Schematic view of (a) the outer tracker as a part of the tracking system, and (b) of one single layer of the OT. The silicon trackers are shown in purple. The figure with the individuals OT tubes in (b) is shown as a horizontal cut. Figures taken from Ref. [24].

the T stations cover an area of $5 \times 6\text{m}^2$.

3.2.2 The particle identification system

Besides the measurement of the trajectory and the momentum, it is crucial to determine which type of particle passed through the detector. Only by this, a mass hypothesis and the combination of particles to heavier mother particles in the reconstruction is possible. The particle identification system of the LHCb detector consists out of two Ring-Imaging Cherenkov (RICH) detectors, a calorimeter system and the muon chambers.

Using the information from these subsystems, likelihood values $\mathcal{L}$ for the different particle hypothesis are calculated. From these values the DLL_{XY} variables defined as

$$\text{DLL}_{XY} = \ln\mathcal{L}_X - \ln\mathcal{L}_Y \tag{3.1}$$

are calculated for the particle hypothesis X vs particle hypothesis Y.

In the following, the different subsystems are described.

Ring-Imaging Cherenkov detectors

For this analysis, only final states with charged hadrons are present. These are identified by the two Ring-Imaging Cherenkov detectors RICH1 and RICH2. Charged

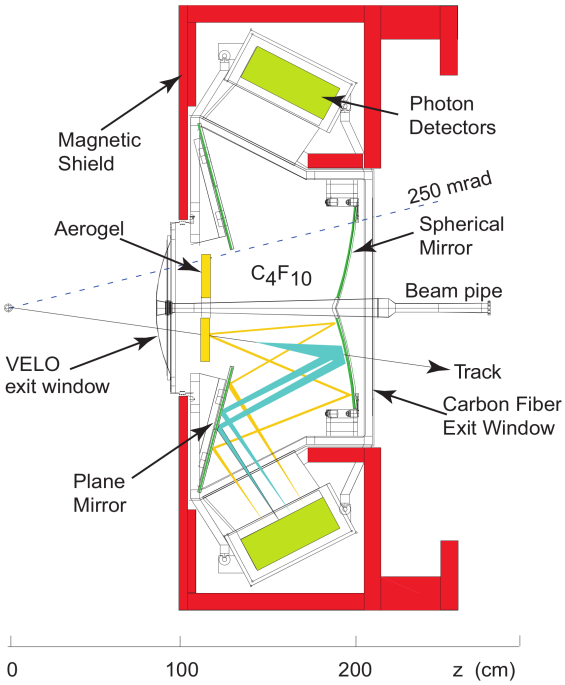

Figure 3.7: Layout of the RICH1 detector. The shown z-axis describes the distance from the nominal pp interaction point. Figure taken from Ref. [24].

particles travelling through a medium with a velocity larger than the speed of light in this medium emit photons under a specific angle θ given by:

$$\cos\theta = \frac{1}{\beta n}, \tag{3.2}$$

where β is the velocity in units of the speed of light, and n the refractive index of the medium. By measuring the opening angle of the emitted light cone, the velocity of the particle can be calculated. By combining it with the measured momentum, the mass can be calculated and a particle hypothesis is assigned. In the RICH detectors, the emitted light is guided by mirrors to hybrid photon detectors. This is shown in figure 3.7.

The RICH1 is located in front of the TT and is filled with aerogel and C_4F_{10} which have different refractive indices optimized for particles in the momentum range of $2\,\mathrm{GeV}/c$ to $40\,\mathrm{GeV}/c$. In order to distinguish high momentum pions, kaons, protons and muons, RICH2 is filled with CF_4 which has a smaller refractive index, and is, therefore, sensitive up to a momentum of $100\,\mathrm{GeV}/c$. Since high momentum particles are more likely to be produced along the beam pipe, RICH2 is located behind the T stations and does not cover, in contrast to RICH1, the whole detector acceptance.

Calorimeters

The calorimeter system of the LHCb detector is responsible for the energy measurement and identification of hadrons, photons and electrons. Additionally, its response is used in the trigger decision as discussed in chapter 3.2.3. There are four different calorimeters, all placed downstream the T stations. They have a similar structure and consist of alternating plates of absorbing and scintillating material. Particles passing through the absorbing plates deposit energy in the form of particle showers which are translated by the scintillating layers into photons. These photons are detected by photon multipliers.

The Scintillating Pad Detector (SPD) is the first component and is used to distinguish between photons and electrons since only the latter deposit some energy in it. Following the beam direction, the next components are the Pre-Shower detector (PS) and the Electromagnetic (ECAL) and Hadronic (HCAL) calorimeter. The former two are used to measure the energy of electrons and photons, whereas the latter is responsible for hadrons. Since electrons and photons hardly reach the HCAL, the combination of ECAL and HCAL can be used to distinguish between hadrons and electrons or photons.

For this analysis the main contribution of the calorimeter system is its input for the trigger decisions.

Muon system

Although muons are not relevant for the reconstructed decays used for this analysis, their identification should be shortly discussed. Muons which have a large enough momentum to not being bent out by the magnet are so called minimal ionizing particles and hardly interact with the previously discussed calorimeter system. Therefore, the muon stations M2-M5 are placed at the end of the detector. Additionally, there are 80 cm thick iron absorbers between them. They ensure that only muons reach the rear muon stations, which helps identifying muons. The first muon station M1 is placed for trigger purposes in front of the calorimeter system. All muon stations except the inner part of M1 are build out of multi-wire proportional chambers which measure the trajectory of muons. Due to the higher particle flux, the inner part of M1 is build as a gas electron multiplier.

3.2.3 The trigger system

The LHC is designed to collide proton bunches with a frequency of 40 MHz. Since it is not possible to record the detector response with the same frequency, only events which are likely to contain b- and c-quarks are selected and recorded. To decide whether an event is potentially of interest is the task of the trigger system.

The first stage is the hardware trigger $L0$ which reduces the rate to 1 MHz. It uses the information from the calorimeter system and the muon stations. In the calorimeter system, a large transversal energy deposition triggers the event. Thereby,

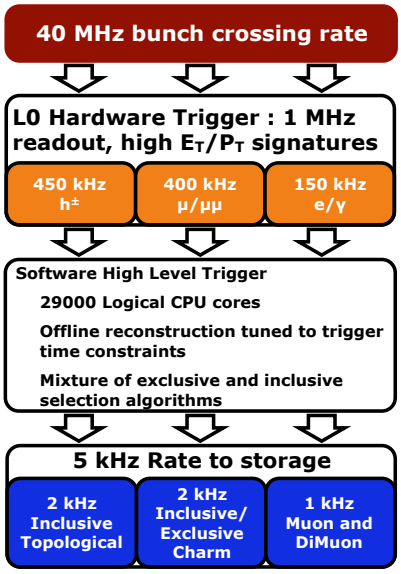

Figure 3.8: Scheme of the trigger system of LHCb. Only the configuration for 2012 is shown. Figure taken from Ref. [25].

the trigger distinguishes between hadrons, photons and electrons having caused this deposition. In the muon stations, the L0 trigger searches for straight lines and estimates the transversal momentum of these candidates. If it exceeds a certain value, the event is passed to the next trigger stage and the event is tagged as "triggered by a muon".

Events passing the hardware trigger are further filtered by two software stages. The HLT1 trigger adds information from the tracking system and creates first track candidates with the associated measured momenta. On top of requirements on the momenta, events with tracks having an high impact parameter with respect to the primary pp-vertex are triggered. Finally, in the HLT2 trigger, an almost complete reconstruction of the event is performed using all subsystems of the LHCb detector. Here, dedicated trigger lines for specific decays and typical decay topologies of heavy hadrons are implemented. The HLT2 trigger reduces the rate to the recordable 5 KHz.

Using the full reconstruction of an event and the information which trigger has selected the event, it is possible to categorise an event with respect to a specific particle or decay in this event as either:

- triggered by the decay/particle (TOS) or
- triggered independently of the decay/particle (TIS).

This can be done for every trigger stage and categorizing an event for example as `L0Hadron` TIS with respect to a specific charm meson decay means, that other

particles than the final state particles of the charm meson were sufficient to trigger the event. In chapter 6.3 the chosen trigger configurations for this analysis are discussed.

Chapter 4

Analysis overview

The aim of this analysis is to measure the time-integrated CP asymmetry of the decay $D^0 \to K^-K^+$:

$$A_{CP}(K^-K^+) = \frac{\Gamma(D^0 \to K^-K^+) - \Gamma(\overline{D}^0 \to K^-K^+)}{\Gamma(D^0 \to K^-K^+) + \Gamma(\overline{D}^0 \to K^-K^+)}. \tag{4.1}$$

Only D^0 candidates originating from the decay $D^{*+} \to D^0\pi^{+1,2}_{sl}$ are used. Thereby, the flavour of the D^0 meson at production can be determined by the charge of the pion. This specific choice of the origin of the D^0 meson introduces nuisance detection and production asymmetries coming from the D^{*+} and the π^+_{sl}, respectively. In order to determine or correct for these nuisance asymmetries, the calibration channels $D^{*+} \to D^0(\to K^-\pi^+)\pi^+_{sl}$, $D^+ \to K^-\pi^+\pi^+$, and $D^+ \to \overline{K}^0\pi^+$ are used.

This thesis is structured according to the different steps that have do be performed in order to determine $A_{CP}(K^-K^+)$:

- Chapter 5 presents possible nuisance asymmetries and how the different calibration channels have to be combined to yield a cancellation of these additional asymmetries.
- In order to measure the asymmetries of the used channels, it is necessary to select the specific decays and suppress any possible background coming from other particles that are produced in the proton-proton collision. Chapter 6 presents the strategy of this signal selection and a discussion of possible background sources.
- For the determination of $A_{CP}(K^-K^+)$, it is necessary to measure the raw asymmetry of the selected $D^0 \to K^-K^+$ decays as well as of the selected events of the calibration channels. These raw asymmetries are obtained with binned maximum likelihood fits to the mass difference between the D^{*+} and the D^0 meson candidates, Δm, and the mass of the D^+ meson candidate, respectively. For this purpose, the data samples are split according to the flavour of the charm meson, and simultaneous fits are performed to obtain the

[1] If not stated otherwise, the CP conjugated decays are always implied.

[2] Reminder: The pion is labelled as slow since the mass difference between the D^{*+} and D^0 meson is near the pion mass. Therefore, the pion is not additionally boosted after the decay.

asymmetry between these categories. This extraction of the raw asymmetries of each channel is presented in chapter 7.

- The nuisance asymmetries depend on kinematic variables of some of the involved particles. Therefore, it is important that the kinematic distributions of the selected events of the calibration channels are similar to the distributions of the selected $D^{*+} \to D^0(\to K^-K^+)\pi^+_{sl}$ candidates. This requires an weighting of the used channels which is presented in chapter 8.

- One of the nuisance asymmetries is the neutral kaon asymmetry. It arises from the calibration channel $D^+ \to \overline{K}^0\pi^+$ and is not cancelled like the other nuisance asymmetries. Chapter 9 presents a method how this asymmetry can be calculated.

- Taking into account the changes due to the weighting procedure, the different raw asymmetries are combined in chapter 10 in order to obtain a value for $A_{CP}(K^-K^+)$. Finally, systematic effects are studied in chapter 11.

The analysis presented in this thesis constitutes the second measurement of the quantity $A_{CP}(K^-K^+)$ with the LHCb experiment. A previous analysis used semileptonic B-hadron decays to tag the flavour of the neutral charm meson [5]. The methods and strategies developed in this former study are the basis of the one presented here. This includes the specific choice of the calibration channels which has to be modified only little, the basic idea of the weighting procedure and the calculation of the neutral kaon asymmetry. However, especially the exact procedure of the weighting and, associated therewith, the selection strategy has to be strongly adapted to the prompt charm samples.

Chapter 5

Asymmetries and analysis strategy

This chapter explains the basic strategy for determining $A_{CP}(D^0 \to K^-K^+)$. First, the arising additional[1] asymmetries are discussed. Then, the formalism of composite asymmetries is introduced and applied to the channel $D^{*+} \to D^0(\to K^-K^+)\pi^+_{sl}$ as an example. After that, the strategy for obtaining the final CP asymmetry by combining the different channels is presented. Finally, the different data sets and their combination are discussed.

5.1 Discussion of occurring additional asymmetries

In general, there are two types of asymmetries besides the actual CP asymmetry contributing to the measured raw asymmetries. The first one are detection asymmetries which originate from different detection efficiencies for particles and their antiparticles. The other type are production asymmetries which have their origin in the fact, that the LHC is a proton-proton collider, which is an asymmetric initial state containing more quarks than antiquarks.

5.1.1 Production asymmetries

For this analysis, the production asymmetry of charged charm mesons is of special interest. Although charm quarks are always produced as $c\bar{c}$ pairs, the hadronization with proton remnants introduces an enhancement of the number of $D^-(\bar{c}d)$ mesons with respect to the number of $D^+(c\bar{d})$ mesons. This means that the production asymmetry

$$A_P(D^+/D^{*+}) = \frac{\sigma(D^+/D^{*+}) - \sigma(D^-/D^{*-})}{\sigma(D^+/D^{*+}) + \sigma(D^-/D^{*-})} \tag{5.1}$$

is expected to be negative. Here σ is the cross-section for creating the respective charm meson in a pp collision. An easy explanation for this is given by the baryon number conservation in the SM. This conservation requires that there are exactly two more baryons than antibaryons in the final state since this is also the case for the initial proton-proton state. Thus, it is more likely that a c-quark forms a charm

[1] Additional meaning besides the asymmetry due to CP violation.

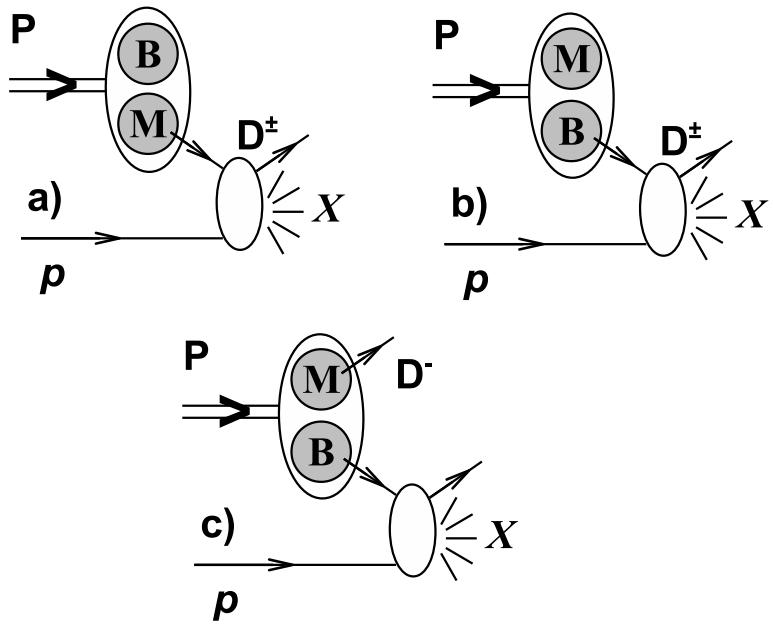

Figure 5.1: Indirect a), b) and direct c) production of charm mesons. The indirect processes are available for mesons and antimesons, whereas the direct production can only lead to mesons containing a $\bar{c}$-quark. Figure taken from Ref. [28].

baryon than that a $\bar{c}$ gets part of an anti charm baryon. Therefore, more charm mesons containing a $\bar{c}$ are produced.

A more precise prediction can be made with the Meson Cloud model (MCM) [28]. This model adds a virtual $c\bar{c}$ pair and describes the proton before the collision as a virtual charm meson-baryon pair. When this proton collides with another proton one can categorize the production of a charm meson in direct and indirect processes. They are depicted in figure 5.1. In the direct production the meson does not interact with the other proton strongly, whereas in the indirect production the meson and baryon form new states when colliding with the proton. Since a $c\bar{c}$ pair can only lead to a meson containing an $\bar{c}$-quark and a baryon with a c-quark, direct production is only possible for the D^-/D^{*-} meson. Whereas indirect production can lead to charm mesons and antimesons. Therefore, the direct production causes a negative production asymmetry.

In the scope of the MCM, the detection asymmetry depends on the Feynman momentum x_F which is a measure for the longitudinal momentum of the charm meson [28]. Figure 5.2 shows the calculated asymmetries for 7 TeV pp collisions as a function of x_F. The rise for higher Feynman momenta, which also corresponds to higher pseudorapidities, can be naively explained by the above mentioned source of asymmetry. Direct production happens more likely in forward direction. At very high longitudinal momenta, meaning high pseudorapidities, the beam drag effect [30] plays an important role and causes the asymmetry to decrease. The beam drag effect describes the fact that c-quarks get more attracted by proton remnants than

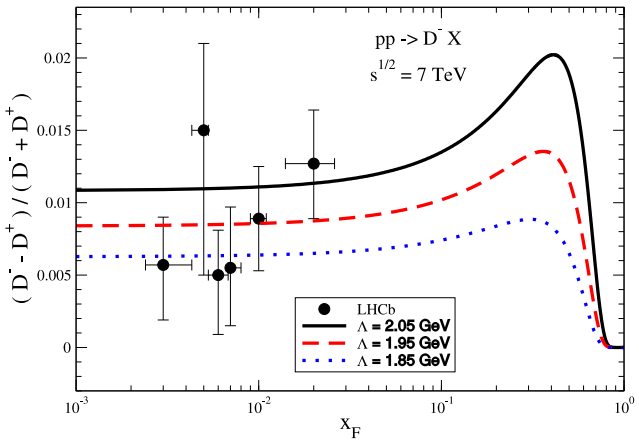

Figure 5.2: Predicted D^- production asymmetry dependence of the Feynman momentum x_F for different cut off parameters λ. Measurements of LHCb at 7 TeV [29] are given by the black data points. For the diagram the asymmetry was defined with an additional minus sign compared to equation 5.1. Figure taken from Ref. [28].

$\bar{c}$-quarks do. As shown in the diagram, charged charm mesons detected by the LHCb detector have a relatively low Feynman momentum and the influence of the drag effect is negligible.

The production asymmetry of charged charm mesons has been measured by LHCb for the 7 TeV data set to be $A_P(D^+) = (-0.96 \pm 0.26 \pm 0.18)\%$ [29]. The first uncertainty is statistical, the second systematic. This order of magnitude is also consistent with the theoretical predictions, see figure 5.2.

5.1.2 Detection asymmetries

For this analysis, detection asymmetries of kaons and pions are relevant. One has to distinguish between asymmetries induced by material interactions and asymmetries coming from an asymmetric detector.

For kaons, interaction with matter is strongly asymmetric as discussed in chapter 2.4. Since kaons that are absorbed by the detector material might not be detected, there is a difference in the detection efficiencies of positively and negatively charged kaons. The amount of material traversed by particles depends on their trajectories. Therefore, the asymmetry depends on the kinematic variables of the particles. The expected value is of the order of 1% [5] for charged kaons, and decreases with increasing momentum. Since the K^- interaction with matter is enhanced with respect to the the K^+ meson, cf. chapter 2.4, their detection efficiency is smaller. For the neutral kaon asymmetry, also other effects have to be taken into account which is discussed seperately in chapter 9. For pions, the detection asymmetry due to material interactions is expected to be negligible, cf. chapter 2.4.

Misalignment and dead regions in the tracking system can cause different reconstruction efficiencies for different parts of the detector. The magnet is responsible for the fact that particles of different charge are preferentially bent in different detector regions. These two effects can cause differences in reconstruction efficiencies for positively and negatively charged particles. Since slow particles are bent more strongly, this asymmetry is expected to increase with decreasing momentum. By inverting the magnet polarity this effect is reversed and by taking the mean, it should completely cancel. In [31] the detection asymmetry of charged pions was measured using partial reconstruction. It turned out to be consistent with zero when averaging over the magnet polarity. Furthermore, the individual asymmetries for each magnet polarity are measured to be less than 1%.

5.2 Extraction of $A_{CP}(D^0 \to K^-K^+)$

Beside the actual asymmetry between $D^0 \to K^-K^+$ and $\overline{D}^0 \to K^-K^+$ decays due to different decay rates, there are two more sources of asymmetries which can influence the finally measured raw asymmetry. These are the detection asymmetry of the slow pion[2] and the production asymmetry of the D^{*+} mesons. How these can be removed is explained in the following two subsections. The general formalism and the used calibration channels base on the previous analysis using semileptonic b-meson decays [5].

5.2.1 Interplay of multiple asymmetries

Using the channel $D^{*+} \to D^0(\to K^-K^+)\pi^+_{sl}$, the interplay of different sources of asymmetries is discussed.

The production asymmetry of the D^{*+} meson can be expressed as

$$A_P(D^{*+}) = \frac{p_P(D^{*+}) - p_P(D^{*-})}{p_P(D^{*+}) + p_P(D^{*-})}, \tag{5.2}$$

where $p_P(x)$ refers to the probability to produce the corresponding particle in a proton-proton (pp) collision. Analogously, the detection asymmetry of the slow pion is given by:

$$A_D(\pi^+_{sl}) = \frac{\epsilon(\pi^+_{sl}) - \epsilon(\pi^-_{sl})}{\epsilon(\pi^+_{sl}) + \epsilon(\pi^-_{sl})}, \tag{5.3}$$

with $\epsilon(x)$ being the detection efficiency of the positively or negatively charged slow pion. Finally, the CP asymmetry of the decay is defined using the partial decay

[2]Reminder: The pion originating from the decay of the D^{*+} meson is used to determine the flavour of the neutral charm meson. It is called the slow pion since it is not significantly boosted by the D^{*+} meson decay.

widths $\Gamma(D^0 \to K^-K^+)$ and $\Gamma(\overline{D}^0 \to K^-K^+)$:

$$A_{CP}(D^0 \to K^-K^+) = \frac{\Gamma(D^0 \to K^-K^+) - \Gamma(\overline{D}^0 \to K^-K^+)}{\Gamma(D^0 \to K^-K^+) + \Gamma(\overline{D}^0 \to K^-K^+)}. \tag{5.4}$$

Solving for the partial decay widths yields:

$$\Gamma(D^0 \to K^-K^+) = \frac{1 + A_{CP}}{2}(\Gamma(D^0 \to K^-K^+) + \Gamma(\overline{D}^0 \to K^-K^+)) \tag{5.5}$$

$$\Gamma(\overline{D}^0 \to K^-K^+) = \frac{1 - A_{CP}}{2}(\Gamma(D^0 \to K^-K^+) + \Gamma(\overline{D}^0 \to K^-K^+)). \tag{5.6}$$

The same conversion can be done for the production probability and the detection efficiency. This leads to

$$N^+ = N(D^0 \to K^-K^+) \propto (1 + A_P)(1 + A_D)(1 + A_{CP}) \tag{5.7}$$

$$N^- = N(\overline{D}^0 \to K^-K^+) \propto (1 - A_P)(1 - A_D)(1 - A_{CP}), \tag{5.8}$$

where $N^{+/-}$ is the number of reconstructed and selected $D^0/\overline{D}^0$ decays, respectively. Constant factors that are common for N^+ and N^- are not of interest and were ignored in these equations. The final raw asymmetry

$$A_{raw} = \frac{N^+ - N^-}{N^+ + N^-} \tag{5.9}$$

can then be rearranged to

$$A_{raw} = \frac{A_P + A_D + A_{CP} + A_P A_D A_{CP}}{1 + A_P A_D + A_P A_{CP} + A_D A_{CP}}. \tag{5.10}$$

Since all occurring asymmetries are expected to be at most at the few percent level, this equation can be linearised to:

$$A_{raw} = A_P + A_D + A_{CP}. \tag{5.11}$$

Corrections to this approximation are third order terms and higher. Therefore, they are expected to be of the order $\mathcal{O}(10^{-6})$ and negligible. But this assumption does not have to be valid if there are fiducial regions where single asymmetries are large. This is shortly discussed here.

As mentioned in the previous subsection, the individual asymmetries depend on kinematic variables. This fact needs to be included for a more precise description of the measured raw asymmetry:

$$\begin{aligned} A_{raw} &= \int A_{raw}(\boldsymbol{p}_{D^*}, \boldsymbol{p}_{\pi_{sl}}) n(\boldsymbol{p}_{D^*} \boldsymbol{p}_{\pi_{sl}}) \mathrm{d}\boldsymbol{p}_{D^*} \mathrm{d}\boldsymbol{p}_{\pi_{sl}} \\ &= \int \frac{A_P(\boldsymbol{p}_{D^*}) + A_D(\boldsymbol{p}_{\pi_{sl}}) + A_{CP} + A_P(\boldsymbol{p}_{D^*}) A_D(\boldsymbol{p}_{\pi_{sl}}) A_{CP}}{1 + A_P(\boldsymbol{p}_{D^*}) A_D(\boldsymbol{p}_{\pi_{sl}}) + A_P(\boldsymbol{p}_{D^*}) A_{CP} + A_D(\boldsymbol{p}_{\pi_{sl}}) A_{CP}} n(\boldsymbol{p}_{D^*}, \boldsymbol{p}_{\pi_{sl}}) \mathrm{d}\boldsymbol{p}_{D^*} \mathrm{d}\boldsymbol{p}_{\pi_{sl}}. \end{aligned} \tag{5.12}$$

Here $\boldsymbol{p}$ represents the kinematic variables on which the respective asymmetry depends:

$$\boldsymbol{p}_{D^*} \equiv p_T^{D^*}, \eta^{D^*} \tag{5.13}$$
$$\boldsymbol{p}_{\pi_{sl}} \equiv p_T^{\pi_{sl}}, \eta^{\pi_{sl}}, \phi^{\pi_{sl}}, \tag{5.14}$$

and $n(\boldsymbol{p}_{D^*}, \boldsymbol{p}_{\pi_{sl}})$ is the normalised data distribution as function of these variables. Since the production asymmetry of D^{*+} mesons does not depend on ϕ, cf chapter 5.1.1, this variable can be omitted. To make the same approximation as in 5.11, the asymmetries have to be small for all $\boldsymbol{p}_{D^*}$ and $\boldsymbol{p}_{D^*}$. Therefore, one has to exclude regions where this is not the case. For production asymmetries, no regions with extremely high asymmetries are expected, but, as discussed in chapter 6, dead detector regions and the bending of charged particles by the magnet cause high detection asymmetries. The fiducial cuts described in chapter 6 remove such regions with high detection asymmetries, and additional regions are excluded as a systematic study in chapter 11.3.

5.2.2 Cancellation of additional asymmetries

According to equation 5.11, the CP asymmetry can be expressed as the difference of the measured raw asymmetry, and the production and detection asymmetry of the D^{*+}/π_{sl}^+:

$$A_{CP}(D^0 \to K^-K^+) = A_{raw}(D^0 \to K^-K^+) - A_P(D^{*+}) - A_D(\pi_{sl}^+). \tag{5.15}$$

The decay $D^{*+} \to D^0(\to K^-\pi^+)\pi_{sl}^+$ is used as a calibration channel to cancel the additional production and detection asymmetry. Since this decay is Cabibbo-favoured, the CP asymmetry can be neglected[3]. In contrast to the decay into two kaons, the final state $K^-\pi^+$ is not CP symmetric. Therefore, additional detections asymmetries, as discussed in the last subsection, are present:

$$A_{raw}(D^0 \to K^-\pi^+) = A_P(D^{*+}) + A_D(\pi_{sl}^+) + A_D(K^-) + A_D(\pi^+) \tag{5.16}$$
$$\Leftrightarrow \quad A_P(D^{*+}) + A_D(\pi_{sl}^+) = A_{raw}(D^0 \to K^-\pi^+) - A_D(K^-) - A_D(\pi^+). \tag{5.17}$$

In order to evaluate the detection asymmetry of the K^- and the π^+, the Cabibbo-favoured decay $D^+ \to K^-\pi^+\pi^+$ is used. Using the previously discussed asymmetries, cf. chapter 5.1, its raw asymmetry is given by

$$A_{raw}(D^+ \to K^-\pi^+\pi^+) = A_P(D^+) + A_D(K^-) + A_D(\pi_{l.m.}^+) + A_D(\pi_{h.m.}^+) \tag{5.18}$$
$$\Leftrightarrow \quad A_D(K^-) + A_D(\pi_{l.m.}^+) = A_{raw}(D^+ \to K^-\pi^+\pi^+) - A_P(D^+) - A_D(\pi_{h.m.}^+), \tag{5.19}$$

where the pion with the **h**igher transverse **m**omentum is labelled as $\pi_{h.m.}^+$, and the one with the **l**ower transverse **m**omentum as $\pi_{l.m.}^+$. In principle both pions could be

[3] In contrast to the Cabibbo-suppressed decays, the tree-level contributions dominate the decay amplitudes of Cabibbo-favoured decays.

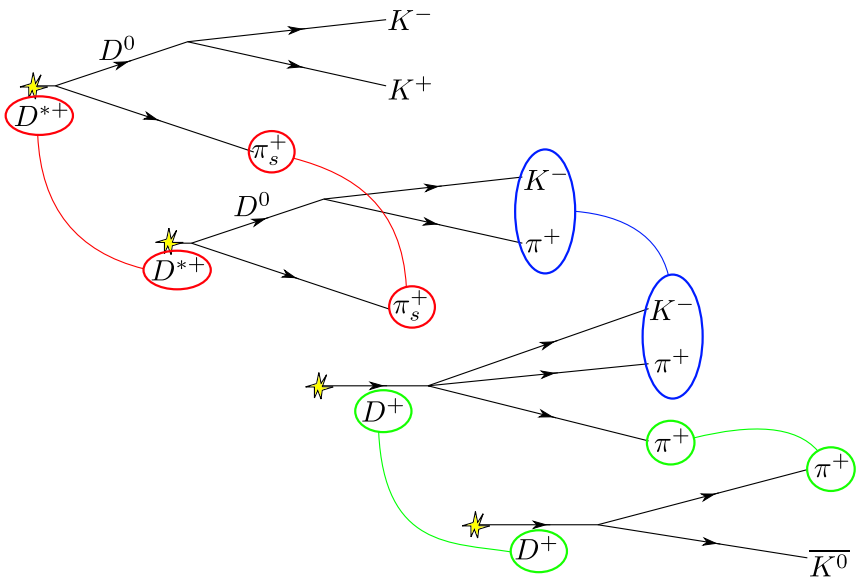

Figure 5.3: Strategy to cancel additional asymmetries of the raw asymmetry of the decay $D^0 \to K^-K^+$. Connected particles indicate the cancellation of their production or detection asymmetries by the subtraction of raw asymmetries.

chosen to cancel with the pion of the decays $D^0 \to K^-\pi^+$ but as will be discussed in chapter 6.4.3 and 8.2.1, it is more reasonable to choose the low momentum pion. The remaining production asymmetry of the D^+ meson and the detection asymmetry of the other pion are cancelled by using the decay $D^+ \to \overline{K}^0\pi^+$. It is also Cabibbo favoured and the measured raw asymmetry, therefore, only depends on detection and production asymmetries:

$$A_{raw}(D^+ \to \overline{K}^0\pi^+) = A_P(D^+) + A_D(\overline{K}^0) + A_D(\pi^+) \tag{5.20}$$

$$\Leftrightarrow \quad A_P(D^+) + A_D(\pi^+) = A_{raw}(D^+ \to \overline{K}^0\pi^+) - A_D(\overline{K}^0). \tag{5.21}$$

Only the neutral kaon asymmetry remains. Due to the lifetime acceptance, only kaons with a small decay time are selected, and the asymmetry is expected to be small and can be calculated, cf. chapter 9. The combination of equations 5.15 to 5.21 yields an expression for $A_{CP}(D^0 \to K^-K^+)$ which only depends on the measured raw asymmetries and the calculable $\overline{K}^0$ asymmetry:

$$\begin{aligned} A_{CP}(D^0 \to K^-K^+) =& A_{raw}(D^0 \to K^-K^+) - A_{raw}(D^0 \to K^-\pi^+) \\ &+ A_{raw}(D^+ \to K^-\pi^+\pi^+) - A_{raw}(D^+ \to \overline{K}^0\pi^+) \\ &+ A_D(\overline{K}^0). \end{aligned} \tag{5.22}$$

This is only valid if the single asymmetries can be linearly added as it is discussed in chapter 5.2.1. From this equation it is immediately clear that the statistical

uncertainty of each used channel directly translates into the statistical uncertainty of the final CP asymmetry. Figure 5.3 shows all used channels and how their individual asymmetries are meant to cancel.

As indicated in equation 5.12, the individual asymmetries depend on the kinematic variables of the involved particles. Therefore, detection and production asymmetries cancel between different channels only if both show the same distribution in the respective variables. Thus, the different channels need to be weighted to each other. This weighting procedure is discussed in detail in chapter 8.

5.3 Data categories

The analysis is independently performed for each of the four categories of data samples separated by magnet polarity up, magnet polarity down and by data from 2011 and from 2012, taken at 7 TeV and 8 TeV, respectively. Especially the individual detection asymmetries are expected to be different for the different magnet polarities. They depend on geometrical asymmetries of the detector and inverting the magnet polarity is assumed to mirror these effects. However, after the cancellation of the additional asymmetries by using the different calibration channels, the final CP asymmetry should be independent of the polarity. The same holds for the 2011/2012 data categories. So, the four categories can be used as a consistency check.
Anyhow, in order to ensure the cancellation of detection asymmetries which flip sign with magnet polarity, the arithmetic mean of polarity up and polarity down is used:

$$A_{CP}^{up+down} = \frac{A_{CP}^{up} + A_{CP}^{down}}{2}. \tag{5.23}$$

In 2011 60% of the data were taken with magnet polarity down and, therefore, an arithmetic mean reduces the statistical sensitivity:

$$\sigma_{A_{CP}}^{up+down} = \frac{\sqrt{{\sigma_{A_{CP}}^{up}}^2 + {\sigma_{A_{CP}}^{down}}^2}}{2}. \tag{5.24}$$

Since in 2012 the size of the polarity samples is to good approximation equal, the overall loss of statistics is small.

When averaging the result from 2011 and 2012, the respective statistic uncertainties are used for a weighted mean:

$$A_{CP} = \frac{1}{\frac{1}{{\sigma_{A_{CP}}^{2011}}^2} + \frac{1}{{\sigma_{A_{CP}}^{2012}}^2}} \left(\frac{1}{{\sigma_{A_{CP}}^{2011}}^2} A_{CP}^{2011} + \frac{1}{{\sigma_{A_{CP}}^{2012}}^2} A_{CP}^{2012} \right), \tag{5.25}$$

$$\sigma_{A_{CP}} = \frac{1}{\sqrt{\frac{1}{{\sigma_{A_{CP}}^{2011}}^2} + \frac{1}{{\sigma_{A_{CP}}^{2012}}^2}}}. \tag{5.26}$$

This ensures the optimal statistical sensitivity.

The individual statistical uncertainty $\sigma_{A_{CP}}^{cat}$ of each of the four data categories originates directly from the statistical uncertainty of the measured raw asymmetries.

Chapter 6

Event selection

This chapter provides a description of the event reconstruction and selection. First, the decay topologies of the individual decays and some important properties which help to select the events are introduced. Then, the chosen trigger configuration is discussed. After that, the offline selection requirements applied to the stored data are explained.

6.1 Decay topologies

For the reconstruction and selection, the specific structure and characteristic properties of the decays are exploited. Therefore, the decay topologies will be shortly introduced for all channels which are relevant for this analysis.

6.1.1 D^{*+} decays

Both used $D^{*+} \to D^0(\to h^-h^+)\pi^+_{sl}$ decays[1] have the same decay topology and will therefore also have a very similar reconstruction and selection. Figure 6.1 shows the decay structure. For this analysis only prompt D^{*+} mesons are used. This means that they are directly produced in the pp collision and originate from the so-called primary vertex (PV). They decay almost immediately into a slow pion and a D^0 meson which therefore effectively also come from the PV.

Since the D^0 particle has a relatively large lifetime, it decays at a displaced decay vertex, called a secondary vertex (SV), which is a central property of heavy meson decays. An important quantity related to an secondary vertex is the impact parameter (IP) of particles which come from this SV. The impact parameter of a particle with respect to the PV is given by the smallest distance between the vertex and the extrapolated trajectory of the particle, see figure 6.1. Particles coming from a SV tend to have a high impact parameter. The distance between the PV and the SV is the flight distance $\gamma \cdot c\tau$ of the D^0 meson. Here, γ is the Lorentz factor of the boosted meson and τ is the proper decay time. The quantity $c\tau$ is, therefore, independent of the specific boost of the meson and can be used as a measure of the lifetime.

[1] In the following, these channels are sometimes abbreviated as only $D^0 \to h^-h^+$.

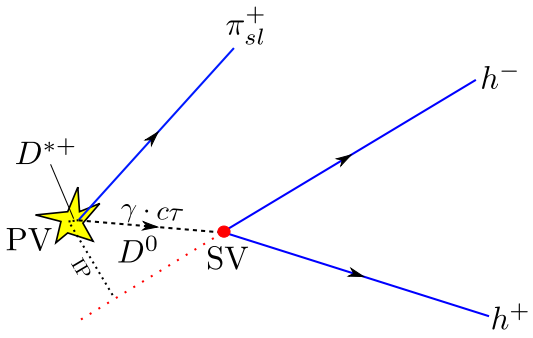

Figure 6.1: Decay topology of the decay $D^{*+} \to D^0(\to h^- h^+)\pi^+_{sl}$. The D^0 meson and the slow pion come from a D^{*+} meson which decays near the primary vertex (PV). The D^0 meson decays then at a secondary vertex (SV). Furthermore, the impact parameter (IP) of a final state hadron and the flight distance ($c\tau$) of the charm meson are sketched.

6.1.2 D^+ decays

The decay topologies of the decays $D^+ \to K^-\pi^+\pi^+$ and $D^+ \to \overline{K}^0\pi^+$ are shown in figure 6.2. Like the both D^0 decays, they have a displaced vertex due to the relatively long living charm meson. As previously discussed, this leads to high impact parameters of the D^+ meson daughters.

The K^0 state is a superposition of the long living K^0_L state and the K^0_s state which has a much shorter lifetime. Since almost all K^0_L mesons decay outside the VELO, only K^0_s mesons are used. They nearly always decay into two neutral or charged pions. Since neutral pions can not be detected by the tracking system, only the final state $\pi^-\pi^+$ is chosen. This state is symmetric and does not induce an additional

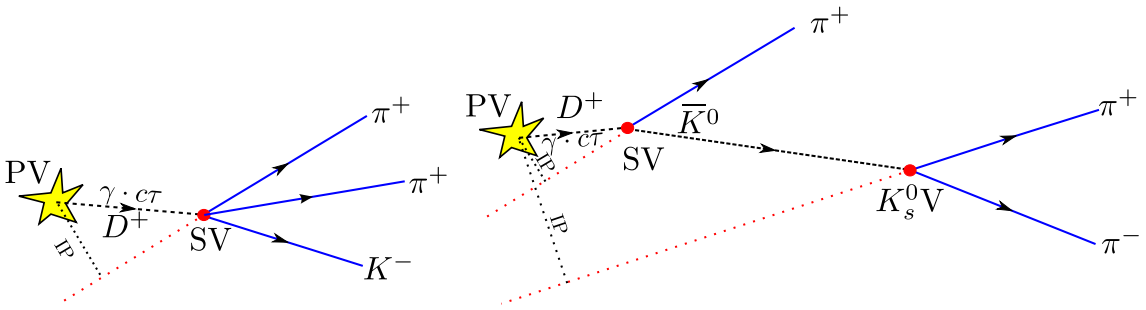

(a) $D^+ \to K^-\pi^+\pi^+$ **(b)** $D^+ \to \overline{K}^0\pi^+$

Figure 6.2: Decay topologies of the D^+ decays $D^+ \to \overline{K}^0\pi^+$ and $D^+ \to K^-\pi^+\pi^+$. The prompt D^+ mesons emerge at the primary vertex (PV) and decay at a secondary vertex (SV). Due to its long lifetime, the $\overline{K}^0$ meson decays at a strongly displaced third vertex (K^0_sV). In addition, the impact parameter (IP) of two final state hadrons and the flight distance ($c\tau$) of the charm meson are sketched.

detection asymmetry. Although the K_s^0 meson decays orders of magnitude faster than the K_L^0 meson, only approximately a quarter of them decay inside the VELO. Only such decays which lead to a long reconstructed track, cf. chapter 3, are used in this analysis. The K_s^0 meson decays at a third vertex ($K_s^0 V$) which is largely displaced from the PV.

6.2 Background sources

In order to extract the raw asymmetries, it is necessary to understand possible background sources. For the D^{*+} decays the raw asymmetries are extracted by a fit to the distribution of the measured mass difference Δm between the reconstructed D^{*+} and D^0 mesons, see chapter 7. In contrast to that, the raw asymmetries of the D^+ channels are obtained by a direct fit to the mass distribution of the charm meson.

6.2.1 Combinatorial background

When combining the final states particles to an D^0 or D^+ candidate, it is possible to combine random particles which do not originate from a common mother particle. This background is called combinatoric and is nearly always present. It is flat[2] and can be separated from the signal by the fit.

6.2.2 Random pion background

A special kind of combinatoric background present in the Δm distribution is the random pion background. It originates from a random pion being combined with a D^0 particle in order to reconstruct a D^{*+} meson. Since the nominal pion mass is assigned to all pion candidates, Δm values smaller than this mass are kinematically not possible. Therefore a strong threshold effect for small Δm is expected for this type of background. However it is also flat and can be separated from the signal by the fit.

6.2.3 Specific backgrounds

Besides these combinatorial backgrounds, specific decay channels that are not fully and/or wrongly reconstructed can leak into the signal regions. For the Cabibbo-favoured decays used in this analysis these background contributions are strongly suppressed and are not taken into account. An example for a possible background in the channel $D^0 \to K^-\pi^+$ is the decay $D^0 \to \pi^+\pi^-\pi^0$ where the neutral pion is not reconstructed while the negatively charged pion is mis-identified as a kaon. The higher mass of the kaon hypothesis partially compensates the missing pion, and if the D^0 meson originates from a D^{*+} meson this background might peak in the

[2]Flat means that there are no peaking structures.

Δm distribution. However, this background is found to be negligible in a similar analysis, which also came to the same result for other possible background decays [32].

Only for the Cabibbo-suppressed decay $D^0 \to K^-K^+$ it is expected that other decays might leak into the signal peak in the Δm distribution. Whereas mis-identified $D^0 \to K^-\pi^+$ decays peak far enough from the signal decay, partially reconstructed decays in which a pion is mis-identified as a kaon are more likely to be present in the signal region. Backgrounds from particles other than a D^0 meson originating from a D^{*+} meson, can not affect the signal peak in the Δm distribution and are, therefore, taken into account by the random pion background. In Ref. [32], detailed studies on possible channels were made. It turned out that the decay $D^0 \to K^-\pi^+\pi^0$ is most likely to influence the signal peak. Its influence is nevertheless expected to be small and will be studied by using a dedicated fit model as a systematic uncertainty in chapter 11.

6.3 Trigger selections

In chapter 3.2.3, the trigger system of the LHCb experiment was presented. This section describes the specific trigger configuration which is used to trigger events containing the decays of interest.

6.3.1 Hardware trigger

One possibility for triggering prompt charm decays by the L0 hardware trigger is via one of the pions or kaons in the final state which produces a high transverse energy deposition in the calorimeters. This means, that these events are then triggered by the signal candidate (TOS, cf. chapter 3.2.3). Since the final states are different for all used channels, a trigger on signal particles could introduce different asymmetries for the individual channels. This would lead to spurious asymmetries in the final CP asymmetry. Therefore, it is required that the event was triggered by the L0 trigger independently of the signal decay (TIS). This can for example happen by hadronic decay products of the other charm quark or a muon with high transverse momentum.

6.3.2 Software trigger

In the second stage of the software trigger, **Hlt2**, an almost full event reconstruction is performed. Therefore, it is possible to choose a trigger line which is dedicated to select events containing candidates of the respective D^0 and D^+ decays. In the case of the $D^{*+} \to D^0(\to h^-h^+)\pi^+_{sl}$ decays, two hadron candidates with high impact parameter are combined to from a D^0 meson candidate. There are several requirements which have to be fulfilled by this D^0 candidate and its daughter particles.

Table 6.1: Some important requirements of the chosen Hlt1 trigger line. If there are differences between the data taking periods 2011/first half 2012/second half 2012 the values are given in this order.

Variable	**Requirement**
IP	> 0.1mm
χ^2(IP)	> 16
p	$> 10/10/3\,\mathrm{GeV}/c$
p_T	$> 1.7/1.7/1.6\,\mathrm{GeV}/c$
χ^2_{track}/ndf	$< 2/1.5/2$

Since these criteria follow a similar strategy as the offline reconstruction which is presented in chapter 6.4, no details are given.

The decay $D^+ \to K^-\pi^+\pi^+$ is reconstructed in the Hlt2 software trigger stage following a similar strategy to the D^0 meson trigger lines' one. For the decay $D^+ \to \overline{K}^0\pi^+$, two pion candidates with large impact parameters are combined to form a K^0_s candidate. This candidate is then used to from a D^+ meson together with another pion which is also required to show a large impact parameter. Like for the D^0 meson decays, detailed requirements are only given for the offline selection.

The only requirement applied in the Hlt2 software trigger stage which should be mentioned at this point concerns the decision of the first software trigger stage, **Hlt1**. The chosen Hlt2 trigger lines as well for the D^0 as for the D^+ meson decays, require that one of the D^0 daughters had triggered the event in the Hlt1. Since this requirement has a large impact on the weighting procedure presented in chapter 8, the detailed criteria that have been applied in the Hlt1 software stage are given in table 6.1. For a more detailed discussion of the impact of the Hlt1 trigger decision see section 6.4.3.

The required trigger line in the Hlt1 software stage is designed to detect tracks with a high impact parameter with respect to the primary vertex. Beside the mentioned high impact parameter and its significance (χ^2(IP))[3], selection requirements on the momenta and track quality (χ^2_{track}/ndf) have to be fulfilled. The requirements changed between the data taking periods 2011, the first half of 2012, and the second half of 2012. The corresponding values are individually listed in the table. Again, a more detailed discussion and reasoning of the different selection criteria follows when describing the offline selection.

6.4 Offline selection

After the events have been triggered and stored, the individual decays are again reconstructed and selected in the so-called stripping. Stripping is a centralized

[3]The significance of the impact parameter is the gain of the χ^2 value of the PV vertex-fit when including the respective track to the PV.

Table 6.2: Used stripping lines for each of the used decays. They are all part of the `CHARM` micro-DST of `Reco14-Stripping20/r1`.

Decay	**Stripping line**
$D^{*+} \to D^0(\to K^-K^+)\pi^+_{sl}$	`DstarForPromptCharm`
$D^{*+} \to D^0(\to K^-\pi^+)\pi^+_{sl}$	`DstarForPromptCharm`
$D^+ \to K^-\pi^+\pi^+$	`D2hhh_KPPLine`
$D^+ \to \overline{K}^0\pi^+$	`D2KS0HPionLine`

reconstruction and selection of different event or channel types that is run on the entire LHCb dataset, and delivers pre-selected data for later analysis. Additional selection criteria on top of the stripping selection are applied afterwards and a certain Hlt1 trigger configuration is chosen.

6.4.1 Stripping requirements

For this analysis, the data collected in 2011 is recorded using a reconstruction version Reco14, and Stripping version `20r1`. The data collected in 2012 is reconstructed in the same way and selected by the Stripping version `20`. The specific selection lines in the stripping are listed in table 6.2. Their structure and requirements will be discussed for the different channels hereafter.

D^{*+} decays

As in the Hlt2 trigger line, the two final state hadrons are combined into a D^0 candidate. Then, another pion is combined with this candidate to form a D^{*+} candidate. All requirements for the different particles are listed in table 6.3. Except for the different particle identification (PID) requirements, cf. chapter 3.2.2, on the final state hadrons, they are exactly the same for $D^0 \to K^-K^+$ and $D^0 \to K^-\pi^+$ decays. These relatively loose PID requirements suppress background originating from misidentified particles. Beside certain selection criteria on kinematic variables like transverse momentum (p_T) or pseudorapidity[4] (η) and the track quality (track χ^2), the D^0 daughters are additionally required to have a high impact parameter significance (χ^2_{IP}) since they should originate from a secondary vertex. This reduced much of the hadronic background originating from the PV. The requirements on kinematic variables represent the detector acceptance (η) and suppress also hadrons originating from the PV which are strongly boosted (p_T). Light mesons originating from the decay of heavy particles tend to have higher transverse momenta. To reject unphysical tracks a selection requirement on the track ghost probability, $P_{ghost}(track)$, is applied. This quantity is a multivariate classifier used to reject tracks which do not originate from a real particle [33].

[4] Cf. chapter 3.2.

Table 6.3: Stripping requirements for the used D^{*+} decays. They are discussed in chapter 6.4.1.

Candidate	**Variable**	**Requirement**
K/π	track χ^2/NDF	< 5
	p_T	$> 250\,\mathrm{MeV}/c$
	$P_{ghost}(track)$	< 0.5
	χ^2_{IP}	> 9
	η	$\in (2, 5)$
K	$\mathrm{DLL}_{K\pi}$	> 2
π	$\mathrm{DLL}_{K\pi}$	< -2
D^0	p_T	$> 2000\,\mathrm{MeV}/c$
	$m(D^0) - m_{nominal}$	$\in (-50, 75)\,\mathrm{MeV}/c^2$
	$c \cdot \tau$	$> 100\ \mu\mathrm{m}$
	$\cos\alpha$	< 0.9
	vertex χ^2	< 9
	χ^2_{IP}	< 9
π^+_{sl}	track χ^2/NDF	< 5
	p_T	$> 250\,\mathrm{MeV}/c$
D^{*+}	vertex χ^2	< 64
	$m(D^{*+}) - m(D0)$	$< 155\,\mathrm{MeV}/c^2$

The reconstructed D^0 meson is required to have a good vertex fit quality (vertex χ^2), high p_T and a mass which is in a certain window around the true mass. The vertex fit quality describes how good the two tracks of the daughter candidates form a vertex. A requirement on the flight distance, $c\tau$, rejects events which have no secondary vertex. To reject non-prompt charm, the impact parameter significance of the D^0 meson with respect to the PV, χ^2_{IP}, is required to be small. The quantity $\cos\alpha$ is the cosine of the angle between the D^0 daughters' momenta and the D^0 momentum in its rest frame and is required to be smaller than 0.9. This supports the requirement of a high impact parameter significance for the D^0 daughters. The additional slow pion only has to fulfil requirements on p_T and the track quality, track χ^2/NDF. When combining it with the D^0 meson, the mass difference of the resulting D^{*+} candidate and the D^0 meson is not allowed to exceed a certain value. Additionally a requirement on the vertex quality of the D^{*+} candidate, vertex χ^2, candidate is imposed.

D^+ decays

For the decay $D^+ \to K^-\pi^+\pi^+$, similar requirements are used as for the D^0 decays. Only the additional variables will be discussed. All selection requirements can be found in table 6.4. In order to form a good D^+ decay vertex, its children are required to have a distance of closest approach (DOCA) smaller than 0.5mm. Since

Table 6.4: Stripping requirements for $D^+ \to K^-\pi^+\pi^+$ candidates. They are discussed in chapter 6.4.1.

Candidate	**Variable**	**Requirement**
K/π	track χ^2/NDF	< 4
	p_T	$> 250\,\mathrm{MeV}/c$
	p	$> 2000\,\mathrm{MeV}/c$
	χ^2_{IP-PV}	> 4
	$\#\ (\chi^2_{IP} > 10)$	> 1
	$\sum p_T$	$> 2800\,\mathrm{MeV}/c$
	DOCA	$< 0.5\,\mathrm{mm}$
K	$DLL_{K\pi}$	> 7
π	$DLL_{K\pi}$	< 3
D^+	vertex χ^2/NDF	< 10
	DIRA	> 0.98
	χ^2_{IP}	< 12
	χ^2-distance decay vertex - PV	> 36
	χ^2_{FD}	> 125
	m	$\in (1800, 1940)\,\mathrm{MeV}/c^2$

D^+ candidates should decay at a certain distance from the PV, requirements on the χ^2 distance of the both vertices, and additionally, on the χ^2 significance of the flight distance, are applied. The direction angle (DIRA) of the D^+ candidate is the angle between its momentum and the vector defined by the PV and its decay vertex. In order to have a consistent reconstruction and to select prompt charm mesons, the cosine of this angle is required to be near 1. The reconstruction of the decay $D^+ \to \overline{K}^0\pi^+$ by the stripping is analogues to the one in the Hlt2. The applied criteria are listed in table 6.5. In addition to the already mentioned χ^2-distance to the PV, the difference in the z position between PV and D^+ decay vertex is used to ensure the existence of a secondary vertex.

6.4.2 Additional requirements

Before additional requirements are applied on the stripped data, all events are again reconstructed with the DecayTreeFitter (DTF) tool [34]. The DTF fits simultaneously the whole decay chain and certain constraints can be implemented. It is used to constrain the D^{*+} and the D^+ mesons to point back to the PV. This improves their mass resolution. For all channels, a loose selection on the fit quality of the DTF is applied to reject decays where the fit did not properly converge.

For all occurring pions, except the slow pion from the D^{*+} meson, the PID requirements applied on stripping level are tightened to reject background decays with mis-identified particles, cf. chapter 6.2.3. For the charged kaons also tighter PID requirements are imposed. Additional selection criteria explained in this section are

Table 6.5: Stripping requirements for $D^+ \to \overline{K}^0\pi^+$ candidates. They are discussed in chapter 6.4.1.

Candidate	**Variable**	**Requirement**
$\overline{K}^0 children$	track χ^2/NDF	< 4
	p_T	$> 250\,\mathrm{MeV}/c$
	p	$> 2000\,\mathrm{MeV}/c$
	χ^2_{IP}	> 40
	χ^2_{DOCA}	< 25
$\overline{K}^0$	p_T	$> 1000\,\mathrm{MeV}/c$
	χ^2_{IP}	> 7
	vertex χ^2/NDF	< 10
	χ^2-distance decay vertex - PV	> 300
	m	$\in (462, 532)\,\mathrm{MeV}/c^2$
π^+	p_T	$> 250\,\mathrm{MeV}/c$
	p	$> 2000\,\mathrm{MeV}/c$
	track χ^2/NDF	< 3
	χ^2_{IP}	> 15
	$DLL_{K\pi}$	< 0
D^+	p_T	$> 1000\,\mathrm{MeV}/c$
	χ^2_{DOCA}	< 11
	track χ^2/NDF	< 10
	m	$\in (1770, 2070)\,\mathrm{MeV}/c^2$
	χ^2_{IP}	< 15
	χ^2-distance decay vertex - PV	> 5
	$z(D^+) - z(PV)$	> 10

listed in table 6.6.

To reduce the combinatorial background, the mass of the reconstructed D^0 candidate is required to be in a $34\,\mathrm{MeV}/c^2$ mass window around the D^0 nominal mass. A fit to the mass difference Δm between the D^{*+} and the D^0 meson is used to determine the signal yield. Therefore, no tight requirements are applied. The threshold of this mass difference is the pion mass $m_{\pi^+} = 139.57\,\mathrm{MeV}/c^2$ [11]. Since Δm is hard to model near this threshold, it is restricted to the window between $139.77\,\mathrm{MeV}/c^2$ and $151.57\,\mathrm{MeV}/c^2$. This corresponds to [$0.2\,\mathrm{MeV}/c^2$,$12\,\mathrm{MeV}/c^2$] above the threshold. The signal yield of the D^+ decays is obtained by a fit to the mass distribution of the charm meson candidates. Due to the DTF the original D^+ mass window from the stripping selection is smeared. This causes the edge regions of the mass distribution to be hard to model. Therefore, the slightly narrower mass window 1820-1920 MeV/c^2 is chosen.

Table 6.6: Additional requirements applied after the stripping for all decay channels. An additional kinematic selection is presented in table 6.7.

	$\boldsymbol{D^0 \to K^-\pi^+ / \pi^-\pi^+}$	
Candidate	**Variable**	**Requirement**
D^{*+}	χ^2_{DTF}	$\in (0, 750)$
	Δm	$\in (139.77, 151.57)\,\mathrm{MeV}/c^2$
K^-K^+	$m(K^-K^+)$	$\in (1850, 1884)\,\mathrm{MeV}/c^2$
$K^-\pi^+$	$m(K^-\pi^+)$	$\in (1850, 1884)\,\mathrm{MeV}/c^2$
K	$\mathrm{DLL}_{K\pi}$	> 7
π	$\mathrm{DLL}_{K\pi}$	< -7

	$\boldsymbol{D^+ \to K^-\pi^+\pi^+}$	
Candidate	**Variable**	**Requirement**
D^+	χ^2_{DTF}	$\in (0, 750)$
$K^-\pi^+\pi^+$	$m(K^-\pi^+\pi^+)$	$\in (1820, 1920)\,\mathrm{MeV}/c^2$
K	$\mathrm{DLL}_{K\pi}$	> 7
π	$\mathrm{DLL}_{K\pi}$	< -7

	$\boldsymbol{D^+ \to \overline{K}^0\pi^+}$	
Candidate	**Variable**	**Requirement**
D^{*+}	χ^2_{DTF}	$\in (0, 750)$
$\overline{K}^0\pi^+$	$m(\overline{K}^0\pi^+)$	$\in (1820, 1920)\,\mathrm{MeV}/c^2$

6.4.3 Kinematic ranges

As will be discussed in chapter 8, it is important that the distributions of the particles, whose detection or production asymmetries are meant to cancel, agree. Therefore, an adjustment of different momentum requirements between the different decay channels is necessary. Especially, the Hlt2 trigger requirement that at least one of the D^0/D^+ meson daughters has to trigger the event in the first software trigger stage Hlt1, imposes some selection criteria on p/p_T of this daughter particles, see table 6.1. This Hlt1 requirement allows $D^+ \to K^-\pi^+\pi^+$ decays which have a low p/p_T pion and kaon to be triggered, since also the other pion could have triggered the event in Hlt1. In contrast, no $D^0 \to K^-\pi^+$ decays where the pion and kaon have low p/p_T are triggered. This inequality can not be corrected by the kinematic weighting explained in chapter 8. Therefore, the kaons in the both channels are required to satisfy the Hlt1 trigger conditions which is a natural way to exclude these problematic events.

Additional requirements which are applied to align the already existing requirements on kinematic variables[5] are listed in table 6.7. In order to make the weighting mentioned above more effective, the low momentum pion in $D^+ \to K^-\pi^+\pi^+$ decays,

[5]They originate from selection requirements of stripping or the triggers.

Table 6.7: Additional requirements on kinematic variables to equalize already existing ones.

Decay	Candidate	Variable	Requirement
$D^+ \to K^-\pi^+\pi^+$	$\pi^+_{l.m.}/\pi^+_{h.m.}$	p	$> 5000\,\mathrm{MeV}/c$
		p_T	$> 800\,\mathrm{MeV}/c$
	$\pi^+_{l.m.}/K^-$	η	$\in (2,5)$
$D^+ \to \bar{K}^0\pi^+$	π^+	p	$> 5000\,\mathrm{MeV}/c$
		p_T	$> 800\,\mathrm{MeV}/c$

cf. 5.2.2, and the pion in $D^0 \to K^-\pi^+$ decays are required to not have triggered the event in the Hlt1. Moreover, these pions are required to have a transverse momentum smaller than $1700\,\mathrm{MeV}/c$. For a more detailed explanation of these additional requirements, see chapter 8.

6.4.4 Fiducial cuts

As was discussed in chapter 5.2.1, regions with large asymmetries in the phase space of involved particles can lead to higher order terms contributing to the raw asymmetry measured in a given channel. Especially, charged particles with low momentum can exhibit regions with maximal asymmetry in their phase space.

In figure 6.3 the raw asymmetry of the channel $D^0 \to K^-K^+$ as a function of the slow pion momentum in z and x direction is shown. No background was subtracted since the same regions with high asymmetries are present independently of the origin of the slow pion. For small longitudinal momenta, there are prominent regions with opposite maximal asymmetry visible. In these regions, the pions of one charge are completely bent out of the detector and are, therefore, not detected.

Figure 6.3b shows the raw asymmetry for decays which have a slow pion whose momentum lies in a horizontal plane together with the beam pipe. Here, the structures parallel to the p_z axis which were already visible in figure 6.3a are more prominent. They originate from pions being bent into the beam pipe near the T-stations and, therefore, escaping the detector. Similarly to the regions at low p_z, this depends on the momenta in z and x direction and on the charge of the pion. Therefore, large asymmetries are visible.

These regions with high raw asymmetries are rejected according to a previous analysis, [35], as indicated by the black lines in figure 6.3a and 6.3b. They are parametrized by:

$$|p_x| \leq a(p_z - p_0), \tag{6.1}$$

with $a = 0.317$ and $p_0 = 2400\,\mathrm{MeV}/c$ for the regions at low p_z, and by:

$$|p_y/p_z| < 0.02 \quad \wedge \quad p_1 - b_1 p_z < |p_x| < p_2 + b_2 p_z, \tag{6.2}$$

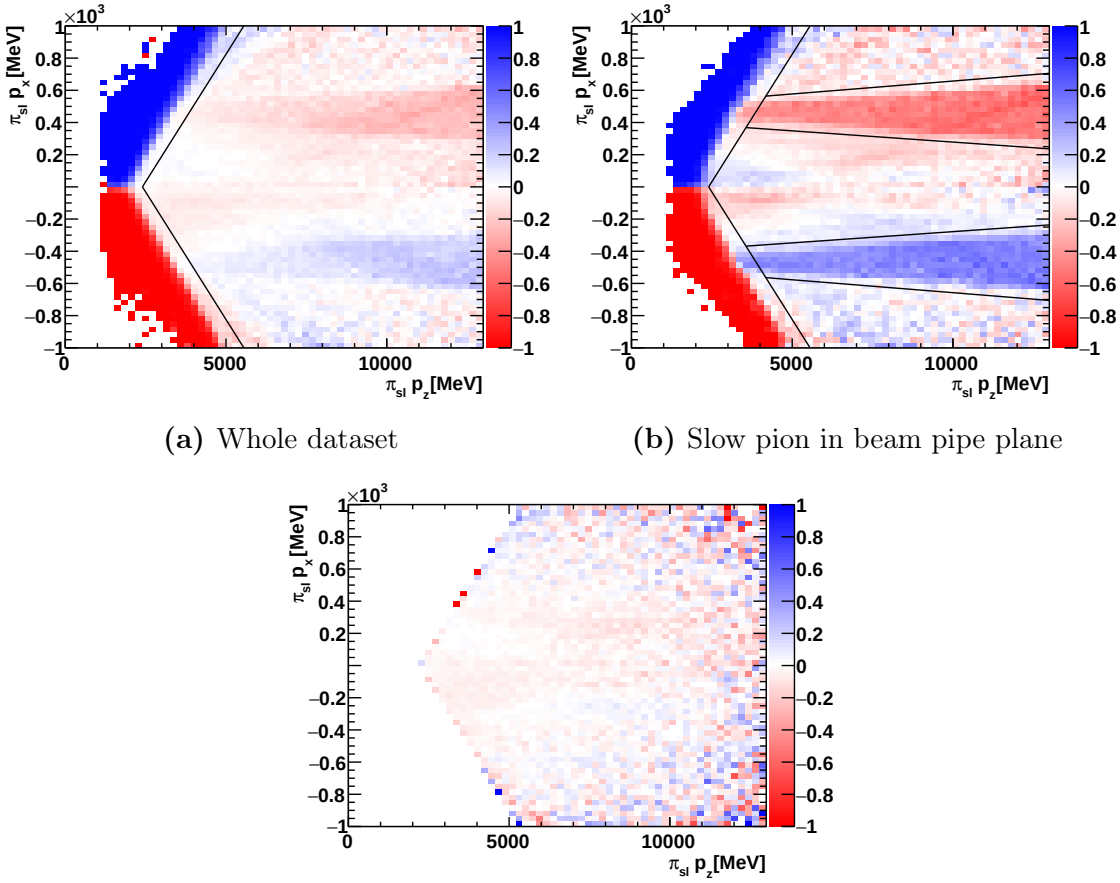

(a) Whole dataset

(b) Slow pion in beam pipe plane

(c) With fiducial regions excluded

Figure 6.3: Raw asymmetry of the channel $D^0 \to K^-K^+$ as a function of the slow pion momentum in x and y direction. The sample from 2012 with magnet polarity up is used. In figure (a) and (b), no additional requirements on top of the stripping level are applied. Figure (b) shows the asymmetry for decay candidates whose slow pion lies in horizontal plane together with the beam pipe. In figure (c) the the regions indicated by black lines in figure (a) and (b) are excluded.

with $p_1 = 418\,\mathrm{MeV}/c$, $p_2 = 497\,\mathrm{MeV}/c$, $b_1 = 0.01397$ and $b_2 = 0.016015$ for structures caused by the beam pipe. For the channel $D^0 \to K^-\pi^+$, the same regions are excluded. In figure 6.3c, these regions are excluded, and no further structures with high asymmetries are visible.

In principle, any charged final state particle which is not part of a CP even or odd final state could have such phase space regions with large detection asymmetries. But since the other charged particles have higher momenta, no such prominent structures are expected. Anyhow, their influence will be studied as a systematic uncertainty in chapter 11.3.

Table 6.8: Signal yields of the four channels for each of the four data categories. They are obtained by the fit described in chapter 7.

Channel	**2011 up**	**2011 down**	**2012 up**	**2012 down**	**Sum**
$D^0 \to K^+K^-$	643 k	918 k	1.82 M	1.87 M	5.26 M
$D^0 \to K^-\pi^+$	1.38 M	1.97 M	3.75 M	3.92 M	11.0 M
$D^+ \to K^-\pi^+\pi^+$	633 k	904 k	2.38 M	2.48 M	6.40 M
$D^+ \to \overline{K}^0\pi^+$	365 k	525 k	1.41 M	1.44 M	3.73 M

6.5 Event yields

The full data sets recorded in 2011 and 2012 are used for this analysis. They correspond to an integrated luminosity of $1\,\text{fb}^{-1}$ and $2\,\text{fb}^{-1}$ respectively. Due to the higher centre-of-mass energy in 2012, the doubled luminosity results in more than the doubled signal yields. In 2011, approximately two thirds of the data was recorded with magnet polarity down, whereas in 2012 both magnet polarities were approximately used in the same amount.

Figure 6.4 shows the invariant mass (difference) distribution of the different charm decays. Especially the channel $D^+ \to K^-\pi^+\pi^+$ shows hardly any background contribution, but also in the other channels the background is strongly suppressed. The signal yields of all channels for the different data categories are listed in table 6.8. The differences between the different channels reflect the different branching ratios and selection criteria. Especially, the chosen HLT1 trigger configuration reduces the statistic of the channels $D^0 \to K^-\pi^+$ and $D^+ \to K^-\pi^+\pi^+$. Nevertheless, the Cabibbo-suppressed decay $D^0 \to K^-K^+$ shows lower signal yields. The reason for the $D^+ \to \overline{K}^0\pi^+$ channel having the least statistics, is the small reconstruction efficiency of the neutral kaons. Most of them decay outside the VELO, and are not reconstructed as long tracks.

Since the statistical uncertainty of the raw asymmetries are approximately proportional to $1/\sqrt{N_{sig}}$, the channel with the neutral kaon will contribute most to the final statistical uncertainty. It should be mentioned, that the weighting procedure, which is explained in chapter 8, changes the effective signal yields.

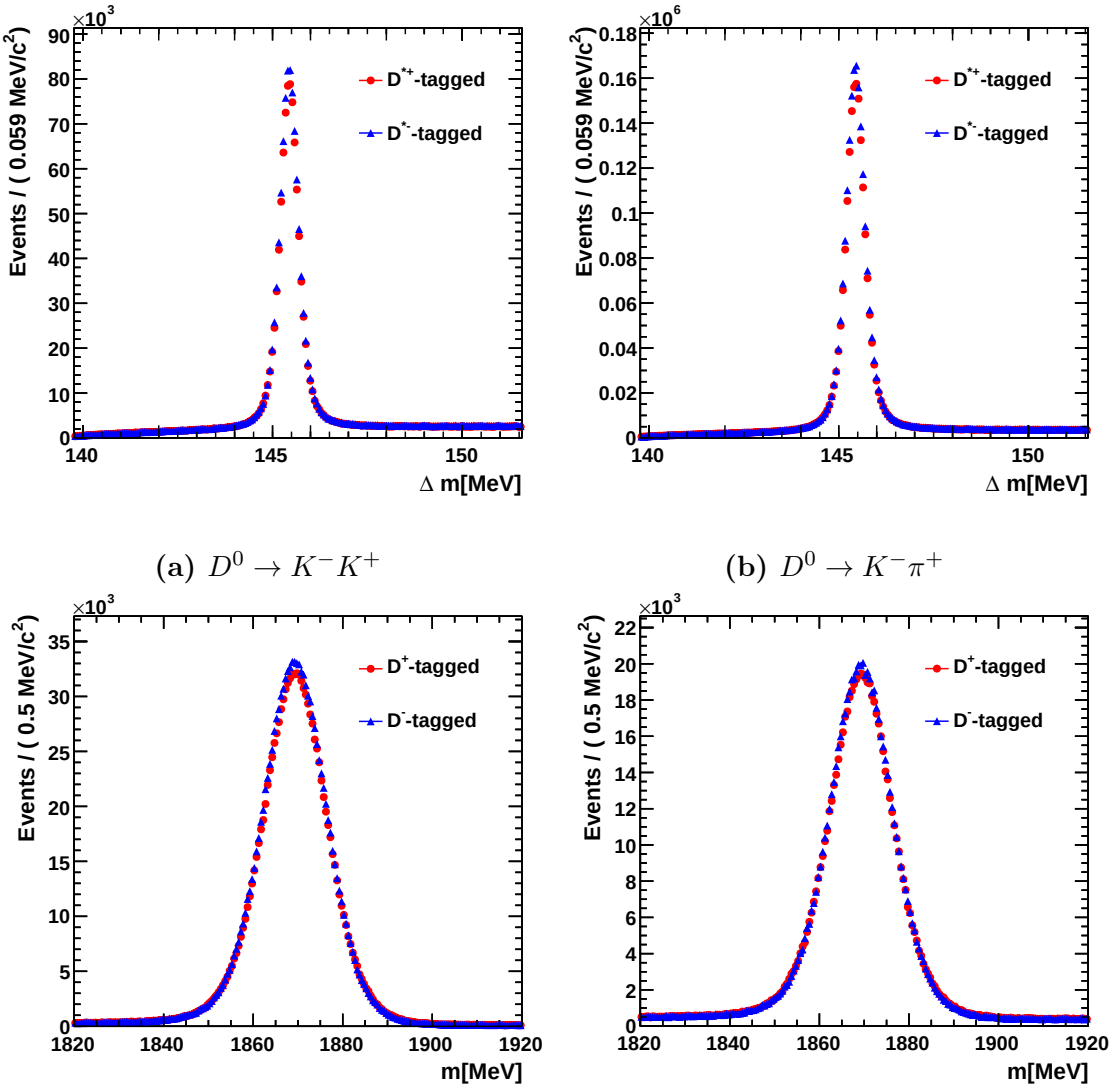

(a) $D^0 \to K^-K^+$ (b) $D^0 \to K^-\pi^+$

(c) $D^+ \to K^-\pi^+\pi^+$ (d) $D^+ \to \overline{K}^0\pi^+$

Figure 6.4: Mass distributions of the selected candidates for each of the four used charm decays. The two flavour categories are shown in red and blue. The data collected in 2012 with magnet polarity up are shown as an example.

Chapter 7

Asymmetry fits

The raw asymmetries as introduced in chapter 5.2 are obtained by binned likelihood fits. For the D^+ decays, the invariant mass distribution of the charm meson is used, whereas signal yields of the D^0 decays are obtained with a fit to the distribution of the measured mass difference between the reconstructed masses of the D^{*+} and D^0 mesons. By using this mass difference, Δm, the influence of the finite resolution of the D^0 meson mass on the D^{*+} meson mass is cancelled. This results in a narrower signal peak and increases the signal over background ratio.

This chapter first presents an introduction of maximum likelihood fits and then provides the description of the different fit models. After showing some example fits, the measured raw asymmetries and their dependence on kinematic variables of the involved particles are presented.

7.1 Maximum likelihood fits

Given an known distribution of measured observables, $\vec{x} = x_1, x_2, ..$, and a probability density function (PDF) which has several free parameters, $\vec{\lambda} = \lambda_1, \lambda_2, ..$, and is meant to describe the observed distribution, a maximum likelihood fit can be used to determine the unknown free parameters of the PDF [36]. The PDF, $\mathcal{P}(\vec{x}_i|\vec{\lambda})$, gives the probability for a certain configuration of the observables, $\vec{x}_i$, for a given set of parameters $\vec{\lambda}$.

The likelihood function can be defined as the product of the probabilities of all N measurements:

$$\mathcal{L}(\vec{x}_i|\vec{\lambda}) = \prod_{i=1}^{N} \mathcal{P}(\vec{x}_i|\vec{\lambda}). \tag{7.1}$$

Therefore, the likelihood function gives a measure of the probability for a parameter set $\vec{\lambda}$ to describe the measured data. By maximizing the likelihood value, one can obtain values for the parameters. In general, the data don't have to be divided into bins since the likelihood value can be calculated measurement by measurement. This is then called an unbinned maximum likelihood fit. Anyhow, using binned data and, therefore, performing a binned maximum likelihood fit, has computational advantages.

7.2 Fit models

In order to obtain the raw asymmetry, the respective dataset has to be divided into positively and negatively tagged decays, see figure 6.4. The charge of the slow pion and the reconstructed D^+/D^- meson, respectively, is used to tag the flavour of the D^0 meson at production. Then, a simultaneous fit of both categories is performed. Some parameters are shared and the asymmetry is extracted as a free parameter in the fit. Using the asymmetry, A_{raw}, and the total signal yield, N_{sig}, as parameters of the fit, the number of signal candidates, $N^{\pm}_{sig}$, of the respective category is given by:

$$N^{\pm}_{sig} = \frac{N_{sig}(1 \mp A_{raw})}{2}. \tag{7.2}$$

The asymmetry of the background A_{bkg} is analogously implemented and connected to the number of background candidates $N^{\pm}_{bkg}$ in the respective category. Then, the final PDF $\mathcal{P}^{\pm}$ of the individual category can be written as:

$$\mathcal{P}^{\pm} = N^{\pm}_{sig}\mathcal{P}^{\pm}_{sig} + N^{\pm}_{bkg}\mathcal{P}^{\pm}_{bkg}. \tag{7.3}$$

$\mathcal{P}^{\pm}_{sig}$ and $\mathcal{P}^{\pm}_{bkg}$ are the PDFs of the signal and background distributions which are described in the following for the different channels. For all of the following PDFs, a factor which normalises the distribution to 1 is implied.

7.2.1 D^{*+} decays

For the $D^{*+} \to D^0\pi^+_{sl}$ decays, the Δm distribution has to be modelled, see figure 6.4. The same model is used for the Cabibbo-suppressed and the Cabibbo-favoured decay. For the background, $\mathcal{P}_{bkg}$, an empirical function consisting out of the product of an exponential function and a power law function modelling the phase-space threshold [37]:

$$\mathcal{P}_{bkg}(\Delta m|A, B, \Delta m_0) \propto (\Delta m - \Delta m_0)^A \, exp[(-B\Delta m - \Delta m_0)], \tag{7.4}$$

is used, with Δm_0 parametrizing the threshold and A, B being two shape parameters. Whereas Δm_0 is fixed to the pion mass, $\Delta m_0 = 139.57\,\mathrm{MeV}/c^2$ [11], A and B are determined by the fit. All parameters are shared between the two categories and therefore:

$$\mathcal{P}^{-}_{bkg} = \mathcal{P}^{+}_{bkg}. \tag{7.5}$$

The signal shape, $\mathcal{P}_{sig}$, is parametrized by the sum of three Gaussian distributions, G_1, G_2 and G_3. This specific choice is based on a previous analysis presented in [32]. Beside the normalization factor, a Gaussian function is given by:

$$G_i(\Delta m|\mu_i, \sigma_i,) \propto exp\left[-\frac{(\Delta m - \mu_i)^2}{2\sigma_i}\right], \tag{7.6}$$

where μ and σ parametrize the mean and the width of the function. Two of the Gaussian distributions are required to have the same mean parameter μ_1. The broadest Gaussian distribution is allowed to have a different mean parameter μ_2. Additionally, the mean parameters can be different for the two tags. All width parameters are scaled by the parameter ω with respect to the width parameters of the events with the opposite flavour such that:

$$\sigma_i^- = \omega\sigma_i^+. \tag{7.7}$$

All other signal shape parameters are shared between the two data categories. In total, the signal PDFs can then be written as:

$$\begin{aligned}\mathcal{P}_{sig}^+ =& f_1 G_1(\Delta m|\mu_1^+, \sigma_1^+) \\ &+ (1-f_1)[f_2 G_2(\Delta m|\mu_1^+, \sigma_2^+) + (1-f_2)G_3(\Delta m|\mu_2^+, \sigma_3^+)],\end{aligned} \tag{7.8}$$

$$\begin{aligned}\mathcal{P}_{sig}^- =& f_1 G_1(\Delta m|\mu_1^-, \omega\sigma_1^+) \\ &+ (1-f_1)[f_2 G_2(\Delta m|\mu_1^-, \omega\sigma_2^+) + (1-f_2)G_3(\Delta m|\mu_2^-, \omega\sigma_3^+)].\end{aligned} \tag{7.9}$$

The parameters f_1 and f_2 parametrize the relative fractions of the signal components and are also shared between the two data categories split by flavour.

7.2.2 D^+ decays

The background distribution of the D^+ meson mass, m_{D^+}, is described by a single exponential function with the decay constant C:

$$\mathcal{P}_{bkg}(m_{D^+}|C) \propto exp[-Cm_{D^+}]. \tag{7.10}$$

As for the D^{*+} decays, the background parameter is shared between the two tags.

For the signal shape, the sum of two Gaussian distributions and a bifurcated Gaussian distribution is chosen. This specific choice is motivated by a previous analysis presented in [5] and by testing different models. The bifurcated Gaussian distribution is necessary in order to describe the asymmetric mass distribution arising from final state radiation. Apart from the correct normalization, it can be written as:

$$BG(m_{D^+}|\mu, \sigma_L, \sigma_R) \propto \begin{cases} exp\left[-\frac{(m_{D^+}-\mu)^2}{2\sigma_L}\right] & \text{for } m_{D^+} < \mu \\ exp\left[-\frac{(m_{D^+}-\mu)^2}{2\sigma_R}\right] & \text{for } m_{D^+} > \mu \end{cases}. \tag{7.11}$$

Here σ_L and σ_R are the width of the left and right half-Gaussian distribution, respectively. Similarly to the D^0 decays, the three signal PDFs have a common mean and scaled widths for the two categories. Therefore, the final signal PDFs are given by:

$$\begin{aligned}\mathcal{P}_{sig}^+ =& f_1 BG(m_{D^+}|\mu^+, \sigma_L^+, \sigma_R^+) \\ &+ (1-f_1)[f_2 G_1(m_{D^+}|\mu^+, \sigma_1^+) + (1-f_2)G_2(m_{D^+}|\mu^+, \sigma_2^+)],\end{aligned} \tag{7.12}$$

$$\begin{aligned}\mathcal{P}_{sig}^- =& f_1 BG(m_{D^+}|\mu^-, \omega\sigma_L^+, \omega\sigma_R^+) \\ &+ (1-f_1)[f_2 G_1(m_{D^+}|\mu^-, \omega\sigma_1^+) + (1-f_2)G_2(m_{D^+}|\mu^-, \omega\sigma_2^+)],\end{aligned} \tag{7.13}$$

where ω again is the width scale factor between the two categories, and f_i the relative fractions of the signal components. The latter are required to be the same for both categories.

The chosen PDFs are only one of many possibilities. Therefore, the systematic effects of making this specific choice has to be studied. This is done by testing other signal and background PDFs and is discussed in chapter 11.1.

7.3 Example fits

Since unbinned likelihood fits are time-consuming for the high statistics used in this analysis, only binned likelihood fits are used. By default, each flavour-tagged sample is divided into 200 bins. By using such a high number of bins, no difference to an unbinned fit is expected. Anyhow, the impact of the chosen number of bins is tested in chapter 11.1.

In order to demonstrate and discuss the performance of the fits, the results for the data category 2012 magnet polarity up are shown in Fig 7.1 to 7.4 for the four decay channels. Besides the fit projections for both tags, the asymmetry between the positive and negative events, overlaid with the fit projection is shown. To estimate the quality of the fit, for each bin the so-called pull can be calculated as

$$\text{pull}_i = \frac{y_i^{\text{data}} - y_i^{\text{pdf}}}{\sigma_i}, \tag{7.14}$$

with y_i^{data} and y_i^{pdf} being the content of bin i for data and the value of the obtained PDF at this position. The deviation of the data from the PDF is normalized to the uncertainty σ_i of the respective bin content. If the chosen PDF would describe data perfectly, these pulls would be normally distributed around 0. The χ^2/ndf value, given by

$$\chi^2/\text{ndf} = \frac{1}{\text{ndf}} \sum_i \text{pull}_i, \tag{7.15}$$

is a good measure for the deviation from this ideal case. The number of degrees of freedom, ndf, is given by the number of bins subtracted by the number of model parameters. A χ^2/ndf value larger than 1 is an evidence for a model, that does not describe the data in full detail. Additionally, the probability p(χ^2,ndf) for the obtained χ^2/ndf value or a higher one, given that the PDF does describe the data perfectly, can be calculated. These values are calculated for the actual fit and the asymmetry, see figure 7.1 to 7.4.

Besides the channel $D^+ \to \overline{K}^0\pi^+$, the obtained p-values of the actual fits are near zero and also the pull distributions show clear structures. The asymmetry distributions show much better p-values between 0.03 and 0.62. Since only the asymmetry is the quantity of interest, it is not strictly required to have a high p-value for the actual fit, but only for the asymmetry. Anyhow, also the pull distributions

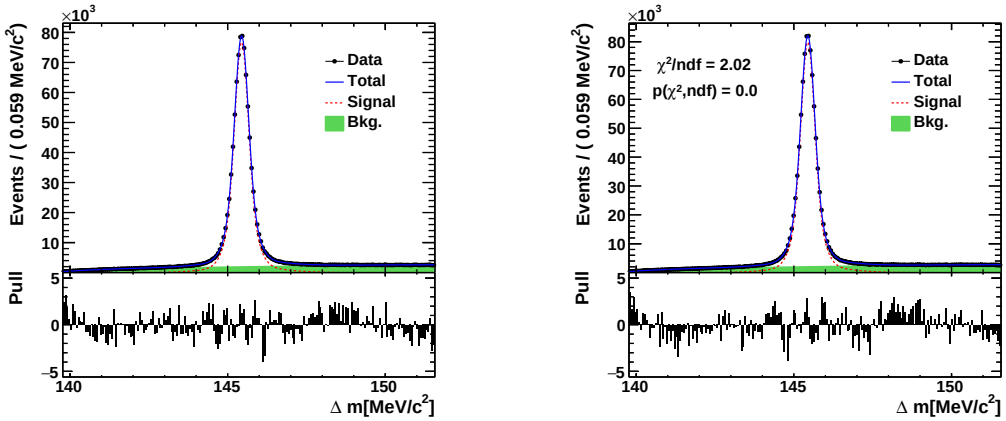

(a) Negatively tagged

(b) Positively tagged

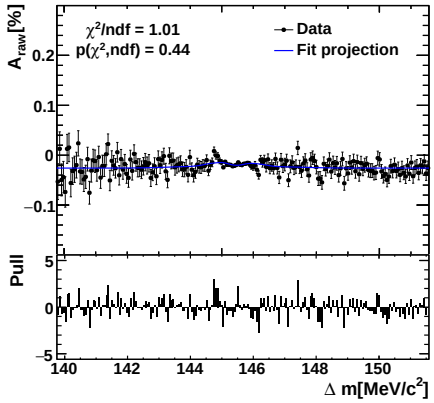

(c) Asymmetry

Figure 7.1: Fit results for the channel $D^0 \to K^-K^+$ using data from 2012 with magnet polarity up. The asymmetry (c) between negative (a) and positive (b) tagged decays is shown. A χ^2 value and the according p-value is given for the actual fit and the obtained asymmetry. The values quoted in the diagram of positively tagged decays refer to the combination of both tags.

of the asymmetries show slight structures and the obtained p-values tend to be to small. Therefore, additional studies on the impact of the chosen fit model are necessary. This is done in chapter 11.1.

7.4 Raw asymmetries

The extracted raw asymmetries are presented here. After a qualitative discussion of the influence of the different individual asymmetries, the dependence on some kinematic variables is shown. The latter is meant to motivate the kinematic weighting explained in chapter 8 which is one of the crucial parts of this analysis.

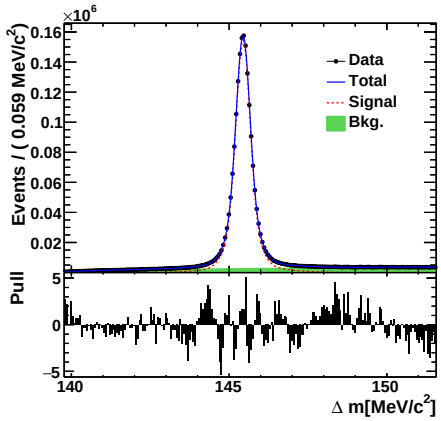

(a) Negatively tagged

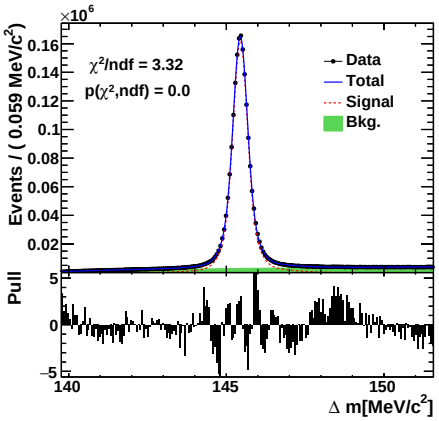

(b) Positively tagged

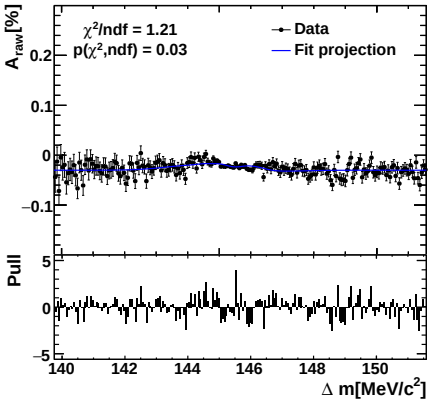

(c) Asymmetry

Figure 7.2: Fit results for the channel $D^0 \to K^-\pi^+$ using data from 2012 with magnet polarity up. The asymmetry (c) between negative (a) and positive (b) tagged decays is shown. A χ^2 value and the according p-value is given for the actual fit and the obtained asymmetry. The values quoted in the diagram of positively tagged decays refer to the combination of both tags.

7.4.1 Extracted raw asymmetries

All extracted asymmetries are listed in table 7.1. The difference between the two magnet polarities and the different channels can be used to qualitatively describe the contribution of the individual nuisance asymmetries.

For both data taking periods, the raw asymmetry of the channel $\boldsymbol{D^0 \to K^-K^+}$ shows a huge difference between the magnet polarities. The only asymmetry affecting this channel which is expected to change sign with magnet polarity is the detection asymmetry of the slow pion. Therefore, this asymmetry is approximately half the difference between the magnet up and magnet down raw asymmetry and of the order of 0.8%. The polarity averaged part of the asymmetry in this channel is of the order of 1%. When neglecting a possible CP violation, this can be explained by

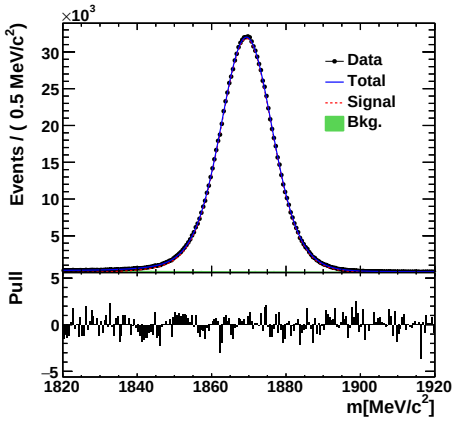

(a) Negatively tagged

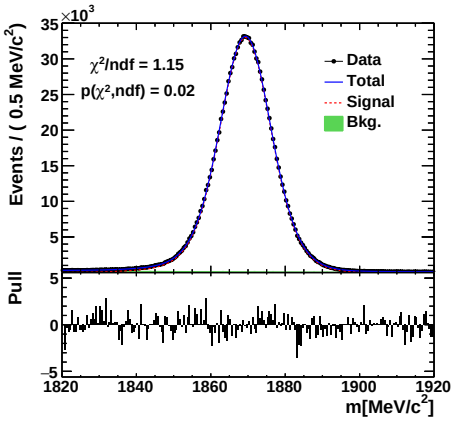

(b) Positively tagged

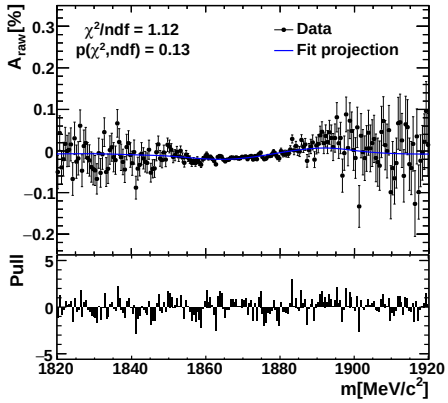

(c) Asymmetry

Figure 7.3: Fit results for the channel $D^+ \to K^-\pi^+\pi^+$ using data from 2012 with magnet polarity up. The asymmetry (c) between negative (a) and positive (b) tagged decays is shown. A χ^2 value and the according p-value is given for the actual fit and the obtained asymmetry. The values quoted in the diagram of positively tagged decays refer to the combination of both tags.

the production asymmetry of the charged charm meson D^{*+} which is expected to be of this order, cf. chapter 5.1.1. Part of this polarity averaged asymmetry could also be a residual component of the slow pion detection asymmetry. Due to its low momentum, the slow pion is very sensitive to possible detector asymmetries. These asymmetries of the detector do not have to be exactly the same for the magnet up and magnet down periods. Therefore, the slow pion detection asymmetry can also affect the polarity averaged raw asymmetry.

The channel $\boldsymbol{D^0 \to K^-\pi^+}$ shows the same behaviour when flipping the magnet polarity, see table 7.1. However, the polarity averaged asymmetry is approximately twice as large as for the $D^0 \to K^-K^+$ channel. This additional asymmetry has to come from the kaon and it is as expected, cf. chapter 5.1.2, also of the order of 1%. Whereas this polarity independent part of the kaon detection asymmetry comes from

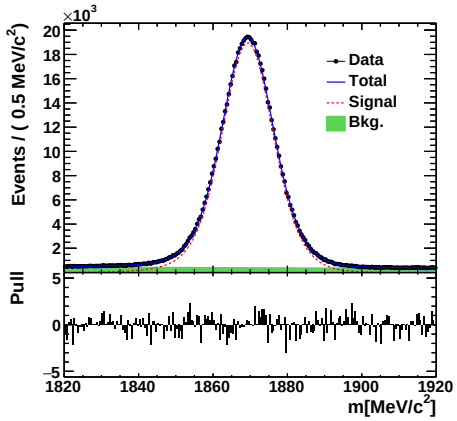

(a) Negatively tagged

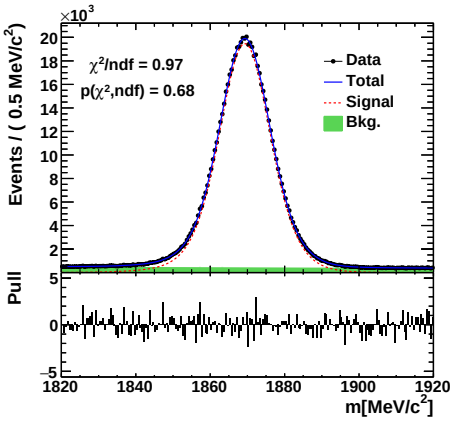

(b) Positively tagged

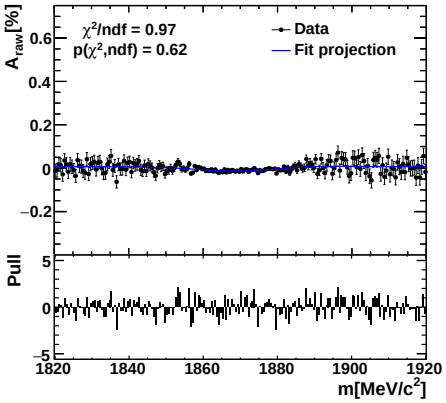

(c) Asymmetry

Figure 7.4: Fit results for the channel $D^+ \to \overline{K}^0\pi^+$ using data from 2012 with magnet polarity up. The asymmetry (c) between negative (a) and positive (b) tagged decays is shown. A χ^2 value and the according p-value is given for the actual fit and the obtained asymmetry. The values quoted in the diagram of positively tagged decays refer to the combination of both tags.

the different material interaction rates of kaons and anti-kaons, there should be an additional component coming from the instrumental asymmetries. This should be present for all charged particles, cf 5.1.2. In 2011, it seems to be of opposite sign and similar size for the K^- and π^+ in $D^0 \to K^-\pi^+$ decays since the polarity depending asymmetry is of the same order as in $D^0 \to K^-K^+$. In 2012, this is not the case and the $K^-\pi^+$ pair seems to contribute significantly to the polarity depending asymmetry. Due to the trigger selection, the pions and the kaons kinematics differ strongly. Therefore, they also tend to get detected by different parts of the detector. Thus, the detection asymmetry due to possible asymmetries of the detector can differ. Between the data taking periods 2011 and 2012 parts of the detector were repaired, or moved, and also the centre-of-mass energy was changed. These can be

Table 7.1: Extracted raw asymmetries in % for each channel and data category. The averaging of magnet polarity up and down and the two data taking periods is done according to chapter 5.3.

2011	**up**	**down**	**mean**
$A_{raw}(D^0 \to K^+K^-)$	-1.81 ± 0.13	-0.16 ± 0.11	-0.986 ± 0.088
$A_{raw}(D^0 \to K^-\pi^+)$	-2.964 ± 0.090	-1.401 ± 0.076	-2.183 ± 0.059
$A_{raw}(D^+ \to K^-\pi^+\pi^+)$	-2.35 ± 0.13	-1.58 ± 0.11	-1.965 ± 0.084
$A_{raw}(D^+ \to \overline{K}^0\pi^+)$	-1.27 ± 0.18	-0.35 ± 0.15	-0.81 ± 0.11
2012	**up**	**down**	**mean**
$A_{raw}(D^0 \to K^+K^-)$	-1.746 ± 0.080	-0.189 ± 0.079	-0.967 ± 0.056
$A_{raw}(D^0 \to K^-\pi^+)$	-2.104 ± 0.055	-1.785 ± 0.054	-1.945 ± 0.039
$A_{raw}(D^+ \to K^-\pi^+\pi^+)$	-1.470 ± 0.067	-1.916 ± 0.065	-1.693 ± 0.047
$A_{raw}(D^+ \to \overline{K}^0\pi^+)$	-0.952 ± 0.091	-0.650 ± 0.090	-0.801 ± 0.064
2011 + 2012	**up**	**down**	**mean**
$A_{raw}(D^0 \to K^+K^-)$	-1.763 ± 0.069	-0.180 ± 0.065	-0.973 ± 0.056
$A_{raw}(D^0 \to K^-\pi^+)$	-2.338 ± 0.047	-1.656 ± 0.044	-2.016 ± 0.039
$A_{raw}(D^+ \to K^-\pi^+\pi^+)$	-1.655 ± 0.059	-1.827 ± 0.056	-1.757 ± 0.047
$A_{raw}(D^+ \to \overline{K}^0\pi^+)$	-1.020 ± 0.081	-0.569 ± 0.077	-0.804 ± 0.064

reasons for the different polarity depending asymmetries of the $K^-\pi^+$ pair in the periods 2011 and 2012.

By looking at the raw asymmetries of the $\boldsymbol{D^+ \to \overline{K}^0\pi^+}$ decays, one can determine the production asymmetry of the charged charm meson to be of the order of 0.8%. This differs slightly from the value obtained for the decay $D^0 \to K^-K^+$, which could result from differences in the kinematic distributions or, as discussed previously, from a residual detection asymmetry of the slow pion. The neutral kaon asymmetry, cf. channel 9, can be neglected in this qualitative discussion. In 2011, the pion detection asymmetry, which is responsible for the polarity depending part, is of the order of 0.5%, whereas in 2012, it seems to be smaller. Reasons for this can be found above.

Finally, the channel $\boldsymbol{D^+ \to K^-\pi^+\pi^+}$ shows a polarity independent asymmetry coming from the detection asymmetry of the kaon and the production asymmetry of the D^+ meson. With approximately 1.8% it perfectly fits to the previous mentioned numbers. In 2011 where the $K^-\pi^+$ pair induces no additional polarity depending asymmetry, the difference between polarity up and down is of the same order as in the $D^+ \to \overline{K}^0\pi^+$ channel and can be explained by the second pion. In contrast to that, in 2012 the $K^-\pi^+$ pair contributes to the polarity depending asymmetry and the second pion has a smaller effect. Therefore, the polarity dependence is quite different between 2011 and 2012 for the $D^+ \to K^-\pi^+\pi^+$ channel.

It should be mentioned, that the numbers presented in this discussion are only meant to give order of magnitudes and are used to visualize the occurring asymme-

tries.

7.4.2 Dependence on kinematic variables

As already discussed in chapter 5.1, the individual detection and production asymmetries are expected to depend on the kinematic variables of the involved particles. Thus, the raw asymmetries are now shown as function of some of these variables.

The channel $\boldsymbol{D^0 \to K^-\pi^+}$ has the largest yield after the selection. Therefore, in this channel, the measured dependencies on the kinematic variables are least affected by statistical fluctuations. Thus, it is used to discuss the occurring dependencies in more detail. In figure 7.5, the raw asymmetry of this channel is shown as a function of four kinematic variables. Since the kinematic variables of the involved particles are correlated, it is not possible to disentangle the influence of the different particles.

Figure 7.5a shows the raw asymmetry as a function of the pseudorapidity of the charm meson. When combining all four data sets, a clear dependence is visible. The asymmetry grows with increasing pseudorapidity. In contrast to that, the asymmetry decreases at high transverse momenta of the charm meson, see figure 7.5b. Both dependencies are expected for production asymmetries and can be explained by the MCM model discussed in chapter 5.1.1. Since the kinematics of the D^{*+} meson are strongly correlated to the slow pion, part of these dependencies could also origin from the latter. It is out of the scope of this analysis to disentangle the two sources.

When looking at the raw asymmetry in bins of the kaon momentum in figure 7.5d, a clear deviation at high values is visible. This behaviour changes sign with polarity flip and can be explained by an asymmetric efficiency of the particle identification system [5], [38]. Also the polarity depending effect at high pseudorapidity of the charm meson is probably caused by this particle identification asymmetry. As mentioned in chapter 5.1.2, one would expect a decreasing asymmetry with increasing momentum of the kaon. This is not visible for this channel. Since the kaon originates from the D^{*+} meson, their kinematics are correlated and the η-dependence of the production asymmetry of the latter could influence the dependence on the kaon momentum.

In figure 7.5c, the dependence on the azimuthal angle ϕ of the kaon is shown. A clear polarity dependant structure is visible. It originates from particles of a specific charge being bent out of the detector. This effect depends on the magnet polarity and is most distinct for the regions with $\phi = 0$ and $\phi = \pm\pi$. At $\phi = \pi/2$, the bending is fully symmetric for positively and negatively charged particles and it causes no asymmetry. When averaging the magnet polarities, this asymmetry should perfectly cancel. The remaining structure can be explained by the overlap regions of the two halves of the VELO. There, the asymmetric interaction of the kaon with the additional material causes a larger detection asymmetry. This effect is visible at $\phi = \pm\pi/2$.

Figure 7.6 shows the raw asymmetry of $\boldsymbol{D^0 \to K^-K^+}$ events as a function of some kinematic variables of the involved particles. Due to the small mass difference between the D^{*+} and the D^0 meson, the kinematics of the slow pion and the D^{*+}

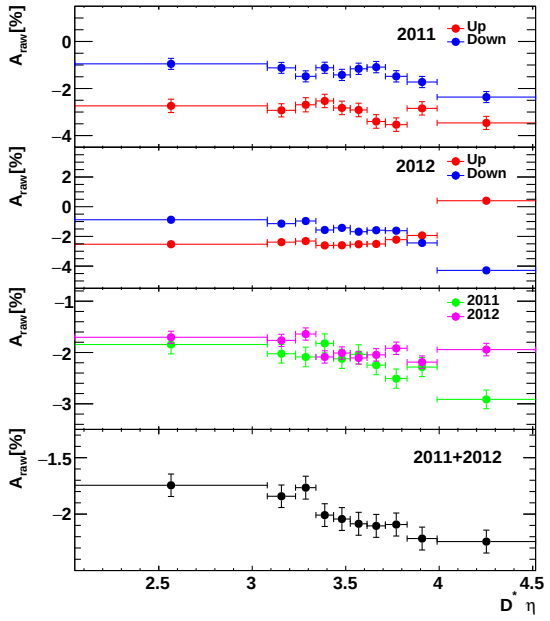

(a) $\eta(D^{*+})$

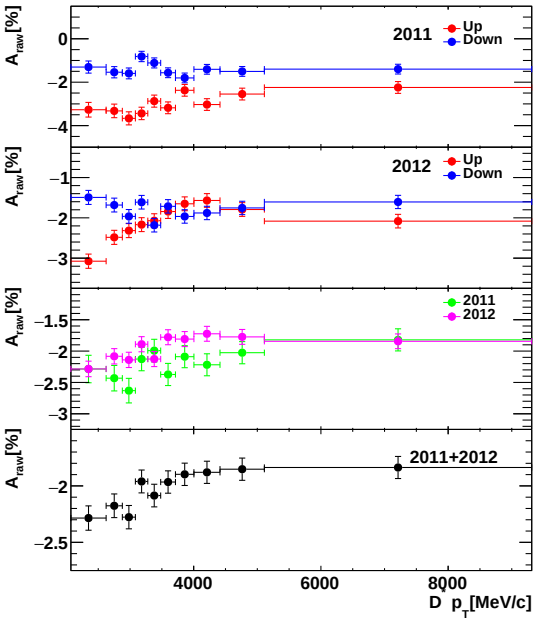

(b) $p_T(D^{*+})$

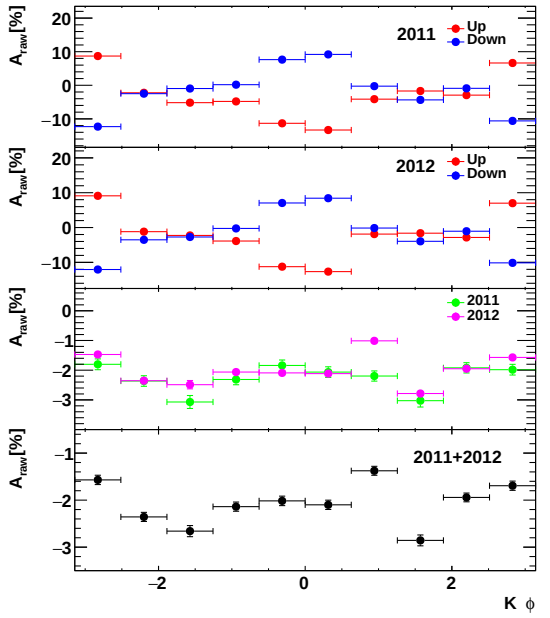

(c) $\phi(K)$

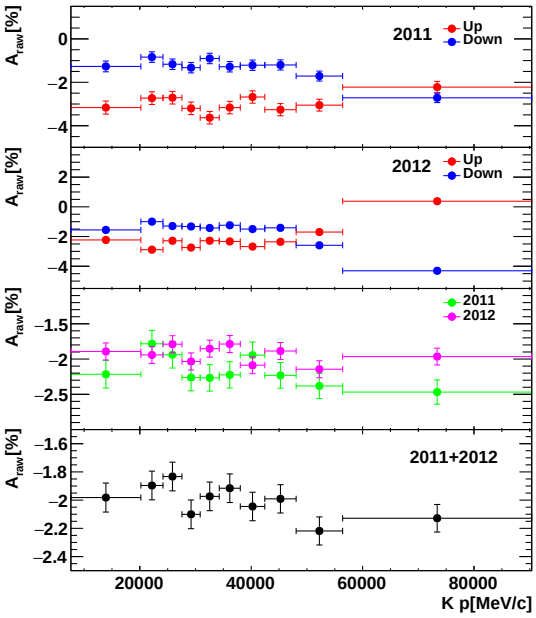

(d) $p(K)$

Figure 7.5: Raw asymmetry of $D^0 \to K^-\pi^+$ events as a function of some kinematic variables of the involved particles. Results for all four data categories and their means are shown. The values are obtained by a fit to each sub-sample. Thereby, most shape parameters were fixed to the value from the fit to the whole data set. To account for the momentum depending mass resolution, the width parameters are allowed to vary by a common factor.

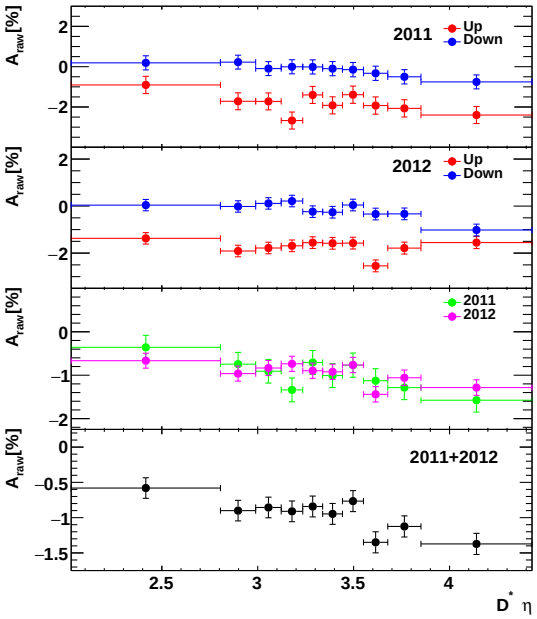

(a) $\eta(D^{*+})$

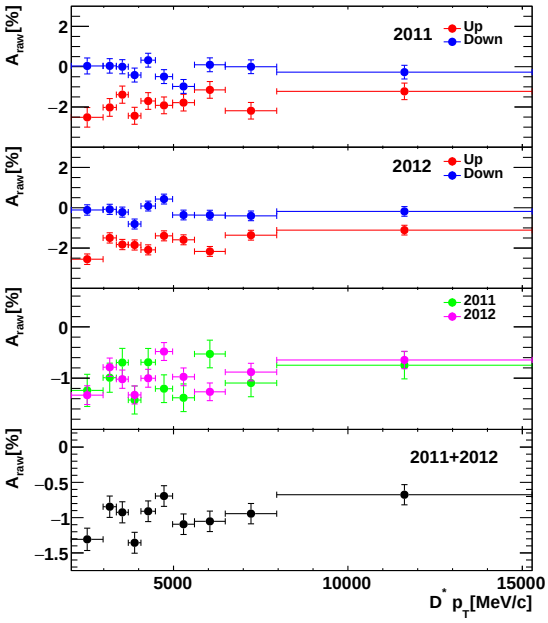

(b) $p_T(D^{*+})$

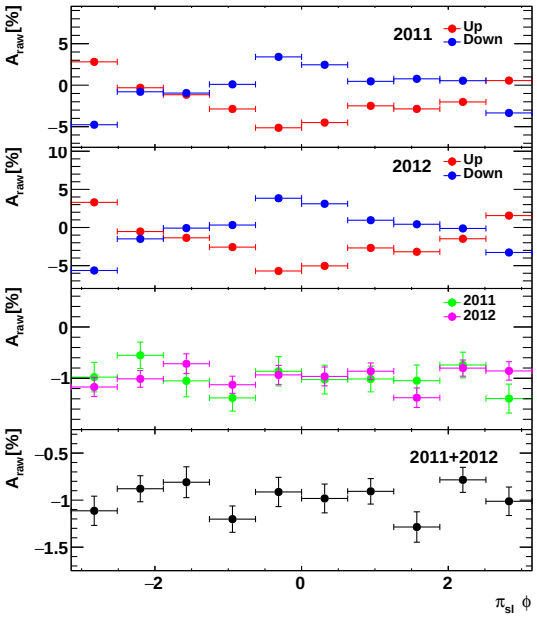

(c) $\phi(\pi_{sl})$

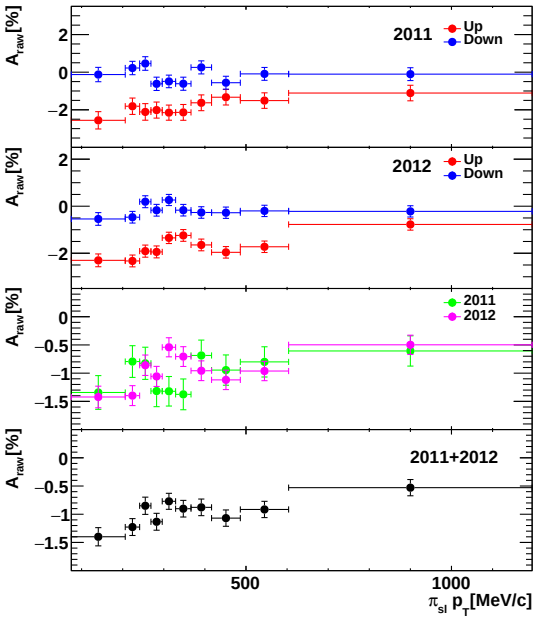

(d) $p_T(\pi_{sl})$

Figure 7.6: Raw asymmetry of $D^0 \to K^-K^+$ events as a function of some kinematic variables of the involved particles. Results for all four data categories and their means are shown. The values are obtained by a fit to each sub-sample. Thereby, most shape parameters were fixed to the value from the fit to the whole data set. To account for the momentum depending mass resolution, the width parameters are allowed to vary by a common factor.

meson are strongly correlated. Therefore, one expects similar results for the raw asymmetry dependencies for these two particles. In figure 7.6d and 7.6b, the dependencies on the transversal momentum of the slow pion and the D^{*+} meson are shown and they have a similar structure. As in the other D^0 channel, the absolute value of the asymmetry decreases with increasing transversal momentum. And, as can be seen in figure 7.6a, it increases with the growing pseudorapidity of the D^{*+} particle.

In figure 7.6c, the polarity averaged raw asymmetry shows no clear dependence on the azimuthal angle ϕ of the slow pion. Any dependence would have to come from a residual detection asymmetry of the slow pion. As for the kaon in $D^0 \to K^-\pi^+$ channel, a clear structure is visible for the individual magnet polarities.

Figure 7.7 shows the raw asymmetry of the channel $\boldsymbol{D^+ \to K^-\pi^+\pi^+}$ as a function of some kinematic variables of the involved particles. The dependence on the transverse momentum of the D^+ meson is shown in 7.7b and is analogue to the observations made for the D^0 channels. In contrast to that, in figure 7.7a the polarity averaged raw asymmetry shows no clear connection to the pseudorapidity of the charm meson. Also, the expected behaviour of the raw asymmetry with increasing momentum of the kaon, shown in figure 7.7d, is more visible than in the $D^0 \to K^-\pi^+$ channel. An explanation for these differences could be a residual detection asymmetry of the slow pion which would only affect the D^0 channel.

In figure 7.7c, a clear dependence of the polarity averaged raw asymmetry on the azimuthal angle of the "high momentum" pion, cf. chapter 5.2.2, is visible. It is not obvious where it comes from. Either it directly originates from a residual detection asymmetry of the pion, or from asymmetries of the "low momentum" pion or the kaon. After the weighting procedure, discussed in chapter 8, the kinematic distributions of the decays are equalised. Therefore, no significant residual asymmetry is expected to be present in the final measurement and it is not crucial to disentangle the different sources of the nuisance asymmetries. Thus, no further investigation of this structure is necessary.

For the channel $\boldsymbol{D^+ \to \overline{K}^0\pi^+}$, the dependencies of the raw asymmetry on some occurring kinematic variables are shown in figure 7.8. They are not discussed in detail since the yields of this channel are small and most of the structures visible in the other channels can be distorted by statistical fluctuations. Anyhow a similar behaviour in all variables as in the other D^+ channel is observed.

7.5 Summary

In this chapter, the extracting mechanism of the raw asymmetries was introduced. A simultaneous fit to positively and negatively tagged mass distributions is performed. The models for the signal and background distributions are chosen on the basis of previous analysis and on the basis of the given data. Additional systematic studies related to the choice of the data modelling are necessary and are presented in chapter 11.1. The raw asymmetries are given independently for both polarity and

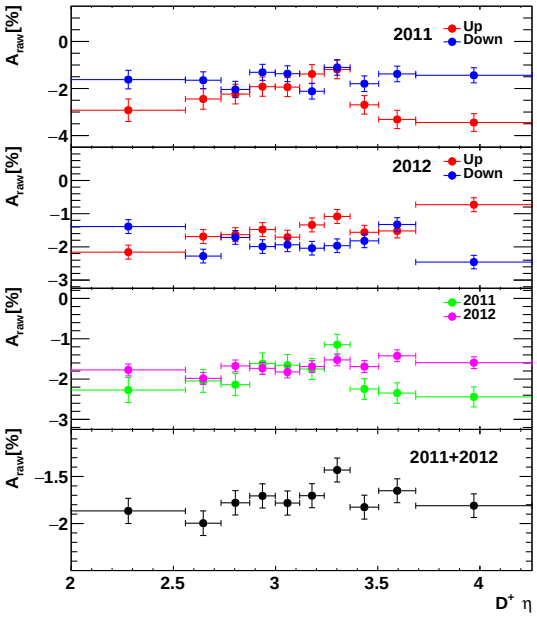

(a) $\eta(D^+)$

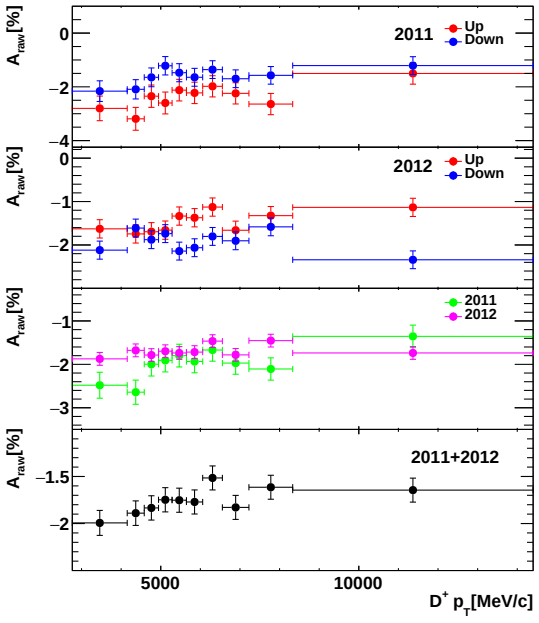

(b) $p_T(D^+)$

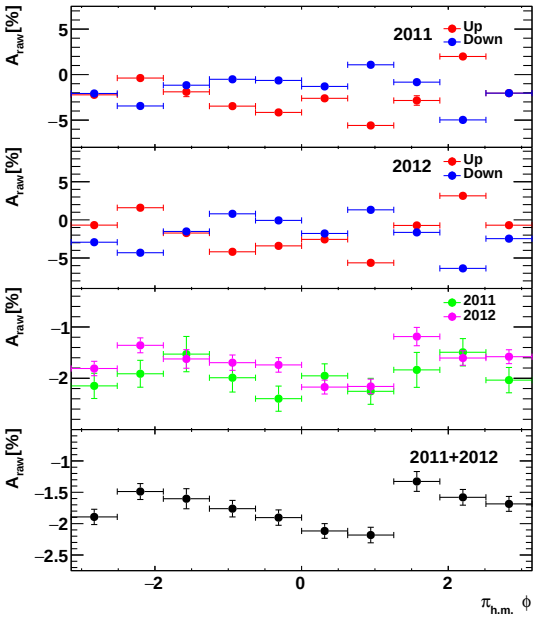

(c) $\phi(\pi)$

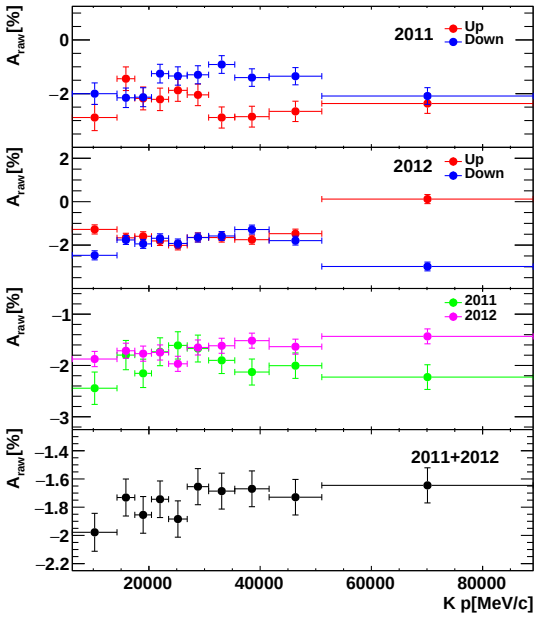

(d) $p(K)$

Figure 7.7: Raw asymmetry of $D^+ \to K^-\pi^+\pi^+$ events as a function of some kinematic variables of the involved particles. Results for all four data categories and their means are shown. The values are obtained by a fit to each sub-sample. Thereby, most shape parameters were fixed to the value from the fit to the whole data set. To account for the momentum depending mass resolution, the width parameters are allowed to vary by a common factor.

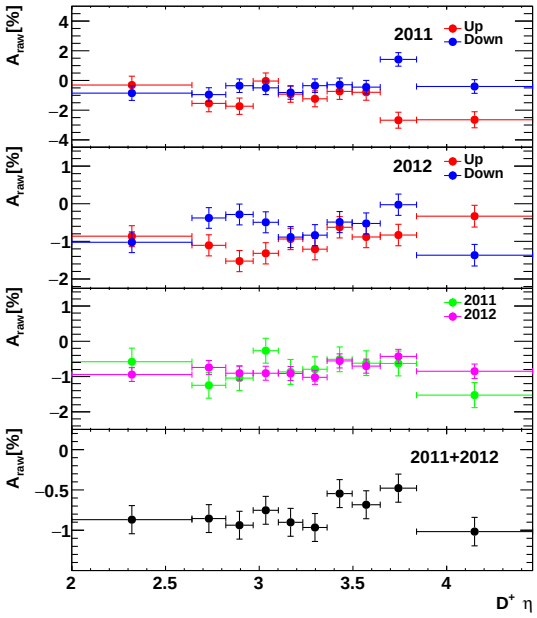

(a) $\eta(D^+)$

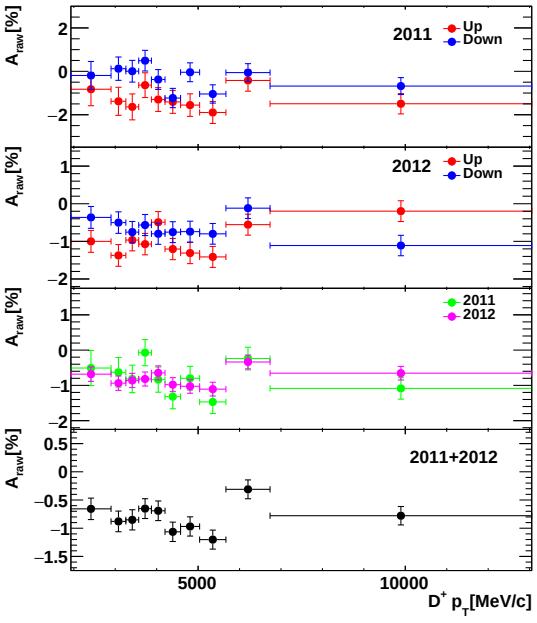

(b) $p_T(D^+)$

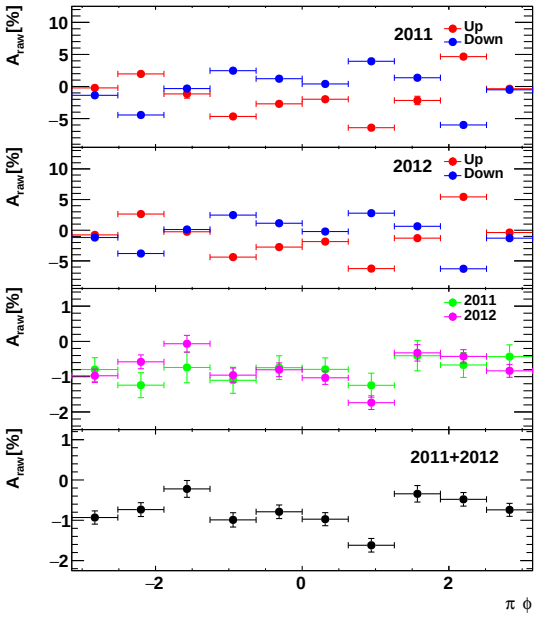

(c) $\phi(\pi)$

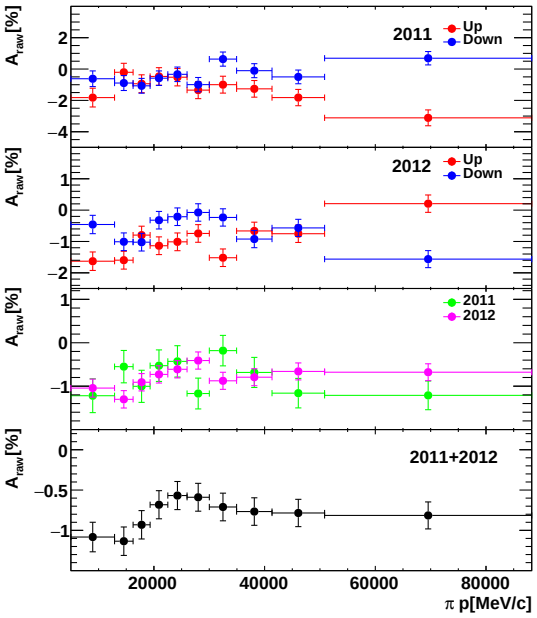

(d) $p(\pi)$

Figure 7.8: Raw asymmetry of $D^+ \to K^-\pi^+\pi^+$ events as a function of some kinematic variables of the involved particles. Results for all four data categories and their means are shown. The values are obtained by a fit to each sub-sample. Thereby, most shape parameters were fixed to the value from the fit to the whole data set. To account for the momentum depending mass resolution, the width parameters are allowed to vary by a common factor.

data taking periods. As expected, they are of the order $0.5 - 3\%$. An qualitative explanation of the individual components is possible by looking at the differences between the different channels and the different magnet polarities.

Then, the measured raw asymmetry of each channel is given as a function of some kinematic variables of the involved particles. Clear structures are visible. Although it is not possible to disentangle qualitatively the influence of the different detection and production asymmetries, possible explanations for the observed dependencies are given.

Chapter 8

Kinematic weighting

The most relevant part of this analysis is the cancellation of additional detection and production asymmetries between the different decay channels. As shown in 5.1 and 7.4.2, these asymmetries depend on kinematic variables of the involved particles. Therefore, a perfect cancellation of all nuisance asymmetries requires identical distributions in this variables for the respective channels. This is achieved by kinematically weighting the events to each other. This chapter starts with a general motivation and description of the weighting. Then, the chosen weighting strategy is motivated and the results are presented.

8.1 Motivation and formalism

This section starts with a discussion of the influence of variable detection and production asymmetries on the cancellation of this nuisance asymmetries. Then, the weighting formalism to correct for these variable asymmetries is presented.

8.1.1 Impact of kinematic distributions on the cancellation of nuisance asymmetries

The cancellation of the production asymmetry of the D^{*+} meson and the detection asymmetry of the π^+_{sl} between the two employed D^0 decays is used to explain the weighting formalism. In analogy to equation 5.12, the measured raw asymmetry in the channel $D^{*+} \to D^0(\to K^-K^+)\pi^+_{sl}$ is generally given by

$$\begin{aligned} A^{KK}_{raw} &= \int A^{KK}_{raw}(p_T^{D^*}, \eta^{D^*}, \phi^{D^*}, p_T^{\pi}, \eta^{\pi}, \phi^{\pi}) n(p_T^{D^*}, \eta^{D^*}, \phi^{D^*}) \mathrm{d}\boldsymbol{p}^{\boldsymbol{D^*}} \\ &= \int A_P^{D^*}(p_T^{D^*}, \eta^{D^*}) n_{KK}(p_T^{D^*}, \eta^{D^*}) \mathrm{d}\boldsymbol{p}^{\boldsymbol{D^*}} + \int A_D^{\pi}(p_T^{\pi}, \eta^{\pi}, \phi^{\pi}) n_{KK}(p_T^{\pi}, \eta^{\pi}, \phi^{\pi}) \mathrm{d}\boldsymbol{p}^{\boldsymbol{\pi}} \\ &\quad + A_{CP}. \end{aligned} \tag{8.1}$$

Variables labelled with a D^* in superscript describe the D^{*+} meson, and those labelled with π refer to the slow pion. A_P and A_D describe the respective production and detection asymmetries, and n^{KK} is the normalized spectrum of the respective particle. After integrating the detection asymmetry of the $K^-\pi^+$ pair, $A_D^{K\pi}$, the

measured raw asymmetry in the channel $D^{*+} \to D^0(\to K^-\pi^+)\pi^+_{sl}$ can be written analogously as

$$\begin{aligned} A^{K\pi}_{raw} &= \int A^{K\pi}_{raw}(p_T^{D^*}, \eta^{D^*}, p_T^{\pi}, \eta^{\pi}, \phi^{\pi}) n(p_T^{D^*}, \eta^{D^*}) \mathrm{d}\boldsymbol{p^{D^*}} \\ &= \int A_P^{D^*}(p_T^{D^*}, \eta^{D^*}) n_{K\pi}(p_T^{D^*}, \eta^{D^*}) \mathrm{d}\boldsymbol{p^{D^*}} + \int A_D^{\pi}(p_T^{\pi}, \eta^{\pi}, \phi^{\pi}) n_{K\pi}(p_T^{\pi}, \eta^{\pi}, \phi^{\pi}) \mathrm{d}\boldsymbol{p^{\pi}} \\ &\quad + A_D^{K\pi}. \end{aligned} \tag{8.2}$$

Therefore, one can only ensure that the detection and production asymmetries cancel if

$$\begin{aligned} n_{KK}(p_T^{D^*}, \eta^{D^*}) &= n_{K\pi}(p_T^{D^*}, \eta^{D^*}), \\ n_{KK}(p_T^{\pi}, \eta^{\pi}, \phi^{\pi}) &= n_{K\pi}(p_T^{\pi}, \eta^{\pi}, \phi^{\pi}). \end{aligned} \tag{8.3}$$

Such equations can be set up for each asymmetry which is meant to cancel when taking the difference of two raw asymmetries.

8.1.2 Weighting formalism

In order to remove the differences in distributions of kinematic variables, a weighting of the datasets is performed. Again, the two D^0 decays are used to demonstrate this procedure. When equalizing the kinematic distributions of the channels $D^0 \to K^-\pi^+$ and $D^0 \to K^-K^+$, the weights can be applied either to the $D^0 \to K^-\pi^+$ channel, or to the $D^0 \to K^-K^+$ channel, or to both. The weighting application strategy is discussed in section 8.2.

For now, an adjustment of the channel $D^0 \to K^-\pi^+$ is assumed. In principle, a simultaneous weighting in five variables, see equation 8.3, is needed since the individual kinematic variables are dependent on each other. However, the amount of available data is not sufficient to guarantee a stable weighting in more then three dimensions. Therefore, only the three kinematic variables of the D^{*+} meson[1] are used to calculate a weight $\omega(p_T^{D^*}, \eta^{D^*}, \phi^{D^*})$ which is given by

$$\omega(p_T^{D^*}, \eta^{D^*}, \phi^{D^*}) = \frac{n_{KK}(p_T^{D^*}, \eta^{D^*}, \phi^{D^*})}{n_{K\pi}(p_T^{D^*}, \eta^{D^*}, \phi^{D^*})}. \tag{8.4}$$

The normalized signal spectra of the two decays n_{KK} and $n_{K\pi}$ are obtained by unfolding the signal and background distributions with the *$_s$Plot* technique [39], see appendix C. Each decay candidate of the channel $D^0 \to K^-\pi^+$ is then weighted according to its D^{*+} candidate kinematics by this factor. After that, additional weighting steps in other kinematic variables are possible. Therefore, the already weighted distributions would be used to calculate the new kinematic weights. These would then be applied to the already weighted $D^0 \to K^-\pi^+$ decays.

[1] The reason for including ϕ of the D^{*+} meson is the same reason for performing only a weighting in D^{*+} variables and is given in the following paragraph.

In the case of the weighting between the channels $D^0 \to K^-K^+$ and $D^0 \to K^-\pi^+$, no second weighting step is necessary as it is shown in chapter 8.2. The reason for this is the strong correlation between the kinematics of the D^{*+} meson and the slow pion. This correlation can be explained by the small mass difference between the D^{*+} and the D^0 meson which only little exceeds the pion mass. Therefore, the pion and the D^{*+} meson candidates of a specific event fly almost into the same direction and it is enough to weight the events according to one of them.

When weights are applied to a dataset with N entries, the yield after weighting N_w is given by

$$N_w = \sum_{n=0}^{N} \omega_n, \tag{8.5}$$

where ω_n is the weight of the n^{th} entry which is calculated according to equation 8.4. Applying for example a weight of 2 on each entry, would cause a doubling of the yield. This would then result in a wrong uncertainty estimation of the measured raw asymmetry. Also, the presence of weights which are not uniformly distributed should lead to a reduction the statistic power of a sample. In order to get the correct yield, and therefore the right uncertainty after weighting, an additional effective weighting factor ω_{eff} is applied to each entry [5]:

$$\omega_{eff} = \frac{\sum_{n=0}^{N} \omega_n}{\sum_{n=0}^{N} \omega_n^2}. \tag{8.6}$$

The effective yield after weighting N_{eff} is then given by

$$N_{eff} = \omega_{eff} \sum_{n=0}^{N} \omega_n. \tag{8.7}$$

In the limit of equal weights for all entries, it equals the not weighted yield and one can show that non-uniform weights always reduce the effective yield.

8.2 Strategy and results

The weighting factor introduced above is responsible for a drastic reduction of statistical sensitivity when weighting datasets to each other which differ strongly in the variables used for weighting. Therefore, it is important to choose a weighting strategy where the initial distributions are already as similar as possible. This strategy is described in the first part of this section. After that, the individual weighting steps and their results are shown. Whereas the weighting formalism and the choice of the calibration channels is in close analogy to the previous analysis presented in Ref. [5], it is necessary to develop a new weighting strategy which is specific for the analysis presented in this thesis.

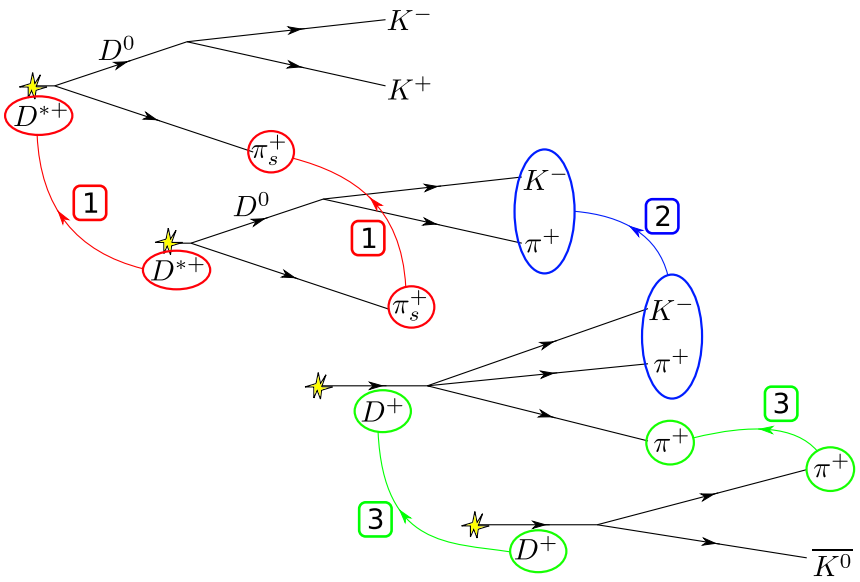

Figure 8.1: "Natural" weighting order. Each channel is weighted into the direction of the $D^0 \to K^-K^+$ channel. The numbers indicate the order and the arrows the direction of the individual weighting steps.

8.2.1 Weighting order and additional requirements

A decay channel, whose kinematic distributions have already been equalised to the kinematic distributions of another channel, cannot be compared and weighted to the kinematics of a third channel without causing discrepancies between the first two channels. Therefore, the weighting has always to be performed into the direction of one of the four channels. Two weighting directions are shown in the figures 8.1 and 8.2.

The first direction is the "natural" weighting order into the direction of the channel of interest, $D^0 \to K^-K^+$. This order was used in the previous LHCb analysis which used semileptonic b-meson decays [5]. At the first step the $D^0 \to K^-\pi^+$ channel is weighted to match the $D^0 \to K^-K^+$ channel. After that, the $D^+ \to K^-\pi^+\pi^+$ channel is weighted to the $D^0 \to K^-\pi^+$ channel using already the weights of the first step. The last step is then the analogous weighting of the channel $D^+ \to \overline{K}^0\pi^+$ to the weighted $D^+ \to K^-\pi^+\pi^+$ channel. Whereas the first two weighting steps are not problematic, the weighting of $D^+ \to \overline{K}^0\pi^+$ would result in a very small effective weighting factor when choosing this weighting order. This would reduce the statistic power of this channel to such a high degree that its statistic uncertainty on A_{raw} would be unacceptably high.

The problematic distribution causing this small effective weighting factor is the p_T distribution of the D^+ meson. In the $D^+ \to \overline{K}^0\pi^+$ channel, the D^+ meson tends

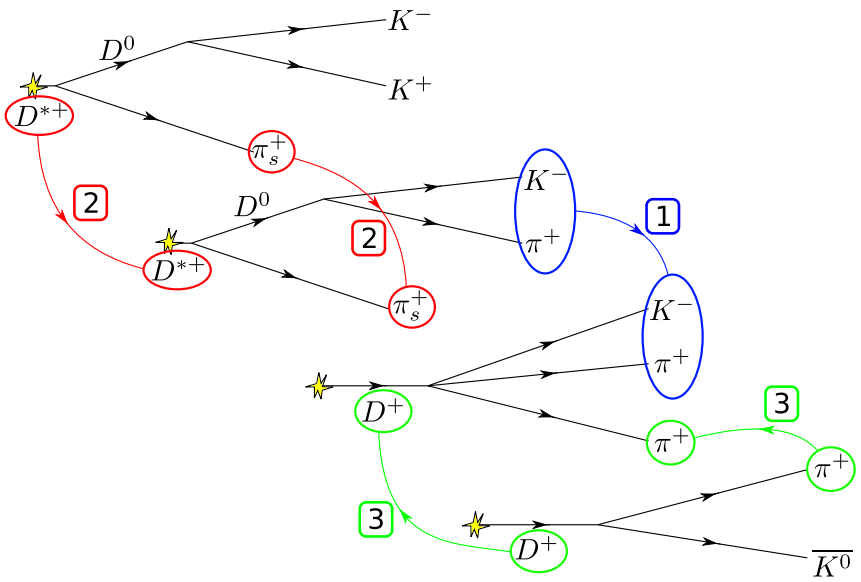

Figure 8.2: Weighting order "on $D^+ \to K^-\pi^+\pi^+$". Each channel is weighted into the direction of the $D^+ \to K^-\pi^+\pi^+$ channel. The numbers indicate the order and the arrows the direction of the individual weighting steps.

to have a smaller transverse momentum[2]. This is expected since one channel is a two body, the other a three body decay. Due to p_T requirements for the daughter particles in the stripping and the trigger selection, the charm mesons with more daughters tend to be measured with a higher p_T. There is one more reason for the huge discrepancy between the channels $D^+ \to \overline{K}^0\pi^+$ and $D^+ \to K^-\pi^+\pi^+$ when using the "natural" weighting order. When weighting the channel $D^+ \to K^-\pi^+\pi^+$ to the channel $D^0 \to K^-\pi^+$, the low p_T pion, cf chapter 5.2.2, is used to match the pion in $D^0 \to K^-\pi^+$ decays. This pion in the decay $D^0 \to K^-\pi^+$ therefore tends, to have a higher transverse momentum, and due to the weighting, the D^+ p_T distribution in the $D^+ \to K^-\pi^+\pi^+$ channel is shifted to higher values.

In order to avoid this small effective weighting factor for the $D^+ \to \overline{K}^0\pi^+$ channel, another weighting order is chosen. It is shown in figure 8.2. The first step is the weighting of the channel $D^0 \to K^-\pi^+$ to match the $D^+ \to K^-\pi^+\pi^+$ channel. Then, $D^0 \to K^-K^+$ decays are weighted on the already weighted $D^0 \to K^-\pi^+$ decays, and in a last step the $D^+ \to \overline{K}^0\pi^+$ channel is weighted to agree with the $D^+ \to K^-\pi^+\pi^+$ channel. This avoids the shift to higher D^+ p_T values in the channel $D^+ \to K^-\pi^+\pi^+$. It should be mentioned that the last step is independent of the other two steps and could also be performed before any other weighting. Since all channels are weighted into the direction of the $D^+ \to K^-\pi^+\pi^+$ channel, this weighting order is from now on called "on $K\pi\pi$". In addition to a change in the weighting order, after each weighting step, weights larger than 10 are not accepted and set to 10. This protects

[2]This can be seen in figure 8.5a.

the effective weight from the effects arising from a few very large weights.

As already mentioned in chapter 6.4.3, the low momentum pion in the decay $D^+ \to K^-\pi^+\pi^+$ and the pion in the decay $D^0 \to K^-\pi^+$ are required to have not triggered the event in the Hlt1 trigger. This is a natural way to select decays in which these pions have low transverse momentum. Then, also the D^+ candidates of these decays tend to have a smaller transverse momentum which reduces the differences between both D^+ decays. Since there are still some decays with a pion p_T larger than $1700\,\mathrm{MeV}/c$ fulfilling this Hlt1 requirement, cf chapter 6.3.2, an additional selection requirement on the transverse momentum is applied, see chapter 6.4.3.

When using the weighting order "on $K\pi\pi$", it is important to require the kaon in $D^+ \to K^-\pi^+\pi^+$ and $D^0 \to K^-\pi^+$ decays to have triggered the event in the Hlt1 trigger and, therefore, to satisfy certain p and p_T criteria. Otherwise, as explained in chapter 6.4.3, there would be a phase space region which is available for the $D^+ \to K^-\pi^+\pi^+$ decay but not for the $D^0 \to K^-\pi^+$ decay. Then, there would be no possibility to weight the latter to match the former.

8.2.2 Weighting steps and Results

Here, the individual weighting configurations for each step are presented. As an example, the results are shown for the data category 2011, magnet polarity down. The other categories show a similar behaviour.

Weighting of $D^0 \to K^-\pi^+$ candidates to $D^+ \to K^-\pi^+\pi^+$ candidates

These two channels should agree in the six-dimensional phase space spanned by the kinematic variables of the kaon and the pion. Since a six-dimensional weighting is not possible, in total four three-dimensional iterative weighting steps are performed[3]:

1. weighting in p_T,η,ϕ of the pion[4]
2. weighting in p_T,η,ϕ of the kaon
3. weighting again in p_T,η,ϕ of the pion
4. weighting again in p_T,η,ϕ of the kaon.

Each dimension of the individual weighting steps is divided into 20 bins. For the η and ϕ distributions, an equidistant binning into the range [2,5] and $[-\pi,\pi]$ is chosen. Since the p_T distribution of the kaon is strongly non-uniform with a long

[3] Several combinations of different weighting steps were tested in order to find the optimal configuration.

[4] Remember that the pion with the lower transverse momentum is used for the $D^+ \to K^-\pi^+\pi^+$ channel in this case.

tail containing only a few events, an adaptive binning was chosen. This is achieved by transforming p_T in the range [0:1] by the empirical function

$$g(p_T) = 2/\pi \arctan\left(5\frac{p_T - A}{B}\right). \tag{8.8}$$

The parameter A is given by the minimal p_T of 1700 MeV/c and $B = 10000\,\mathrm{MeV}/c$ is of the order of the maximal p_T. For the distribution of $g(p_T)$, a uniform binning in the range [0,1] is chosen. The figures 8.3a and 8.3b show the distributions of p_T, η and ϕ of the kaon and the pion before and after the weighting procedure. The agreement after weighting is significantly better than before but not perfect. There are four reasons for these deviations, which do also hold for the weighting of the other channels. First, the iterative weighting in three dimensions is not equivalent to a full six-dimensional weighting if the variables of the different particles are correlated. Furthermore, when plotting the distributions, a much finer binning is used compared to the binning used in the weighting steps. Thus, the distributions are not expected to agree in each bin but only when averaging over some of the bins in the figures. In addition, the truncation of high weights causes some differences. A further intrinsic problem is the weighting of empty bins to bins which are not empty. This can happen if there are large differences in the phase space distributions of the two channels.

The distribution of the weights is shown in figure 8.3c. There are weights higher than 10 because the weights of each of the four steps, which are truncated at 10, are multiplied to get the final weight of an decay candidate. As a result of the weighting procedure, an effective weighting factor of 0.22 has to be applied to the $D^0 \to K^-\pi^+$ channel. This means that the the statistical power is reduced by approximately 80%. A table with all yields before and after weighting is shown in chapter 8.2.2.

Weighting of $D^0 \to K^-K^+$ candidates to $D^0 \to K^-\pi^+$ candidates

The weighting of $D^0 \to K^-K^+$ candidates to the already weighted channel $D^0 \to K^-\pi^+$ is already described in chapter 8.1.2. Since the kinematic variables of the slow pion and the D^{*+} meson are strongly correlated, it is enough to perform only one weighting step in the D^{*+} variables:

1. weighting in p_T, η and ϕ of the D^{*+} meson.

Bins are chosen analogously to the weighting of $D^0 \to K^-\pi^+$ candidates to the channel $D^+ \to K^-\pi^+\pi^+$ and the transverse momentum of the D^{*+} meson is also transformed according to equation 8.8. The parameters A and B are chosen to be 2000 MeV/c and 20000 MeV/c. The figures 8.4a and 8.4b show the distributions of p_T, η and ϕ of the D^{*+} mesons and the slow pions before and after the weighting procedure. As expected, also the distributions of the slow pion agree well after the weighting, and no further weighting in variables of the slow pion is necessary. They even agree better since the effect of the binning is smeared out.

The distribution of the weights is shown in figure 8.4c. This time, there are no weights higher than 10 because only one weighting step is performed. An effective

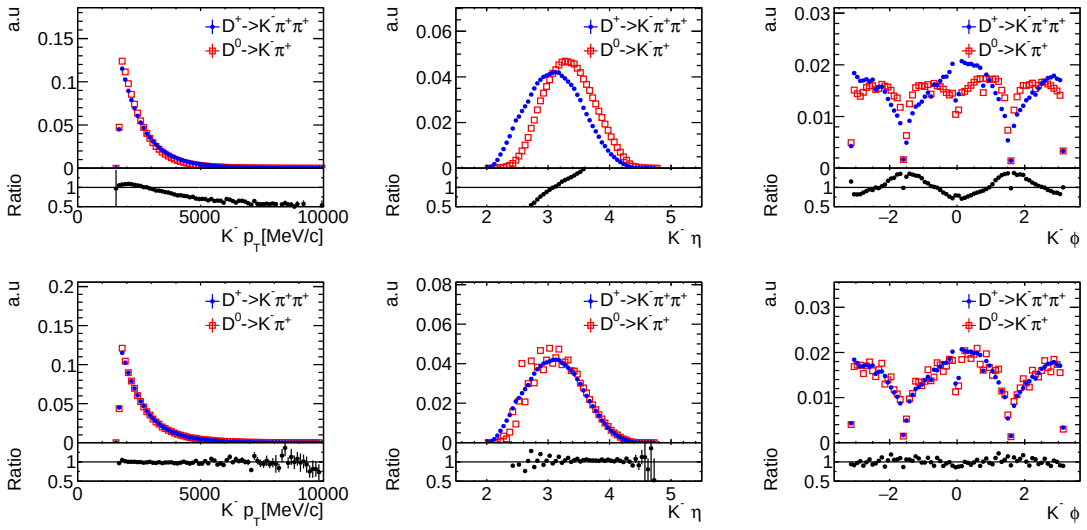

(a) K kinematics

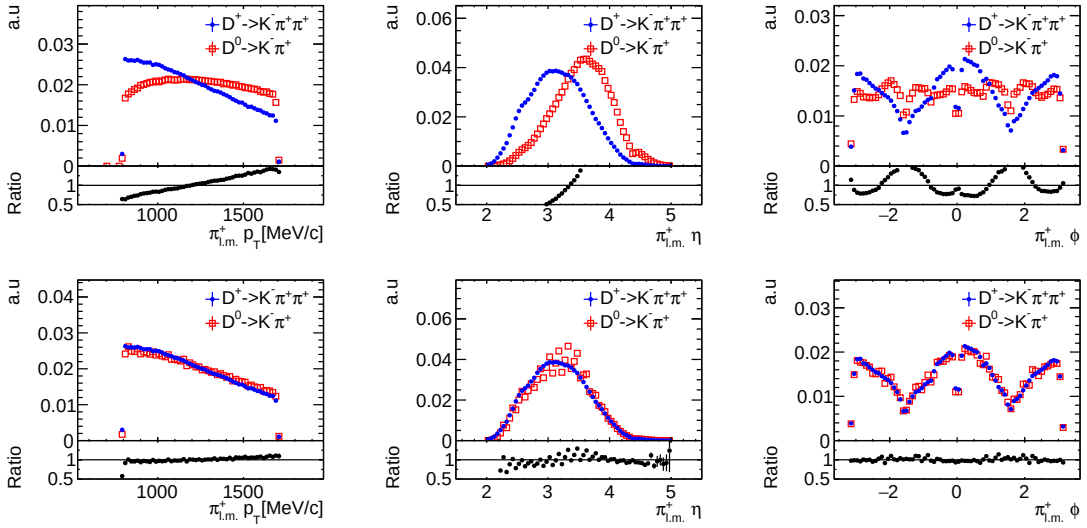

(b) π kinematics

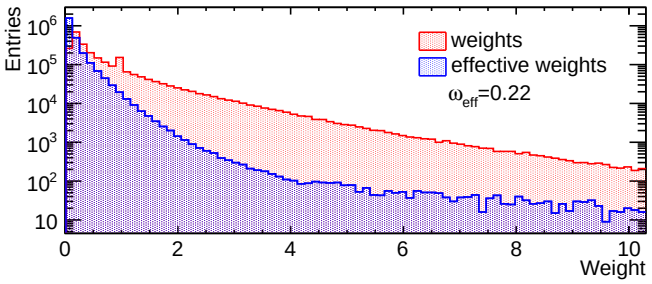

(c) Applied weights

Figure 8.3: Normalized kinematic distributions of (a) the kaon and (b) the pion in the weighting of $D^0 \to K^-\pi^+$ candidates to $D^+ \to K^-\pi^+\pi^+$ candidates. In the top row, they are shown before, and in the bottom row, after weighting. The weights applied are shown in (c). The effective weights are obtained by multiplying the normal weights with the effective weighting factor. The data sample taken in 2011 with magnet polarity down is used.

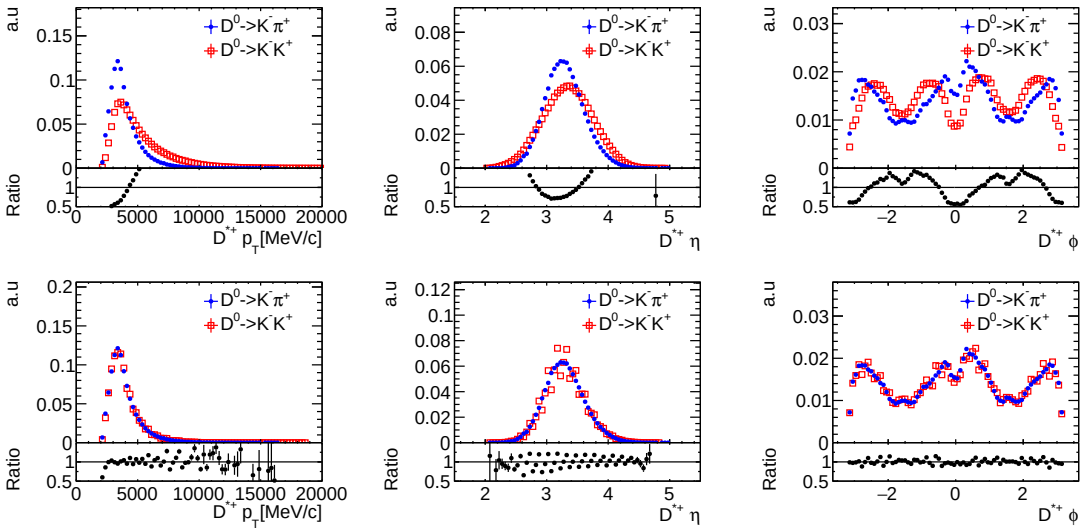

(a) D^* kinematics

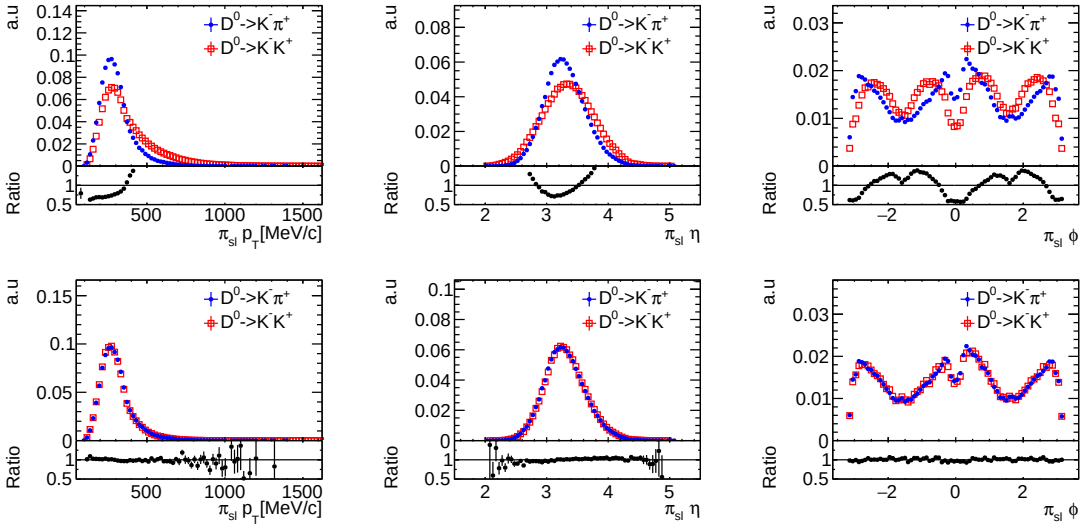

(b) π_{sl} kinematics

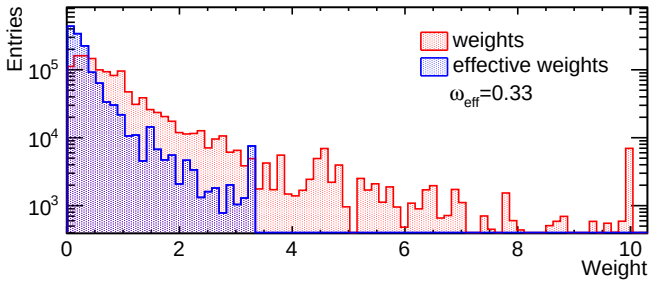

(c) Applied weights

Figure 8.4: Normalized kinematic distributions of (a) the D^{*+} meson and (b) the slow pion in the weighting of the channel $D^0 \to K^-K^+$ to the channel $D^0 \to K^-\pi^+$. In the top row, they are shown before, and in the bottom row, after weighting. The weights applied are shown in (c). The effective weights are obtained by multiplying the normal weights with the effective weighting factor. The data sample taken in 2011 with magnet polarity down is used.

weighting factor of 0.33 has to be applied to the $D^0 \to K^-\pi^+$ channel. This means that the the statistical power of this channel is also reduced by a relatively high amount. A table with all yields before and after weighting is shown at the end of this chapter.

Weighting of $D^+ \to \overline{K}^0\pi^+$ candidates to $D^+ \to K^-\pi^+\pi^+$ candidates

Similarly to the weighting of the $D^0 \to K^-\pi^+$ channel to the $D^+ \to K^-\pi^+\pi^+$ channel, several weighting steps have to be performed to achieve an acceptable agreement between the two channels. Since the production asymmetry of the D^+ meson does not depend on ϕ, cf. chapter 5.1.1, a weighting in this variable is not necessary. The following steps lead to good results[5]

1. weighting in p_T,η of the D^+ meson and in p_T of the pion[6]
2. weighting in p_T,η of the pion and in p_T of the D^+ meson
3. weighting in p_T,ϕ of the pion and in p_T of the D^+ meson.

Here, weighting steps with variables from both particles help to get a simultaneous agreement. The binning is chosen analogously to the weighting of $D^0 \to K^-\pi^+$ candidates to the channel $D^+ \to K^-\pi^+\pi^+$, and the transverse momenta of the D^+ mesons and the pions are also transformed according to equation 8.8. For the pion transverse momentum, $A = 800\,\mathrm{MeV}/c$ and $B = 10000\,\mathrm{MeV}/c$ is chosen. The D^+ transverse momentum, is transformed using exactly the same parameters as for the D^{*+} meson in the second weighting step. The figures 8.5a and 8.5b show the distributions of p_T, η and ϕ of the D^+ meson and the pion before and after the weighting procedure. The overall agreement is good after the weighting. Even in the distribution of ϕ of the D^+ meson, the differences are small which was a priori not required since the production asymmetry does not depend on the azimuthal angle of the D^+ meson. As already explained in 8.2.1, the D^+ p_T distributions show large discrepancies before the weighting. After weighting these distributions are in good agreement.

The distribution of the weights is shown in figure 8.5c. Since there are again multiple weighting steps used, the weights are not limited to 10 but they do not exceed this value much[7]. An effective weighting factor of 0.30 has to be applied to the $D^0 \to K^-\pi^+$ channel. This means that the statistical power of this channel is reduced by 70%. This is the result of the differences in the D^+ p_T distributions. A table with all yields before and after weighting is shown at the end of this chapter.

[5]Several combinations of different weighting steps were tested in order to find the optimal configuration.

[6]Remember that the pion with the higher transverse momentum is used for the $D^+ \to K^-\pi^+\pi^+$ channel in this case.

[7]By the effective weighting factor of 0.3 a weight of 10 corresponds to an effective weight of 3.

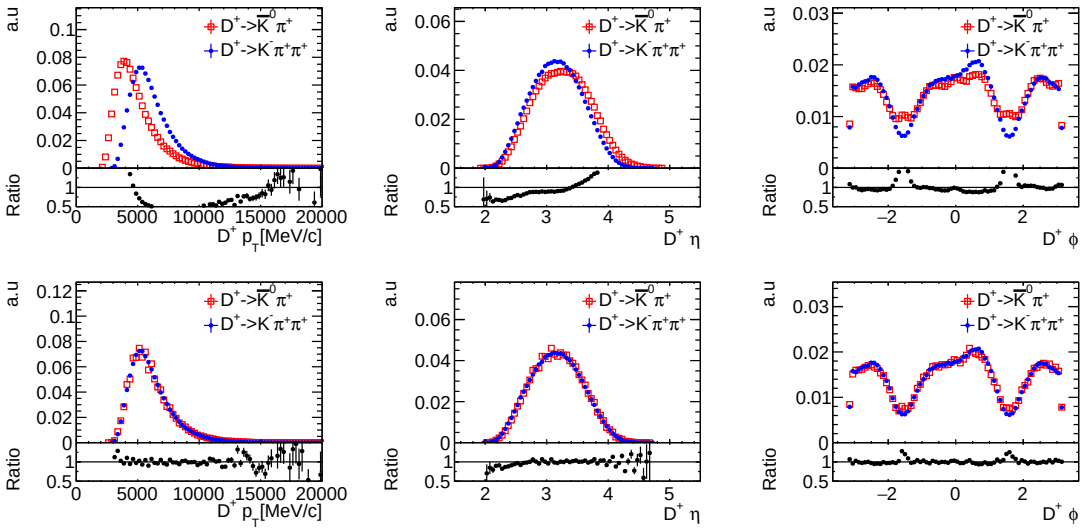

(a) D kinematics

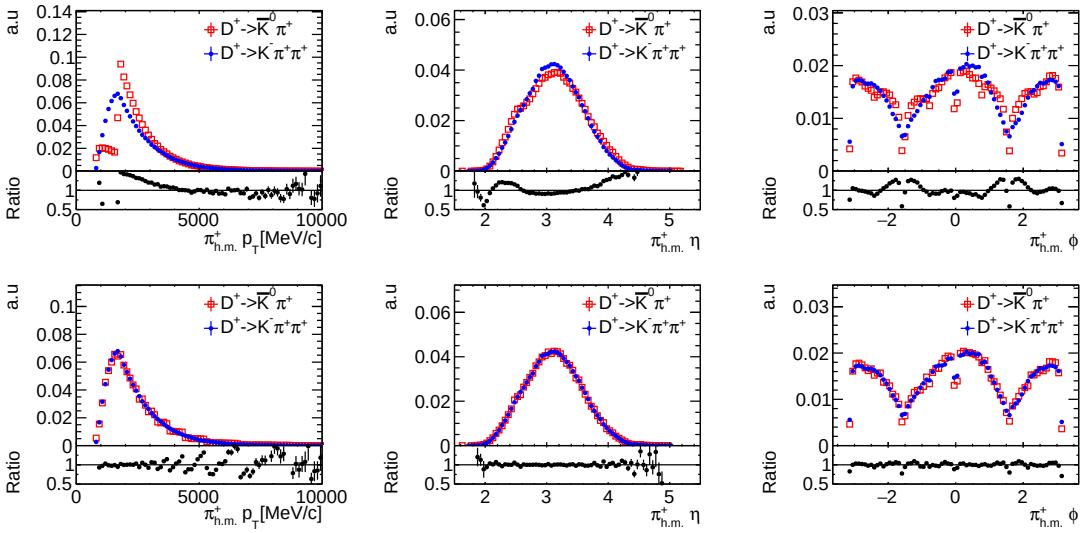

(b) π kinematics

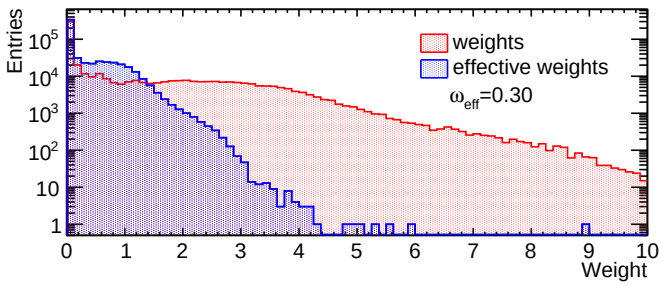

(c) Applied weights

Figure 8.5: Normalized kinematic distributions of (a) the D^+ meson and (b) the pion in the weighting of $D^+ \to \overline{K}^0\pi^+$ candidates to $D^+ \to K^-\pi^+\pi^+$ candidates. In the top row, they are shown before, and in the bottom row, after weighting. The weights applied are shown in (c). The effective weights are obtained by multiplying the normal weights with the effective weighting factor. The data sample taken in 2011 with magnet polarity down is used.

Summary

Table 8.1 shows the yields for each channel before and after the weighting. The statistical loss due to the weighting is of the same order for all channels. With a reduction of about 78−79%, the channel $D^0 \to K^-\pi^+$ is most affected. However, due to its large branching ratio, it is not the statistically limiting channel. The channel $D^+ \to \overline{K}^0\pi^+$ has by far the smallest statistics, before and after the weighting, and contributes the dominant statistical uncertainty.

The effective weighting factors for magnet polarity up and down differ at most by 0.02, but between 2011 and 2012 changes up to 0.05 are present. Since the kinematic distributions can depend on the beam energy and on requirements in the reconstruction, this is not unexpected.

For all steps, the shown diagrams indicate that there are still some residual differences after weighting. Therefore, further systematic studies of the weighting procedure are necessary. There are two ways to estimate how the chosen weighting strategy affects the final measurement. The first is to perform the analysis independently by varying the weighting procedure. The second is to model the dependencies of the individual detection and production asymmetries, and simulate how the chosen weighting scheme performs. Both possibilities are shown in chapter 11.2.

Table 8.1: Signal yields before and after the weighting for each of the weighted channels. The effective weighting factor is approximately given by their ratio.

(a) $D^{*+} \to D^0(\to K^-\pi^+)\pi^+_{sl}$

sample	**original yield**	**yield after weighting**	ω_{eff}
2011 up	1.38 M	265 k	0.22
2011 down	1.97 M	384 k	0.22
2012 up	3.75 M	662 k	0.21
2012 down	3.92 M	741 k	0.22

(b) $D^{*+} \to D^0(\to K^-K^+)\pi^+_{sl}$

sample	**original yield**	**yield after weighting**	ω_{eff}
2011 up	643 k	212 k	0.33
2011 down	918 k	300 k	0.33
2012 up	1.82 M	542 k	0.30
2012 down	1.87 M	561 k	0.31

(c) $D^+ \to \overline{K}^0\pi^+$

sample	**original yield**	**yield after weighting**	ω_{eff}
2011 up	365 k	108 k	0.29
2011 down	525 k	159 k	0.30
2012 up	1.41 M	363 k	0.26
2012 down	1.44 M	367 k	0.25

Chapter 9

Neutral kaon asymmetry

In chapter 5.2, the asymmetry induced by the neutral kaon is identified as the residual asymmetry[1] after combining the measured raw asymmetries. In this chapter, the different components of this asymmetry are discussed and calculated. This is done in full analogy to the previous analysis presented in [5], and is, therefore, not presented in full detail here.

9.1 Motivation and formalism

In the decay $D^+ \to \overline{K}^0\pi^+$, the neutral kaon is produced as the flavour eigenstate $\overline{K}^0$, or as K^0 for the decay of a D^- meson. These flavour eigenstates do not coincide with the mass eigenstates which are instead given by the K_s^0 and the K_L^0 mesons. As mentioned earlier, cf chapter 6.1, the neutral kaons are detected and reconstructed using the decay $K_s^0 \to \pi^-\pi^+$. Since the K_s^0 meson is not a CP eigenstate [40], this induces a detection asymmetry of the produced neutral kaons. In addition, the asymmetric interaction of kaons with material of the detector, cf. chapter 2.4, has to be taken into account. This causes an asymmetry even in the absence of CP violation due to the fact that the K_s^0 meson is a superposition of both flavour eigenstates. The two effects of asymmetric material interaction and CP violation can not be calculated separately since they interfere due to coherent forward scattering.

In analogy to chapter 2.3, the evolution in time of the neutral kaons is governed by an effective Schroedinger equation:

$$i\frac{d}{dt}\begin{pmatrix}|K^0(t)\rangle\\|\overline{K}^0(t)\rangle\end{pmatrix} = \left(\boldsymbol{M} - \frac{i}{2}\boldsymbol{\Gamma}\right)\begin{pmatrix}|K^0(t)\rangle\\|\overline{K}^0(t)\rangle\end{pmatrix}. \tag{9.1}$$

The eigenstates of the Hamiltonian are given by the mass eigenstates K_s^0 and K_L^0 which are connected to the flavour eigenstates by:

$$\begin{aligned}|K^0\rangle &= \frac{\sqrt{1+|\epsilon|^2}}{2}\frac{1}{1+\epsilon}\left(|K_L^0\rangle + |K_s^0\rangle\right),\\ |\overline{K}^0\rangle &= \frac{\sqrt{1+|\epsilon|^2}}{2}\frac{1}{1-\epsilon}\left(|K_L^0\rangle - |K_s^0\rangle\right).\end{aligned} \tag{9.2}$$

[1] Beside a possible CP asymmetry in the decay $D^0 \to K^-K^+$.

Here, ϵ parametrizes the CP violation in mixing and is measured to be: $|\epsilon| = 2.228 \pm 0.011) \times 10^{-3}$ [11]. For $\epsilon \neq 0$, the mass eigenstates differ from the CP eigenstates K_1^0 and K_2^0 and can be expressed as:

$$\begin{aligned} |K_L^0\rangle &= \frac{1}{\sqrt{1+|\epsilon|^2}} \left(|K_2^0\rangle + \epsilon\,|K_1^0\rangle\right), \\ |K_s^0\rangle &= \frac{1}{\sqrt{1+|\epsilon|^2}} \left(|K_1^0\rangle + \epsilon\,|K_2^0\rangle\right). \end{aligned} \tag{9.3}$$

Equation 9.1 is only valid in vacuum. The interaction of the flavour eigenstates of the neutral kaon with matter is described by another differential equation:

$$i\frac{d}{dt}\begin{pmatrix}|K^0(t)\rangle \\ |\overline{K}^0(t)\rangle\end{pmatrix} = \boldsymbol{\chi}\begin{pmatrix}|K^0(t)\rangle \\ |\overline{K}^0(t)\rangle\end{pmatrix} = \begin{pmatrix}\chi & 0 \\ 0 & \overline{\chi}\end{pmatrix}\begin{pmatrix}|K^0(t)\rangle \\ |\overline{K}^0(t)\rangle\end{pmatrix}, \tag{9.4}$$

where χ and $\overline{\chi}$ describe the interaction of K^0 and $\overline{K}^0$ mesons with matter. This interaction has to be taken into account when describing the time evolution of neutral kaons in matter. By combining equation 9.4 with the effective Schroedinger equation 9.1, the time evolution of neutral kaons in the presence of matter is governed by:

$$i\frac{d}{dt}\begin{pmatrix}|K^0(t)\rangle \\ |\overline{K}^0(t)\rangle\end{pmatrix} = \left(\boldsymbol{M} - \frac{i}{2}\boldsymbol{\Gamma} + \boldsymbol{\chi}\right)\begin{pmatrix}|K^0(t)\rangle \\ |\overline{K}^0(t)\rangle\end{pmatrix}. \tag{9.5}$$

Since the states K_L^0 and K_s^0 are no longer the eigenstates of the effective Hamiltonian, transitions between these states are possible when travelling through matter. This effect is called regeneration.

By solving equation 9.5 for the initial states K^0 and $\overline{K}^0$, given by equation 9.2, and combining the result with the decomposition in CP eigenstates, as shown in equation 9.3, one can calculate the time dependent asymmetry of the decay into two pions, defined as:

$$a(t) = \frac{\Gamma(\overline{K}^0_{t=0} \to \pi^-\pi^+)(t) - \Gamma(K^0_{t=0} \to \pi^-\pi^+)(t)}{\Gamma(\overline{K}^0_{t=0} \to \pi^-\pi^+)(t) + \Gamma(K^0_{t=0} \to \pi^-\pi^+)(t)}. \tag{9.6}$$

Figure 9.1a shows the calculated time dependent asymmetry for kaons with a momentum of $30\,\mathrm{GeV}/c$ and a homogeneous material density corresponding to 2% of that of aluminium. For small decay times, the effects of material interaction and CP violation are of the same order. Only for neutral kaons, living longer than 2.5 K_s^0 decay times τ_s, the interference between those two is relevant. The final asymmetry contributing to the measured raw asymmetry, is given by the time integrated neutral kaon asymmetry A:

$$A = \frac{\int_0^\infty \epsilon(t)\left[\Gamma(\overline{K}^0_{t=0} \to \pi^-\pi^+)(t) - \Gamma(K^0_{t=0} \to \pi^-\pi^+)(t)\right]\mathrm{d}t}{\int_0^\infty \epsilon(t)\left[\Gamma(\overline{K}^0_{t=0} \to \pi^-\pi^+)(t) + \Gamma(K^0_{t=0} \to \pi^-\pi^+)(t)\right]\mathrm{d}t}. \tag{9.7}$$

Here, $\epsilon(t)$ describes the time dependent acceptance of neutral kaons. Assuming a flat acceptance, the time integrated asymmetry is shown in figure 9.1b. Since kaons

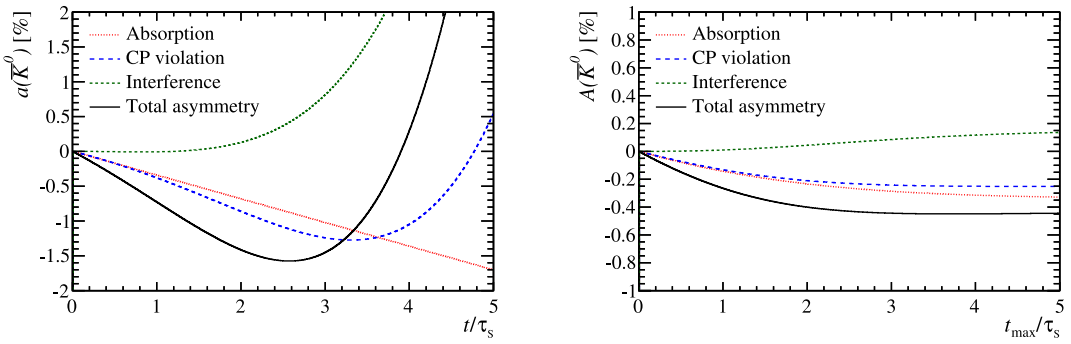

(a) Time-dependent asymmetry **(b)** Time-integrated asymmetry

Figure 9.1: Time dependent (a) and time integrated (b) asymmetry of the neutral kaon. The individual components and the sum are shown. A constant material distribution with 2% of the density of aluminium and kaons with a momentum of 30 GeV/c are assumed. The time is shown in units of the K_s^0 lifetime τ_s. Figure taken from Ref. [5].

used for this analysis are reconstructed by two long tracks, cf. chapter 3.2.1, they are required to decay already inside the VELO. Therefore, only kaons with decay times between 0 and $0.5\tau_s$ are selected [5]. Thus, the expected asymmetry is of order 0.1%.

In order to obtain the asymmetry for the recorded neutral kaons, for each selected candidate j, the asymmetry a_j is iteratively calculated using a simulation of the detector material. For more details, see Ref. [5]. The final asymmetry present in a sample with N candidates is given by:

$$A_D(\overline{K}^0) = \frac{1}{N}\sum_{j=1}^{N} a_j.$$

For each of the four data categories, $A_D(\overline{K}^0)$ is calculated in this way. In order to subtract the background contribution, the individual asymmetries of the candidates are multiplied by weights obtained with the ${}_sPlot$ technique. Analogously, the weights obtained by the kinematic weighting, cf. chapter 8, are applied in order to get the neutral kaon asymmetries for the weighted samples.

9.2 Calculated asymmetries

Table 9.1 shows the calculated neutral kaon asymmetries for each of the four data categories. A 25% systematic uncertainty on the values is quoted. It arises from uncertainties on the K_s^0 model and is taken from Ref. [5]. As expected, the absolute asymmetries are smaller than 0.1%. The individual values for the different categories hardly differ between the magnet polarities of one data taking period,

Table 9.1: Calculated $\overline{K}^0$ asymmetries for the different data categories. Values for the weighted and not weighted samples are given. The quoted uncertainties arise from a relative systematic uncertainty of 25%.

Category	$\boldsymbol{A_D(\overline{K}^0)}$**[%] not weighted**	$\boldsymbol{A_D(\overline{K}^0)}$**[%] weighted**
2011 up	-0.070 ± 0.018	-0.041 ± 0.010
2011 down	-0.071 ± 0.018	-0.040 ± 0.010
2012 up	-0.075 ± 0.019	-0.045 ± 0.011
2012 down	-0.075 ± 0.019	-0.045 ± 0.011

but between 2011 and 2012 data, clear differences are visible. This is due to the different reconstruction and trigger requirements. The weighted samples show a much smaller neutral kaon asymmetry. This can be explained by the shift to higher p_T values visible for the D^+ meson, cf. figure 8.5a. The neutral kaon kinematics are correlated with the charm meson kinematics, and therefore, the neutral kaons p_T spectrum is shifted to higher values. Particles with high p_T values tend to spend less time inside the VELO. Therefore, the kaons in the weighted samples are expected to show smaller decay times which causes a lower neutral kaon asymmetry, cf. figure 9.1a.

Chapter 10

Final asymmetries

In this chapter, the extraction of raw asymmetries of the weighted samples is presented and the obtained values are compared to the ones of the not weighted samples. The asymmetries are then combined with the neutral kaon asymmetry to get a value for the measured CP asymmetry in the decay $D^0 \to K^-K^+$.

10.1 Extraction of $A_{CP}(K^-K^+)$

The raw asymmetries of the weighted samples are extracted analogously to the procedure presented in chapter 7. Figure 10.1 to 10.4 show the mass and asymmetry plots of the final raw asymmetry extraction. Tables containing the final values of the fit parameters can be found in appendix B. As for the not weighted distributions, especially for the D^0 decays the χ^2/ndf values of the mass fits tend to be too large. In contrast to that, the asymmetries, are modelled more appropriate. Anyhow the influence of the fit model is studied in chapter 11.1.

In table 10.1, the extracted raw asymmetries are shown and combined according to chapter 5.2 with the calculated asymmetry induced by the neutral kaon, cf chapter 9, in order to obtain $A_{CP}(K^-K^+)$. As discussed in chapter 5.3, the asymmetries obtained with the two magnet polarities within one year are arithmetically averaged. The weighted mean of both data taking periods is then the final result. This also means, that the final value is neither the arithmetic nor the weighted mean of the values quoted as the mean of both magnet polarities in 2011 and 2012.

The change of the individual raw asymmetries due to the weighting is discussed in the next section. As expected, the measured raw asymmetry of the channel $D^+ \to \overline{K}^0\pi^+$ contributes most to the final statistic uncertainty. However, also the two D^0 decays contribute at a comparable level. Only the raw asymmetries of the channel $D^+ \to K^-\pi^+\pi^+$ show much smaller statistic uncertainties since this channel is not affected by the weighting procedure. Besides the value obtained using data from 2011 with magnet polarity down, all distinct measurements of $A_{CP}(K^-K^+)$ for the four categories are consistent as well with the hypthesis of no CP violation as with the final mean value obtained by all four categories. Also, the value for the category 2011 magnet polarity up deviates not significantly. Especially, the fact that there are no significant differences between magnet polarity up and down

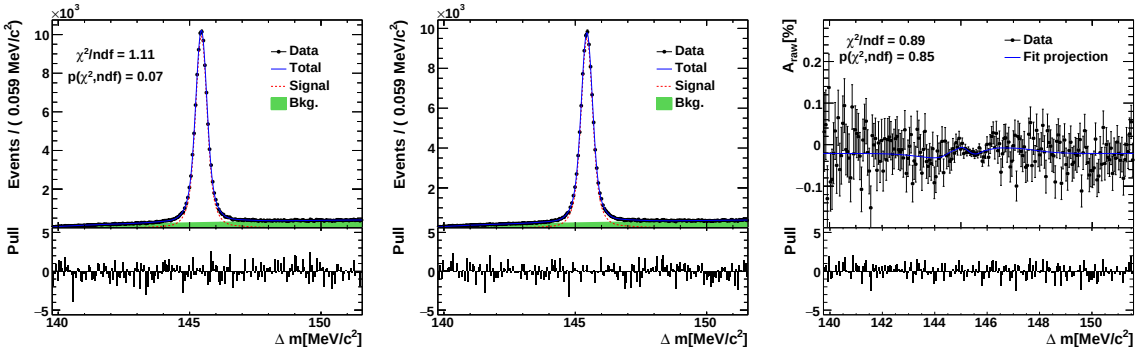

(a) 2011 magnet polarity up

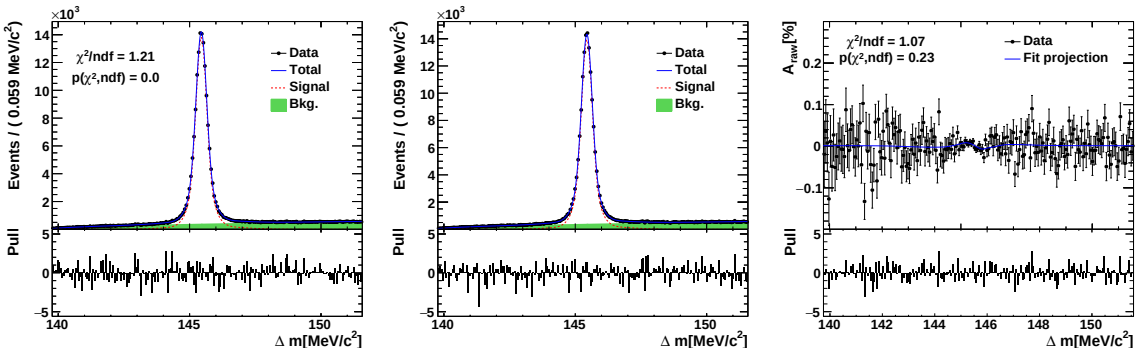

(b) 2011 magnet polarity down

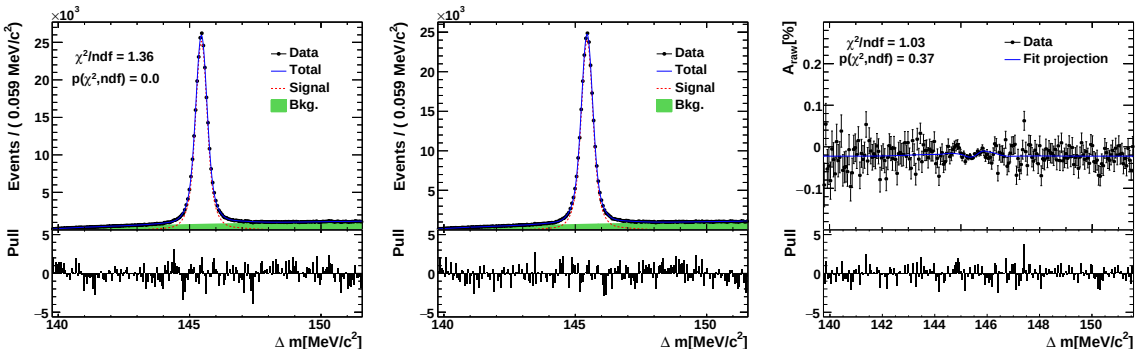

(c) 2012 magnet polarity up

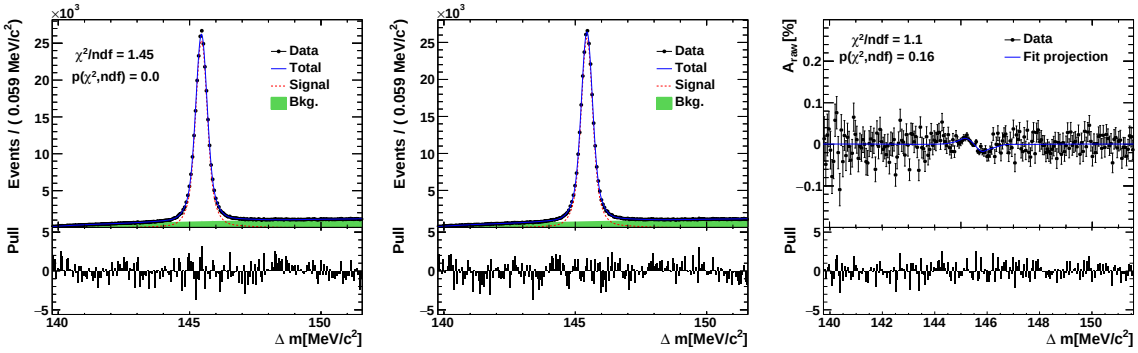

(d) 2012 magnet polarity down

Figure 10.1: Results of the fit to the mass difference between the D^{*+} and D^0 candidate for the channel $D^0 \to K^-K^+$. The left row shows the positively tagged decay candidates, the middle row the negatively tagged candidates, and the right row the asymmetry for each of the four data categories.

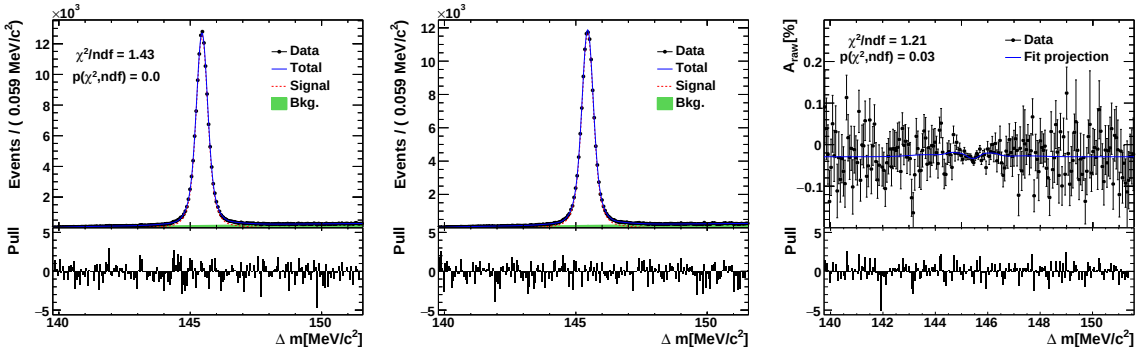

(a) 2011 magnet polarity up

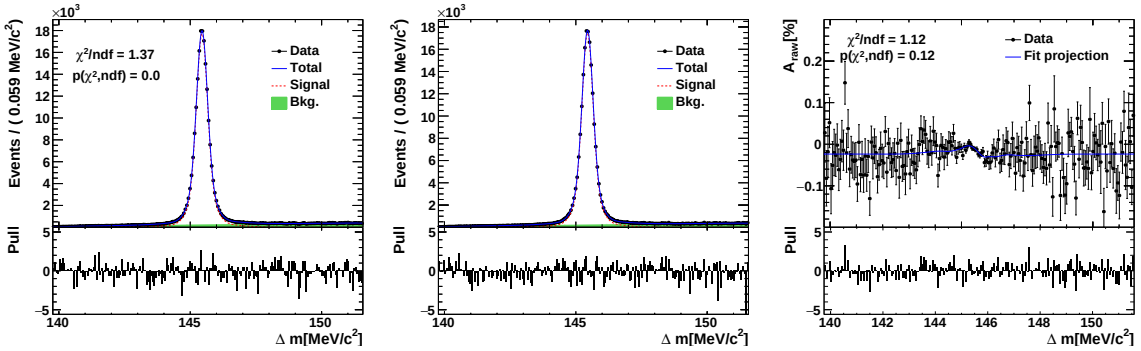

(b) 2011 magnet polarity down

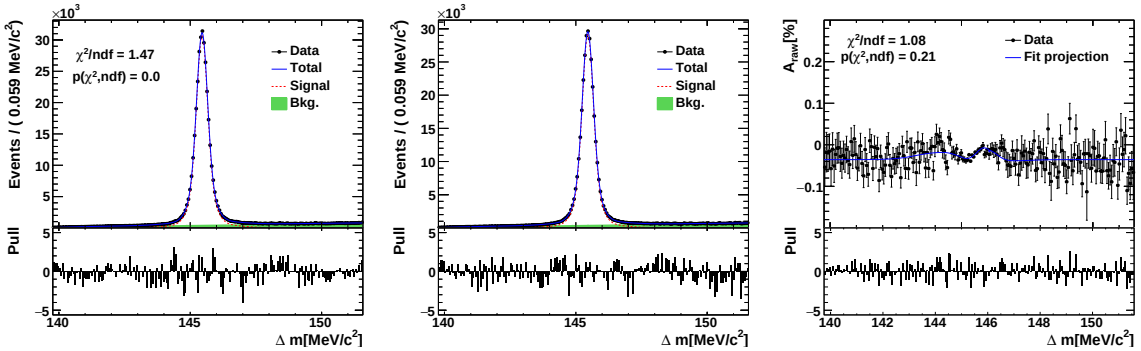

(c) 2012 magnet polarity up

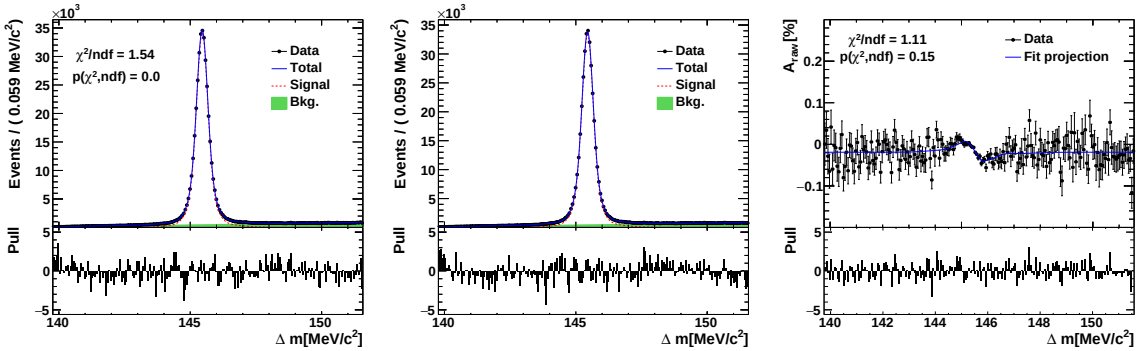

(d) 2012 magnet polarity down

Figure 10.2: Results of the fit to the mass difference between the D^{*+} and D^0 candidate for the channel $D^0 \to K^-\pi^+$. The left row shows the positively tagged decay candidates, the middle row the negatively tagged candidates, and the right row the asymmetry for each of the four data categories.

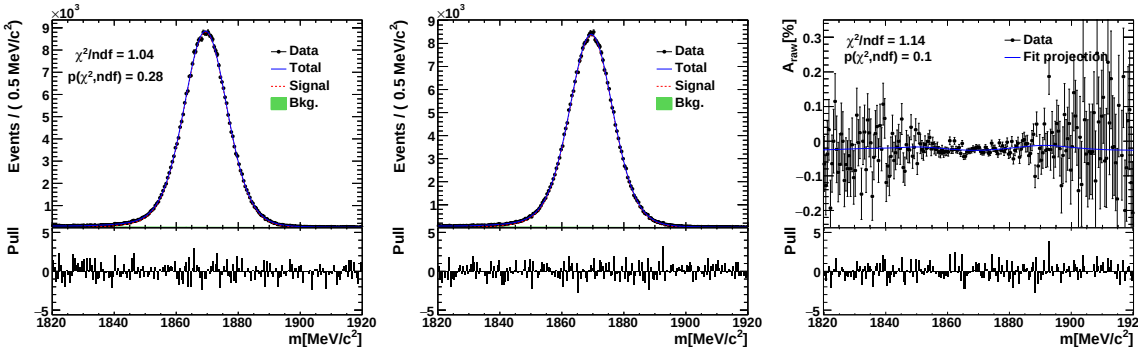

(a) 2011 magnet polarity up

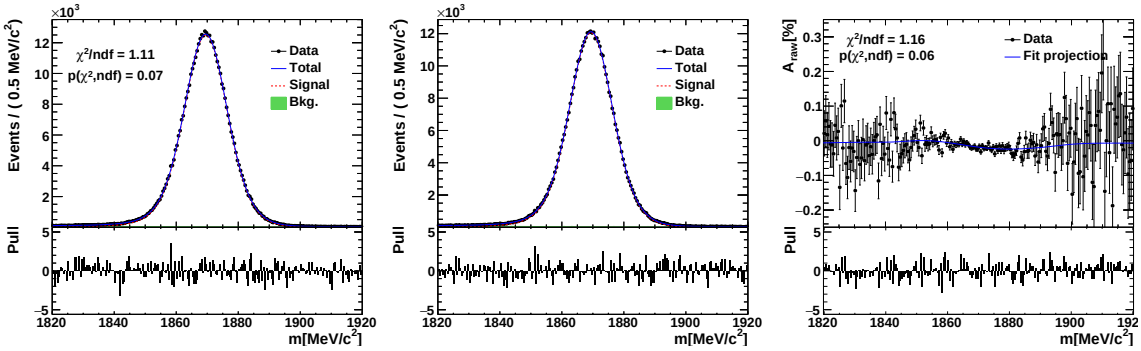

(b) 2011 magnet polarity down

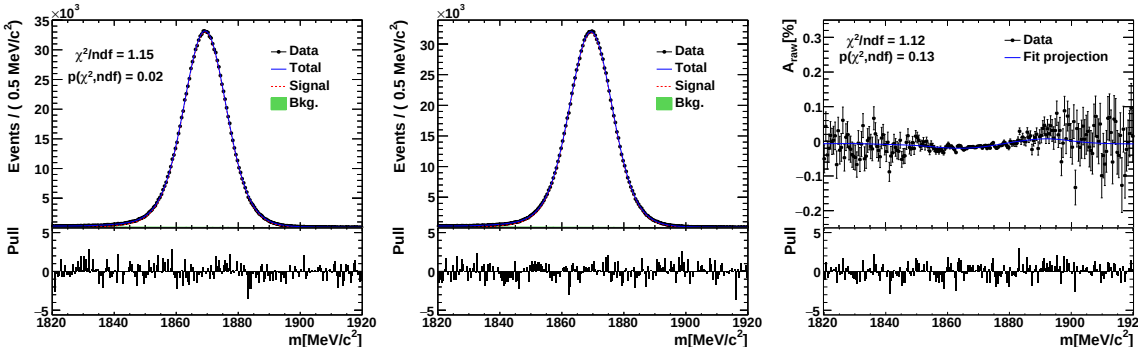

(c) 2012 magnet polarity up

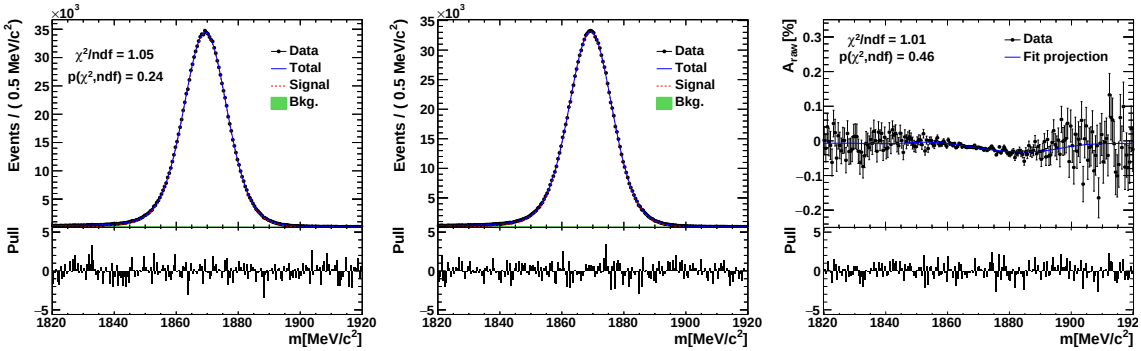

(d) 2012 magnet polarity down

Figure 10.3: Results of the fit to the mass difference between the D^{*+} and D^0 candidate for the channel $D^+ \to K^-\pi^+\pi^+$. The left row shows the positively tagged decay candidates, the middle row the negatively tagged candidates, and the right row the asymmetry for each of the four data categories.

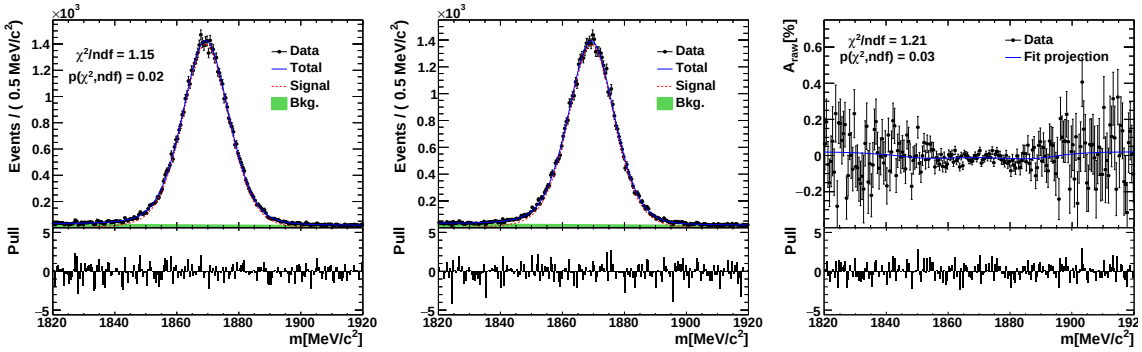

(a) 2011 magnet polarity up

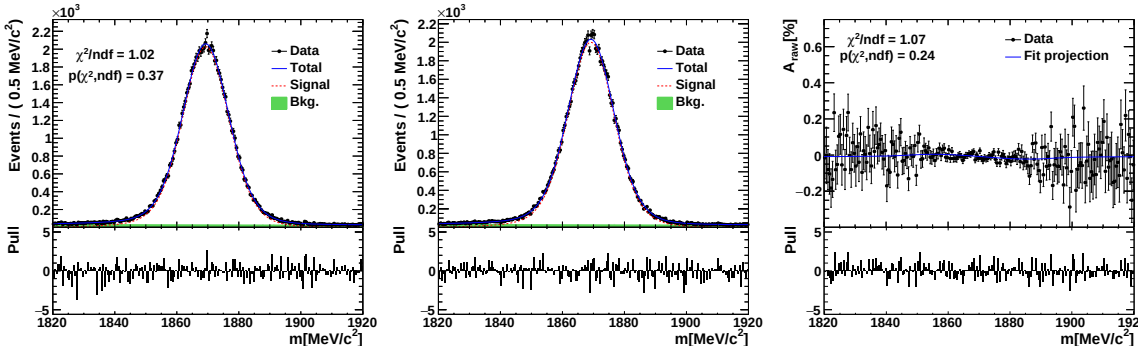

(b) 2011 magnet polarity down

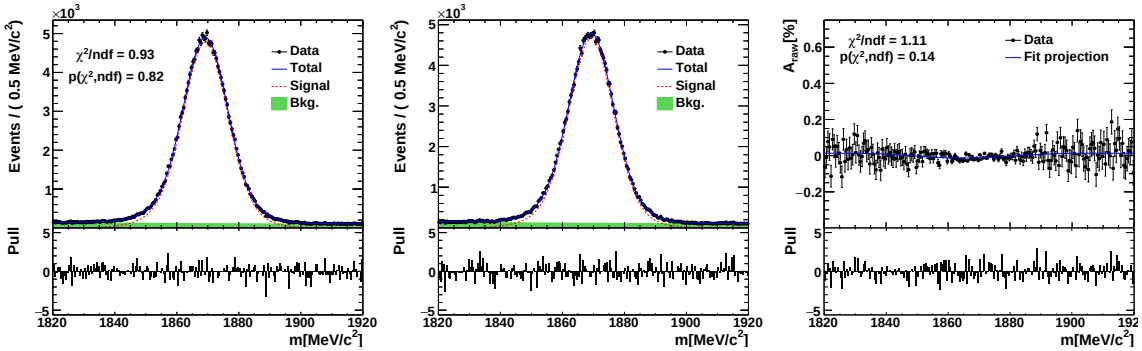

(c) 2012 magnet polarity up

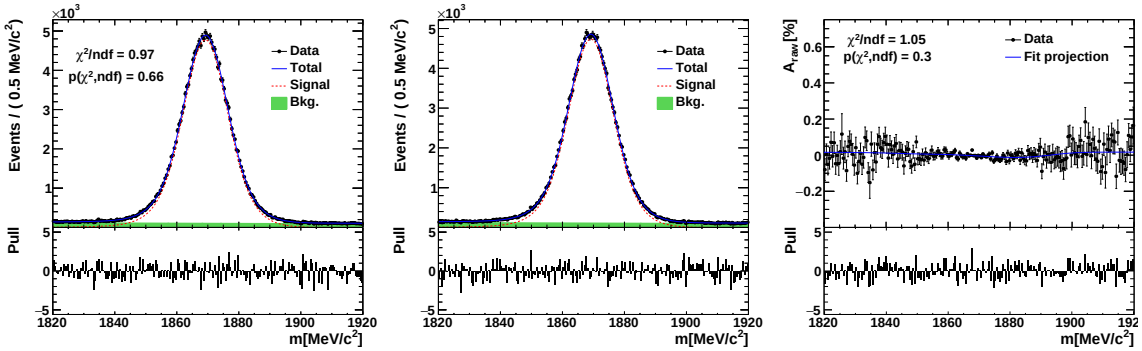

(d) 2012 magnet polarity down

Figure 10.4: Results of the fit to the mass difference between the D^{*+} and D^0 candidate for the channel $D^+ \to \overline{K^0}\pi^+$. The left row shows the positively tagged decay candidates, the middle row the negatively tagged candidates, and the right row the asymmetry for each of the four data categories.

Table 10.1: Final measured asymmetries. Weighted samples are used if present. The combination of the different datasets is analogous to chapter 5.3 and $A_{CP}(K^-K^+)$ is calculated according to chapter 5.2.2.

2011	**up**	**down**	**mean**
$A_{raw}(D^0 \to K^+K^-)$	-1.60 ± 0.24	0.23 ± 0.20	-0.68 ± 0.15
$A_{raw}(D^0 \to K^-\pi^+)$	-2.78 ± 0.20	-1.28 ± 0.17	-2.03 ± 0.13
$A_{raw}(D^+ \to K^-\pi^+\pi^+)$	-2.35 ± 0.13	-1.58 ± 0.11	-1.965 ± 0.084
$A_{raw}(D^+ \to \overline{K}^0\pi^+)$	-1.53 ± 0.33	-0.74 ± 0.27	-1.14 ± 0.21
$A_D(\overline{K}^0)$	-0.041	-0.040	-0.041
$A_{CP}(D^0 \to K^-K^+)$	0.32 ± 0.47	0.63 ± 0.39	0.47 ± 0.31
2012	**up**	**down**	**mean**
$A_{raw}(D^0 \to K^+K^-)$	-1.92 ± 0.15	0.09 ± 0.15	-0.92 ± 0.10
$A_{raw}(D^0 \to K^-\pi^+)$	-2.24 ± 0.13	-1.38 ± 0.12	-1.809 ± 0.089
$A_{raw}(D^+ \to K^-\pi^+\pi^+)$	-1.470 ± 0.067	-1.916 ± 0.065	-1.693 ± 0.047
$A_{raw}(D^+ \to \overline{K}^0\pi^+)$	-1.05 ± 0.18	-0.48 ± 0.18	-0.77 ± 0.13
$A_D(\overline{K}^0)$	-0.045	-0.045	-0.045
$A_{CP}(D^0 \to K^-K^+)$	-0.14 ± 0.28	-0.01 ± 0.27	-0.08 ± 0.19
2011 + 2012	**up**	**down**	**mean**
$A_{raw}(D^0 \to K^+K^-)$	-1.83 ± 0.13	0.14 ± 0.12	-0.84 ± 0.10
$A_{raw}(D^0 \to K^-\pi^+)$	-2.39 ± 0.11	-1.346 ± 0.099	-1.877 ± 0.089
$A_{raw}(D^+ \to K^-\pi^+\pi^+)$	-1.655 ± 0.059	-1.827 ± 0.056	-1.757 ± 0.047
$A_{raw}(D^+ \to \overline{K}^0\pi^+)$	-1.17 ± 0.16	-0.56 ± 0.15	-0.86 ± 0.13
$A_D(\overline{K}^0)$	-0.043	-0.043	-0.043
$A_{CP}(D^0 \to K^-K^+)$	-0.02 ± 0.24	0.19 ± 0.22	0.08 ± 0.16

demonstrates the cancellation of nuisance asymmetries within one data category.

The final value for the time integrated CP asymmetry in the decay $D^0 \to K^-K^+$ is:

$$A_{CP}(K^-K^+) = (0.08 \pm 0.16)\%. \tag{10.1}$$

So far, only the statistical uncertainty is given. A study of systematic uncertainties follows in chapter 11.

10.2 Changes due to weighting

In order to study the effect of the weighting procedure, the changes of the measured raw asymmetries, the asymmetry induced by the neutral kaon and the final CP asymmetry are listed in table 10.2. Since the weights cause a reduction of the yields, the observed shifts can also be to some extend of statistical origin. The quadratic

Table 10.2: Occurring asymmetries affected by the weighting procedure. The average of all four data categories is used. In addition, the shift due to the weighting Δ and the quadratic difference of the uncertainties are shown.

Quantity	**Not weighted**	**Weighted**	$\boldsymbol{\Delta}$**[%]**	$\boldsymbol{\sqrt{\sigma_w^2 - \sigma_{n.w.}^2}}$
$A_{raw}(D^0 \to K^+K^-)$[%]	-0.973 ± 0.047	-0.844 ± 0.086	0.13	0.072
$A_{raw}(D^0 \to K^-\pi^+)$[%]	-2.016 ± 0.032	-1.877 ± 0.074	0.14	0.067
$A_{raw}(D^+ \to \overline{K}^0\pi^+)$[%]	-0.804 ± 0.056	-0.86 ± 0.11	-0.061	0.094
$A_D(\overline{K}^0)$[%]	-0.073	-0.043	0.030	-
$A_{CP}(K^-K^+)$[%]	0.000 ± 0.090	0.08 ± 0.16	0.078	0.14

difference of the uncertainties $\sigma_w/\sigma_{n.w.}$ of weighted and not weighted asymmetries

$$\sqrt{\sigma_w^2 - \sigma_{n.w.}^2}, \tag{10.2}$$

is a good estimator of the possible statistical shift due to the weighting [5].

The channel $D^0 \to K^-\pi^+$ shows the largest shift which is compatible with a statistical fluctuation only within approximately $2\,\sigma$. Also the other D^0 channel shows a shift which exceeds the statistical fluctuation nearly by a factor of 2. In contrast to these two, the channel with the neutral kaon is not shifted significantly more than expected due to statistical fluctuation. Since the yield of this channel is severely reduced by the weighting, and since it is already small compared to the other channels before the weighting, the expected statistical fluctuation is large and hides a possible systematic shift.

The asymmetry of the neutral kaon is reduced by 41%. Since it is calculated for each decay candidate, no statistical uncertainty can be assigned, and the shift due to the weighting is purely systematic. Finally, $A_{CP}(K^-K^+)$ is shifted by approximately 0.08% which is small compared to the possible statistical shift. Anyhow, the weighting procedure is necessary, and the growing statistic uncertainty accounts for possible shifts of $A_{CP}(K^-K^+)$ due to the weighting.

10.3 Consistency

In order to test the stability of the performance of the analysis, consistency checks are made. The idea of such a test is to repeat the analysis for sub-samples of the whole data-set. For this purpose, the data-set is divided into bins of a specific variable. Since for this study, four different decays are combined, there are only a few of these variables which have to be common for all channels. One possibility is already implemented in the structure of the analysis by treating the four data categories given by the year of recording and the magnet polarity independently. As discussed in section 10.1, the four obtained values are consistent.

The second consistency check performed in the scope of this thesis divides the data according to the time of recording. For the LHC, the corresponding variable

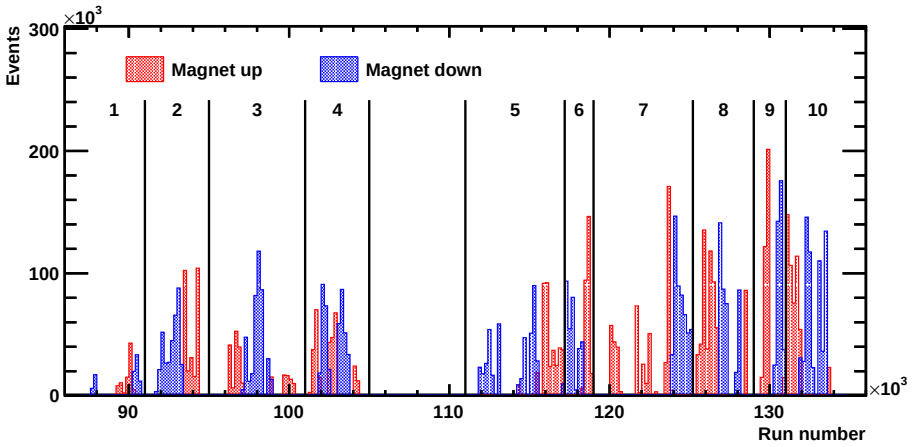

Figure 10.5: Number of recorded and selected $D^0 \to K^-K^+$ decay candidates as a function of the run number. The periods of magnet polarity up and down are marked by the colors red and blue, respectively. The run number blocks used for a consistency check are indicated by the black lines. Block 1-4 correspond to the data taking period 2011 and block 5-10 contain the data recorded in 2012. The exact definition of these blocks can be found in appendix D.

is called run number and specifies short periods of data taking. The number of recorded and selected $D^{*+} \to D^0(\to K^-K^+)\pi^+_{sl}$ decays as a function of the run number is shown in figure 10.5. As indicated by the black lines in this figure, the data recorded in 2011 is divided into four and the data recorded in 2012 in six sub-samples. Each of these periods is defined by interruptions in data taking and by requiring a certain size and at least one magnet polarity flip. The interruptions in the data taking originate from the LHC and are used for maintenance of the detector. These maintenance activities might change detection asymmetries since the detector is opened and closed which can cause changes in the alignment.

For each of these ten periods, the analysis is repeated independently for both magnet polarities. In order to achieve a better stability of the fit, some background and signal parameters are fixed to the values of the default analysis. Figure 10.6 shows the values of $A_{CP}(K^-K^+)$ obtained for the different sub-samples. The p-values for the hypothesis of no dependency are given as well for the two magnet polarities independently, as also for the polarity averaged results. None of these probabilities exceeds 10 %. One possible explanation is a production or detection asymmetry which, one the one hand changes over time, and on the other side is not cancelled perfectly. Another explanation, can be instabilities of the weighting procedure presented in chapter 8. Such instabilities can arise due to statistical fluctuations in the three dimensional binning when using small data samples. This effect can be further investigated by using the kinematic weights created by the default analysis. Whereas this solves the problems of too less events for the weighting, changes in the

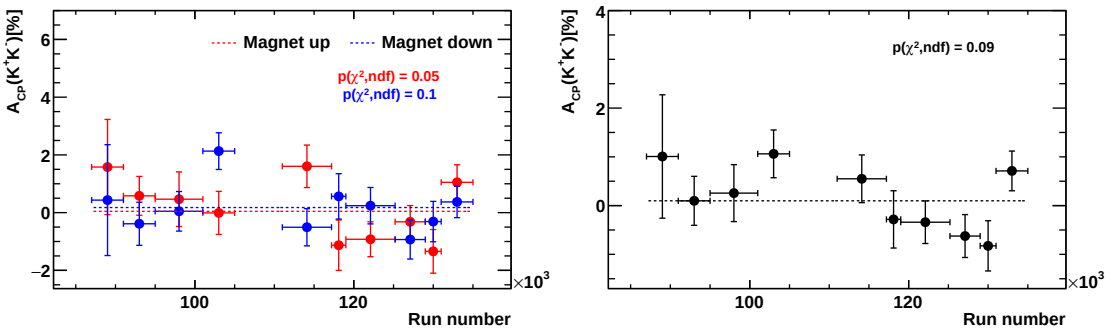

(a) Magnet polarities shown individually **(b)** Magnet polarities averaged

Figure 10.6: $A_{CP}(K^-K^+)$ as a function of the run number. In (a) the values obtained using data recorded with magnet polarity up and down are shown independently. In (b) the polarity averaged values are shown. The data was split according to the run number blocks indicated in figure 10.5, and the full analysis was performed for each of the sub-samples. Additionally, the p-values for the hypothesis of being independent of the run number are quoted.

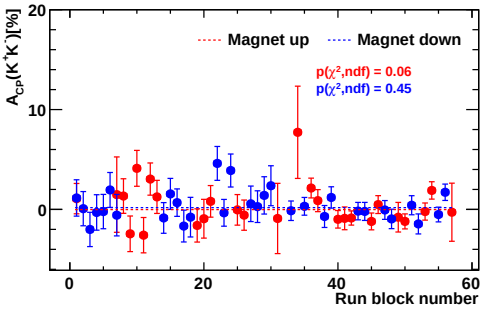

Figure 10.7: $A_{CP}(K^-K^+)$ as a function of the number of the run block using the kinematic weights of the default analysis. The run blocks are defined in appendix D. Additionally, the p-value for the hypothesis of being independent of the run block number is given.

kinematic distributions within one of the four data categories[1] can not be taken into account. When using the kinematic weights of the default analysis, a much finer division into run number periods can be chosen since no large samples are needed for the creation of kinematic weights. Therefore, the whole data-set is divided into 56 run blocks. Their specific definition can be found in appendix D. In figure 10.7, the values for $A_{CP}(K^-K^+)$ for each of these run blocks is shown. The p-value for the hypothesis of no dependency is separately given for magnet polarity up and magnet polarity down. Here, no significant dependency is observed.

[1] Modifications of the Hlt1 trigger configuration during the 2012 are an example for such changes. See table 6.1.

Chapter 11

Estimation of systematic uncertainties

This chapter is dedicated to the study of the sources of the systematic uncertainties. Among the considered sources are the kinematic weighting procedure, the signal and background modelling and the presence of events with more than one candidate. In addition, possible biases coming from the selection requirements are taken into account.

11.1 Extraction of raw asymmetries

The raw asymmetries are extracted with binned log-likelihood fits to the mass difference distribution Δm of the charm mesons D^{*+} and D^0 or to the mass of the D^+ meson. The fit models used are described in chapter 7. Since the choice of the fit model can bias the extraction of the physics parameters, different signal and background models are systematically tested. For this purpose, the data samples before weighting are used in order to ensure the highest statistic significance.

For the D^0 decays, the following changes to the default fit model, cf. chapter 7, are apllied:

- A single Gaussian distribution is chosen as a signal model. This is an extremely simple model and it does not describe the Δm distribution correctly.

- The sum of two Gaussian distributions with a shared value of the mean parameter are tested. Since this is a symmetric signal model, it can not describe any asymmetric tails. Thus, the systematic effects originating from such structures is tested.

- By replacing the third Gaussian distribution of the default model which is allowed to have a different mean parameter by a bifurcated Gaussian with the same mean parameter as the first two Gaussian distributions, an alternative model for an asymmetric tail is tested. The explicit definition of the bifurcated Gaussian can be found in chapter 7.2.2.

Table 11.1: Measured raw asymmetries (in %) of D^0 decays using different fit models. The mean raw asymmetries, cf. chapter 5.3, of all four data categories are used without any kinematic weighting.

Change	$\boldsymbol{D^0 \to K^- K^+}$	$\boldsymbol{D^0 \to K^- \pi^+}$
Default	-0.973 ± 0.047	-2.016 ± 0.032
Gaussian as signal pdf	-0.987 ± 0.048	-2.018 ± 0.033
Double Gaussian as signal pdf	-0.981 ± 0.048	-2.009 ± 0.032
Double Gaussian + bifurcated Gaussian as signal pdf	-0.983 ± 0.047	-2.014 ± 0.032
Mixed polynomial exponential function as background pdf	-0.974 ± 0.047	-2.016 ± 0.032
150 bins per tag	-0.973 ± 0.047	-2.016 ± 0.032
Maximal difference	0.014	0.0071

- An empirical background model consisting of a first order polynomial and a an exponential part is tested as an alternative. It is able to describe the threshold as well as the default model, and it is described in appendix A.1.

- To test the impact of the number of bins of the binned maximum-likelihood fit, this number is reduced to 150 per tag.

In table 11.1, all tested fit models for the D^0 decays and the raw asymmetries obtained are listed. For the $D^0 \to K^- K^+$ channel, the value obtained by the single Gaussian distribution shows the largest deviation from the default value. In the case of the $D^0 \to K^- \pi^+$ decay, the signal model consisting out of the double Gaussian distribution yields the largest deviation. These maximal differences are taken as the systematic uncertainty of the asymmetry extraction of the respective channel.

For the D^+ decays, similar changes to the default fit model, cf. chapter 7, are applied. Besides the already described single and double Gaussian distribution for the signal model and the different number of bins, the following changes are tested:

- By replacing the bifurcated Gaussian distribution of the default model by a Crystal Ball function [41], an alternative model for asymmetric tails is tested. This function consists of a Gaussian inner part and a power-law tail. The explicit definition of the Crystal Ball function can be found in appendix A.1.

- As an alternative background description, a second order polynomial is tested.

In table 11.2 all tested fit models for the D^+ decays and the raw asymmetries obtained by these are listed. For both decays, the raw asymmetry measured by a single Gaussian distribution as signal model shows the largest deviation from the default value. In analogy to the D^0 decays, these maximal differences are taken as the systematic uncertainty of the asymmetry extraction of the respective channel.

Table 11.2: Measured raw asymmetries (in %) of D^+ decays using different fit models. The mean raw asymmetries, cf. chapter 5.3, of all four data categories are used without any kinematic weighting.

Change	$\boldsymbol{D^+ \to K^-\pi^+\pi^+}$	$\boldsymbol{D^+ \to \overline{K}^0\pi^+}$
Default	-1.757 ± 0.041	-0.804 ± 0.056
Gaussian as signal pdf	-1.766 ± 0.041	-0.821 ± 0.056
Double Gaussian as signal pdf	-1.752 ± 0.041	-0.804 ± 0.056
Double Gaussian + Christal Ball function as signal pdf	-1.757 ± 0.041	-0.804 ± 0.056
Exponential as background pdf	-1.758 ± 0.041	-0.805 ± 0.056
150 bins per tag	-1.757 ± 0.041	-0.804 ± 0.056
Maximal difference	0.0094	0.017

Since all measured raw asymmetries are combined linearly to extract $A_{CP}(K^-K^+)$, the final systematic uncertainty due to the extraction of raw asymmetries is given by the quadratic sum of the maximal shift in each channel. The result is shown in table 11.13.

11.2 Weighting procedure

The weighting procedure described in chapter 8 is a crucial part of this analysis. Therefore, it is important to estimate the systematic uncertainty arising from the specific choice of the weighting strategy.

11.2.1 Varying the weighting parameters

An estimation of this uncertainty can be obtained by varying parameters of the weighting procedure. The whole analysis is then repeated with this weighting configuration. All systematic tests can be found in table 11.3.

An obvious variation is the usage of different numbers of bins for the weighting. Hence, the analysis is performed with 25/15 bins in each dimension of the weighting. The used number of bins can have two effects on the performance of the weighting. When choosing a high number of bins, the statistic significance of each bin content is reduced. Therefore, the weighting is no longer stable and a lot of unnaturally large and small weights would be the result. In contrast, when choosing a small number of bins, structures of the distributions can not be resolved and there are still large differences after the weighting.

In order to avoid large weights which would drastically reduce the statistical power of the weighted sample, in each step weights larger than 10 are set to 10. Since these are numbers motivated only by experience, one needs to test the impact of this specific choice. This is done by totally ignoring weights higher then 10 in each

Table 11.3: Systematic checks of the weighting procedure. All performed changes and the thereby obtained final CP asymmetry are listed. The maximal difference to the value obtained with the default weighting strategy is quoted.

Systematic check	$\boldsymbol{A_{CP}(K^-K^+)}$ [%]
Default	0.078 ± 0.163
Weighting only in p_T,η	0.104 ± 0.154
Weighting with 15 bins	0.069 ± 0.160
Weighting with 25 bins	0.009 ± 0.163
Set high weights in each step to 1	0.050 ± 0.152
Maximal difference	0.070

step and setting them to 1.

To test the effect of the multiple weighting steps performed in the weighting of $D^0 \to K^-\pi^+$ and $D^+ \to \overline{K}^0\pi^+$ candidates to the channel $D^+ \to K^-\pi^+\pi^+$, a reduced weighting process is used. The weighting between the two D^0 decays is not varied since there is only one step necessary. Since at least the production asymmetries do not depend on the azimuthal angle ϕ, the weighting in ϕ of any of the involved particles is omitted. Additionally, only two steps are performed for the weighting of $D^0 \to K^-\pi^+$ and $D^+ \to \overline{K}^0\pi^+$ candidates to the channel $D^+ \to K^-\pi^+\pi^+$, respectively. They are given by

1. weighting in p_T,η of the kaon and p_T of the pion
2. weighting in p_T,η of the pion and p_T of the kaon

for the weighting of the D^0 channel and by

1. weighting in p_T,η of the D^+ meson and p_T of the pion
2. weighting in p_T,η of the pion and p_T of the D^+ meson

for the weighting of the D^+ channel.

The usage of a higher number of bins causes the largest shift, whereas the reduction of the bin number, the alternative way of dealing with large weights, and the reduced weighting strategy have only small effects.

The final systematic uncertainty arising from the specific choice of the weighting configuration is taken as the maximal difference between the various results obtained with the modified weighting schemes and the default value. This uncertainty is then propagated in the total systematic uncertainty.

11.2.2 Cancellation of the nuisance asymmetries by modelling the raw asymmetries dependencies

Another way to estimate a possible systematic shift due to the weighting procedure is based on modelling the dependencies of the individual detection and production

Table 11.4: Modelled dependencies of the individual detection or production asymmetries. They are motivated by observations made in [5], and chapter 7.4.2.

Particle	**Modelled asymmetry**[%]	**Constant**[%]
D^{*+}/D^{+}	$(-0.5 - 0.6\, e^{\eta - 4})$	-0.75
K^{-}	$\left(\left[-0.8 - 2.5\, e^{-\frac{p}{10000\,\mathrm{MeV}/c}}\right]\left[1 - 0.6\cos 2\phi - 0.04\phi^2\right]\right)$	-1
π^{+}_{sl}	$\left(-1.8\, e^{-\frac{p_T}{200\,\mathrm{MeV}/c}}\left[1 - 0.6\cos 2\phi\right]\right)$	-0.25
π^{+}	$\left(-0.9\, e^{-\frac{p_T}{5000\,\mathrm{MeV}/c}}\left[1 - 0.6\cos 2\phi\right]\right)$	0

asymmetries. Using these models and neglecting a possible CP asymmetry, the raw asymmetry for the channel $D^{*+} \to D^0(\to K^-K^+)\pi^+_{sl}$ is for example calculated by summing over the background subtracted decay candidates:

$$A_{raw}(D^0 \to K^-K^+) = \frac{1}{N}\sum_{i=0}^{N}\left[A_P(p_T^{D^*}, \eta^{D^*}) + A_D(p_T^{\pi_{sl}}, \eta^{\pi_{sl}}, \phi^{\pi_{sl}})\right]. \tag{11.1}$$

Here, N is the background subtracted yield of this data sample and $A_P(p_T^{D^*}, \eta^{D^*})$ and $A_D(p_T^{\pi_{sl}}, \eta^{\pi_{sl}}, \phi^{\pi_{sl}})$ are the modelled production and detection asymmetry of the D^{*+} meson and the slow pion. By using directly the data as input for this calculation, the correct correlation between the different kinematic variables of the involved particles is obtained. The raw asymmetries are analogously calculated for all channels and data categories and are then combined to the final quantity $A_{CP}(K^-K^+)$. The neutral kaon asymmetry is neglected since it is not cancelled by the subtraction of two raw asymmetries, but it is directly calculated. Then, the obtained weights from chapter 8 are additionally applied event by event and the raw asymmetries are again calculated and combined.

Since no CP asymmetry is implemented in these calculations, the obtained value for $A_{CP}(K^-K^+)$ is a measure for the impact of the differences in the kinematic distributions. Whereas for the case of the not weighted samples a deviation from zero is expected, the value obtained with kinematic weights should be zero, assuming a perfect performance of the weighting.

As it is not possible to disentangle all the different detection and production asymmetries, unexpectedly strong, and therefore conservative, dependency models are chosen. They are meant to mimic the observations made in [5], and chapter 7.4.2. The dependencies of the various nuisance asymmetries are listed in table 11.4.

Besides these dependencies, values for alternatively constant asymmetries are given. They are motivated by the qualitative discussion of the contribution of the different nuisance asymmetries in chapter 7.4.1. In order to get a conservative estimation of a possible systematic shift, A_{CP} was calculated for every possible combination of constant or variable asymmetries given in table 11.4. This ensures that the chosen extreme dependencies do not cancel by chance due to the correlation

of the different particles. For the same reason, this procedure was repeated with assuming no dependence on ϕ of any of the involved particles. The maximal deviation from zero of A_{CP} for the non-weighted samples is 0.23%, whereas the value obtained from the weighted samples deviates at most by 0.03%. This deviation by 0.03% is, therefore, a measure of the systematic uncertainty arising form the weighting procedure.

Compared to the estimation of the systematic uncertainty by testing alternative weighting configurations, this method directly evaluates the performance of the weighting procedure. Therefore, an intrinsic systematic bias which is independent of the exact chosen weighting configuration can be estimated. In order to get a conservative estimation of a possible systematic shift due to the weighting, this number is assumed to be independent of the systematic uncertainty arising from testing alternative weighting configurations. Therefore, it is also listed in table 11.13.

11.3 Fiducial cuts

In chapter 6.4.4, the fiducial cuts applied to the slow pion in the D^{*+} decays are described. Besides the slow pion in the two D^{*+} decays, there are other particles in the decay modes employed in this analysis, which are part of a CP asymmetric final state. In the case of the decay $D^0 \to K^-\pi^+$ the kaon and the pion are such particles. Also the charged kaons and pions in the D^+ meson decays have to be considered. For these particles, fiducial regions with large detection asymmetries can cause non-linearities in the interplay of different sources of asymmetries, cf. chapter 5.2.1. The impact of this effect on the final CP asymmetry has to be studied. Therefore, fiducial regions with large asymmetries are excluded for these particles.

Figure 11.1 shows the raw asymmetry of the channels $D^0 \to K^-\pi^+$, $D^+ \to K^-\pi^+\pi^+$ and $D^+ \to \overline{K}^0\pi^+$ as function of p_z and p_x of the respective final state particle. As an example, data collected in 2012 with magnet polarity up is chosen. The stripes with large asymmetries come from the combination of the bending due the magnetic field and the material of the detector. The edge regions at low p_z show large asymmetries which can be explained analogously to the same regions in the fiducial volume of the slow pions. There, particles of one charge are bent out of the detector which therefore result in maximal asymmetries.

Regions which are excluded as a systematic test are indicated by black lines. A detailed description of these regions can be found in appendix A.2. The final value of $A_{CP}(K^-K^+)$ obtained after applying these fiducial cuts is quoted in table 11.5. Compared to other sources of systematic uncertainties, the obtained difference to the default value is negligible.

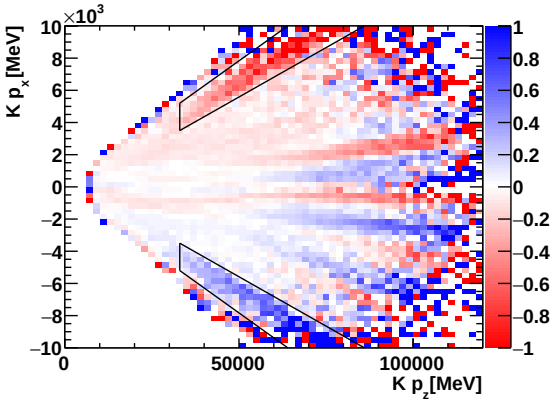

(a) Kaon of $D^0 \to K^-\pi^+$

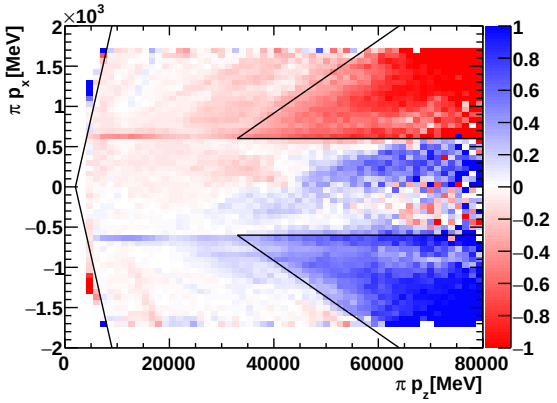

(b) Pion of $D^0 \to K^-\pi^+$

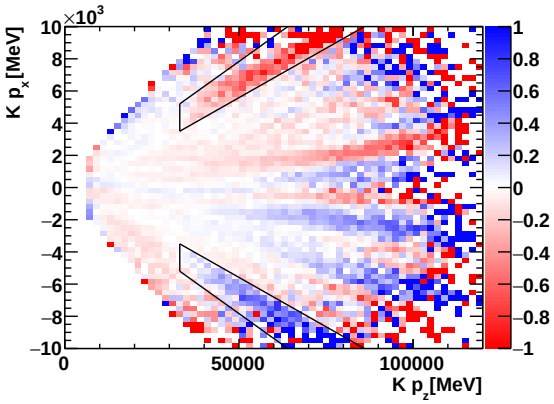

(c) Kaon of $D^+ \to K^-\pi^+\pi^+$

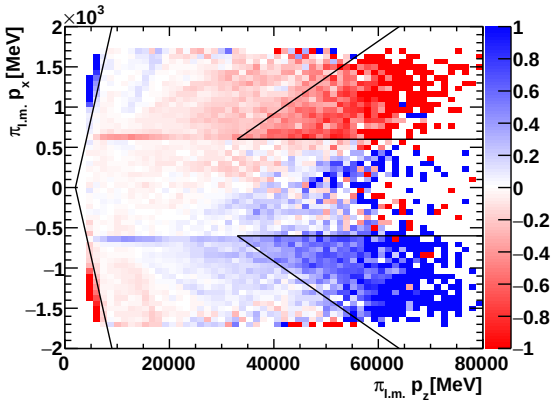

(d) Low momentum pion of $D^+ \to K^-\pi^+\pi^+$

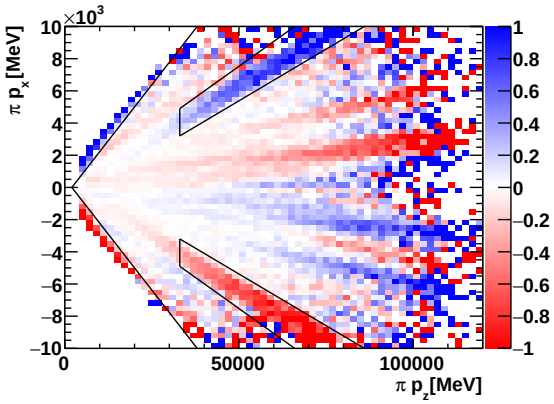

(e) High momentum pion of $D^+ \to K^-\pi^+\pi^+$

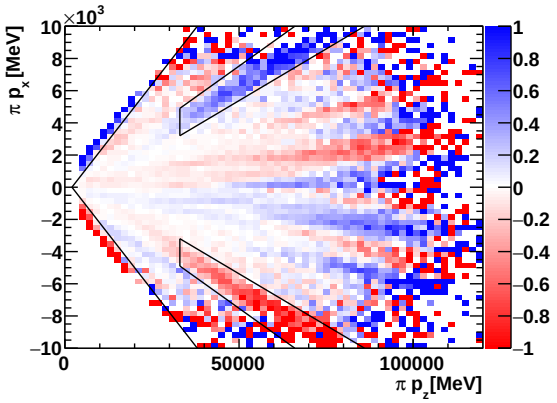

(f) Pion of $D^+ \to \overline{K}^0\pi^+$

Figure 11.1: Raw asymmetries of the channels $D^0 \to K^-\pi^+$, $D^+ \to K^-\pi^+\pi^+$ and $D^+ \to \overline{K}^0\pi^+$ as function of p_z and p_x of the respective final state particle. Regions which are excluded as a systematic test are indicated by the black lines. Data from 2012 with magnet polarity up is used.

Table 11.5: The asymmetry $A_{CP}(K^-K^+)$ obtained when excluding the additional fiducial regions.

Systematic check	$\boldsymbol{A_{CP}(K^-K^+)}$ [%]
Default	0.0785 ± 0.1632
Additional fiducial cuts	0.0803 ± 0.1635
Difference	0.0018

Table 11.6: Obtained final asymmetries with a looser requirement on the D^0 mass in $D^0 \to K^-\pi^+$ decays.

Systematic check	$\boldsymbol{A_{CP}(K^-K^+)}$ [%]
Default	0.078 ± 0.163
Wide m(D^0) window for $D^0 \to K^-\pi^+$	0.035 ± 0.162
Difference	0.044

11.4 Mass range of D^0 candidates

In order to suppress combinatoric background in the decays $D^{*+} \to D^0(\to h^-h^+)\pi^+_{sl}$ the mass of the D^0 candidate is required to lie in the range $[1850{,}1884]\,\mathrm{MeV}/c^2$, cf. chapter 6.4.2. If the shape of the mass distribution is different for D^0 and $\overline{D}^0$ mesons, this might lead to an additional nuisance asymmetry. A slightly different mean value or a different width of the mass peak of reconstructed D^0 candidates with respect to $\overline{D}^0$ candidates would lead for example to different selection efficiencies for the two flavour categories.

For the decay $D^0 \to K^-K^+$ such an effect is not possible since the final state is symmetric. However, the measured raw asymmetries of $D^{*+} \to D^0(\to K^-\pi^+)\pi^+_{sl}$ might be influenced by the choice of the $m(D^0)$ window. The asymmetric interaction with matter for K^- and K^+ mesons, cf. chapter 2.4, could for example influence the momentum resolution of the respective particle. In order to estimate the impact of the chosen $m(D^0)$ range, the analysis is independently performed with a loosened requirement on the mass of the D^0 meson in $D^0 \to K^-\pi^+$ decays. This loosened requirement, $m(D^0) \in [1822.5, 1910]\,\mathrm{MeV}/c^2$, is based on a selection requirement in the trigger and on a two-dimensional fit which is presented in section 11.8.

In table 11.6, the values for $A_{CP}(K^-K^+)$ obtained by the default and the modified selection are shown. The difference is taken as a systematic uncertainty. It is found to be a little bit smaller than the uncertainty arising from the weighting procedure. Further studies which were out of the scope of this thesis are necessary in order to investigate the origin of this shift. Thereby, it might be possible to adapt the D^0 mass window and to reduce this systematic uncertainty.

Table 11.7: Obtained final asymmetries with different PID requirements. The exact values for the loose and tight selection are given in the text.

Systematic check	$\boldsymbol{A_{CP}(K^-K^+)}$ [%]
Default	0.078 ± 0.163
Loose PID requirements	0.048 ± 0.157
Tight PID requirements	0.113 ± 0.171
Maximal difference	0.035

11.5 Particle identification

For the final state kaons and pions, the $\mathrm{DLL}_{K\pi}$ requirements, cf. chapter 6.4.2, are tightened and equalized between the different channels with respect to the stripping requirements. The impact of these requirements on $A_{CP}(K^-K^+)$ is tested by varying the PID requirements and independently performing the analysis with the new data sets. Since this has an effect on the misidentification probability of the final state particles, it could have an effect on background which could leak in the signal peak of one of the four used channels.

First, the analysis was repeated with loosened requirements, namely $\mathrm{DLL}_{K\pi} > 5$ for kaons and $\mathrm{DLL}_{K\pi} < -5$ for pions. Then, it was performed with tightened requirements, namely $\mathrm{DLL}_{K\pi} > 9$ for kaons and $\mathrm{DLL}_{K\pi} < -9$ for pions. Table 11.7 shows the obtained final asymmetries. Both $A_{CP}(K^-K^+)$ values obtained with alternative PID requirements show a deviation from the default value. Since these different requirements result in different data samples, the observed shifts can partially be of statistical nature. Anyhow, the maximal deviation is taken as a systematic uncertainty.

11.6 Hlt1 configuration

In chapter 6.4.3 the chosen Hlt1 configuration is described. It aims to exclude regions in the p_T distributions of certain particles which would cause problems during the weighting. Since the the Hlt1 trigger uses also other variables than the transverse momentum, this could introduce a bias. Therefore, the analysis is performed independently without any specific Hlt1 selection after the stripping selection. The only additional requirement applied to exclude decay candidates with a low p_T pion and kaon in $D^+ \to K^-\pi^+\pi^+$ events is: $p_T > 1700\,\mathrm{Mev}/c$ for the kaons in $D^+ \to K^-\pi^+\pi^+$ and $D^0 \to K^-K^+$ decays. The additional requirement on the transverse momentum of the pion in these decays is omitted. Table 11.8 shows the value of $A_{CP}(K^-K^+)$ obtained with this selection configuration. The deviation with respect to the default value, is of the same order as the systematic uncertainties arising from the particle identification or the asymmetry extraction.

Table 11.8: Obtained final asymmetries without using any specific offline Hlt1 trigger selection. The exact changes of the selection with respect to the default are given in the text.

Systematic check	$\boldsymbol{A_{CP}(K^-K^+)}$ [%]
Default	0.078 ± 0.163
No Hlt1 requirements	0.046 ± 0.175
Difference	0.033

Table 11.9: Fraction of events which contribute more than one candidate to the D^0 candidates. Data from 2012 was used.

Magnet polarity	**Channel**	**MC fraction[%]**
Up	$D^0 \to K^-K^+$	6.4
	$D^0 \to K^-\pi^+$	4.8
Down	$D^0 \to K^-K^+$	6.5
	$D^0 \to K^-\pi^+$	4.9

11.7 Multiple candidates

For the D^{*+} decays used in this analysis, a relative high fraction of all events contains more than one candidate. In table 11.9, the fraction of events with multiple candidates is quoted for 2012 data. These multiple candidates (MC) dominantly arise from combining the same D^0 meson with multiple slow pion candidates. If these additional slow pions correspond to a real particle, they only increase the amount of combinatorial background and do not affect the asymmetry. What can also happen is that a real slow pion is reconstructed twice and this could bias the asymmetry.

Therefore, two different treatments of multiple candidates are tested. One possibility is to accept only one decay candidate per event. This is done by randomly selecting the candidate. Another possibility is to reject all events with multiple candidates. Both selections are tested and the obtained final values for $A_{CP}(K^-K^+)$ are listed in table 11.10. It is hard to disentangle the two types of additional slow pions. Therefore, the full difference to the default selection is taken as systematic uncertainty. This difference is comparable to the systematic uncertainties arising from the previous tests.

Table 11.10: The asymmetry $A_{CP}(K^-K^+)$ obtained with the respective treatments of multiple candidates. The maximal difference to the default selection is used as systematic uncertainty.

Systematic check	$\boldsymbol{A_{CP}(K^-K^+)}$ [%]
Default	0.078 ± 0.163
Select one random multiple candidate	0.052 ± 0.164
Reject all multiple candidates	0.042 ± 0.166
Maximal difference	0.037

11.8 Estimation of possible peaking background sources

In chapter 6.2.3, possible background sources which may bias the extracted raw asymmetries are discussed. Whereas the Cabibbo-favoured decays are expected to be only affected by combinatoric background, the Cabibbo-suppressed decay $D^0 \to K^-K^+$ might be affected by the decay $D^0 \to K^-\pi^+\pi^0$. Like in the signal decay into two kaons, the D^0 meson originates from a D^{*+} meson. If the neutral pion is not reconstructed, and the charged pion is mis-identified as a kaon, the reconstructed D^0 candidate may have a mass that leaks into nominal D^0 mass window.

In order to estimate the effect of this peaking background on the extracted raw asymmetry, a two-dimensional fit to the mass difference Δm and the mass of the D^0 candidate, m_{D^0}, is performed. For this purpose, the shape in m_{D^0} and Δm of partially and mis-reconstructed $D^0 \to K^-\pi^+\pi^0$ decays is determined using simulated decays. These simulation is taken from an ongoing LHCb study using a similar reconstruction strategy [32]. It is out of the scope of this thesis to create custom-made simulations for exactly the selection requirements used in this analysis. Anyhow, the used simulations should be precise enough to estimate the effect of this specific background. In order to be able to fit the m_{D^0} distribution, the chosen m_{D^0} window, cf. table 6.6, is loosened to: $m(D^0) \in [1822.5, 1910]\,\mathrm{MeV}/c^2$.

In the following, the different components of the used fit model are briefly described.

- The signal component is modelled in Δm by using the same PDF as for the one-dimensional fit. Since all signal decays have to contain a correct reconstructed D^0 meson, the signal component is part of the peak in the m_{D^0} distribution. This peak is modelled using the sum of a double and a bifurcated Gaussian distribution. All parameters of this signal component are allowed to float.

- The random pion background originates from correctly reconstructed D^0 mesons which are combined with random pions. Therefore, this component is modelled in m_{D^0} by using the same PDF as the signal component. In the Δm distribution, the random pion background is modelled in analogy to the back-

ground PDF in the one-dimensional fit. Like in the one-dimensional fit, only the threshold parameter is fixed to the nominal pion mass.

- The combinatorial background of the D^0 candidate is described by a single exponential function in the case of the m_{D^0} distribution. Since these D^0 candidates originate by definition not from a real D^{*+} meson, the combinatorial background is modelled in the Δm distribution by the same PDF as the random pion background.

- The background originating from $D^0 \to K^-\pi^+\pi^0$ decays is modelled using the discussed simulations. In the m_{D^0} distribution, it is modelled using a single exponential function with a fixed decay constant. For the Δm distribution, the sum of a Gaussian distribution and an empirical function consisting out of an exponential, a polynomial, and a power law part is chose. The detailed parametrization is given in appendix A.1. All parameters besides the mean and width of the Gaussian distribution are fixed to the values obtained in the simulation.

- An additional background source which is present in the m_{D^0} distribution is the decay $D_s^+ \to K^-K^+\pi^+$. If the positively charged kaon is not reconstructed, and additionally the pion is misidentified as a kaon, this channel leaks into the low-mass sideband of the m_{D^0} distribution. This component is described by a single exponential function in the m_{D^0} distribution. The decay constant of this exponential function is fixed to a value obtained by a simulation. This simulation is part of the ongoing analysis which was mentioned earlier [32]. In the Δm distribution, this component can be modelled by the same PDF which is used for the random pion background.

Combining all components, a simultaneous two-dimensional fit to the two tag categories is performed. The relative fractions of the individual components are allowed to differ between the tag categories in order to account for different asymmetries of the several background contributions. All other parameters used to describe the m_{D^0} distribution are shared between the two tag categories.

The two-dimensional fit is performed for the four different data samples of $D^0 \to K^-K^+$ decays and the kinematic weighting procedure is redone. Figure 11.2 shows the Δm and m_{D^0} projections for the two flavour categories. In table 11.11, the mean measured raw asymmetry in the channel $D^0 \to K^-K^+$ is shown for the default analysis and for the two-dimensional fit. The difference is assigned as a systematic uncertainty. It is found to be two order of magnitude smaller than the leading systematic uncertainty. Anyhow, it is listed in table 11.13 and taken into account when calculating the total systematic uncertainty.

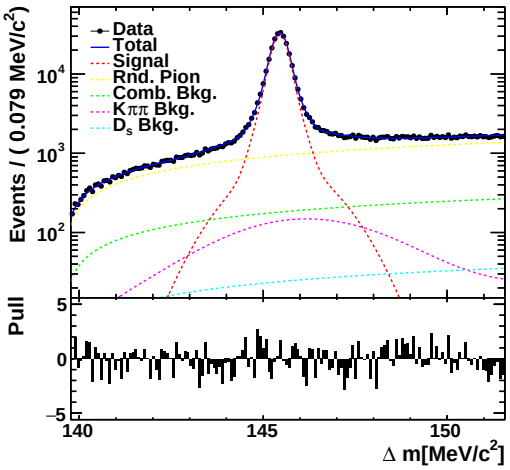

(a) Negatively tagged Δm projection

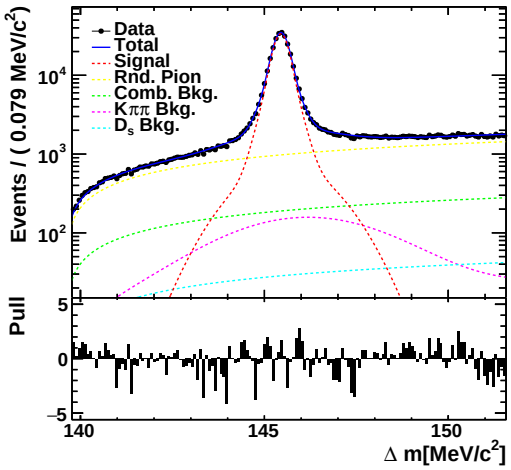

(b) Positively tagged Δm projection

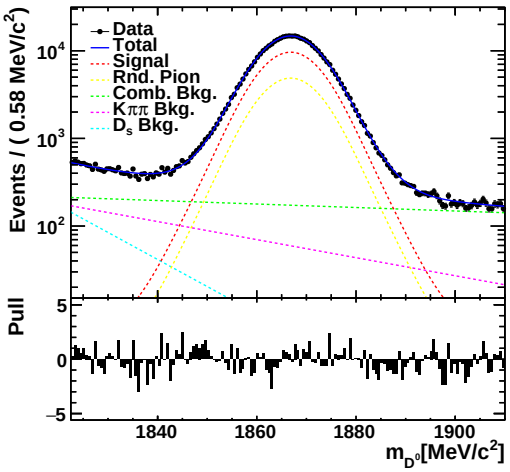

(c) Negatively tagged m_{D^0} projection

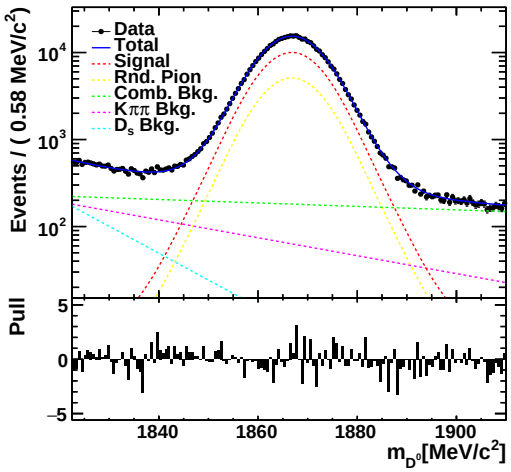

(d) Positively tagged m_{D^0} projection

Figure 11.2: Fit projections of the two dimensional fit to the $D^0 \to K^-K^+$ sample taken in 2012 with magnet polarity up. In (a) and (b) the Δm projection of the negatively and positively tagged decays are shown. The respective m_{D^0} projections can be seen in (c) and (d). The different background contributions discussed in the text are shown for both mass dimensions.

Table 11.11: The mean raw asymmetry of the channel $A_{raw}(D^0 \to K^-K^+)$ obtained by the default analysis and the two dimensional fit. The difference is used as systematic uncertainty.

Systematic check	$\boldsymbol{A_{raw}(D^0 \to K^-K^+)}$ [%]
Default	-0.84426 ± 0.08643
2D fit allowing peaking background	-0.84474 ± 0.08695
Difference	0.00048

11.9 Estimation of the impact of secondary charm mesons

The selection criteria presented in chapter 6 include requirements on the impact parameter significance of the $D^0(D^+)$ mesons with respect to the PV. This aims to suppress so called secondary charm mesons which originate from B-mesons. However, a certain fraction of secondary mesons, f_{sec}, is still present. These decay candidates might influence the cancellation of the charm meson production asymmetries between the two D^{*+} and the two D^+ channels.

As an example, the impact of secondary charm mesons on the production asymmetries in $D^{*+} \to D^0(\to h^-h^+)\pi^+_{sl}$ decays is discussed. The effective production asymmetry, A_P^{eff}, of D^{*+} mesons is given by:

$$A_P^{eff} = (1 - f_{sec})A_P + f_{sec}A_{sec}, \tag{11.2}$$

where A_P is the production asymmetry of prompt D^{*+} mesons, $A_P \approx 0.96\%$ see chapter 5.1.1, and A_{sec} the asymmetry of D^{*+} mesons originating from B-meson decays. The latter arises for the production asymmetry of B-mesons. When subtraction the raw asymmetries of the channels $D^{*+} \to D^0(\to K^-K^+)\pi^+_{sl}$ and $D^{*+} \to D^0(\to K^-\pi^+)\pi^+_{sl}$, cf. chapter 5.2.2, a different secondary fractions of these channels can lead to a systematic shift, Δ_{sec}:

$$\begin{aligned}\Delta_{sec} = A_P^{eff}(K^-K^+) - A_P^{eff}(K^-\pi^+) =& (1 - f_{sec}^{K^-K^+})A_P + f_{sec}^{K^-\pi^+}A_{sec} \\ &-(1 - f_{sec}^{K^-K^+})A_P + f_{sec}^{K^-\pi^+}A_{sec} \\ =& (f_{sec}^{K^-K^+} - f_{sec}^{K^-\pi^+})(A_{sec} - A_P).\end{aligned} \tag{11.3}$$

An analogous equation counts for the two D^+ channels. In a previous LHCb analysis which used the same requirement on the impact parameter significance, the secondary fractions were measured to be 2.82% for the final state K^-K^+ and 3.39% for the final state $\pi^-\pi^+$ [42][3]. Since the final state $K^-\pi^+$ is more similar to K^-K^+ than the final state $\pi^-\pi^+$, the difference between these fractions, $\sim 0.6\%$, can be used as a conservative value for $f_{sec}^{K^-K^+} - f_{sec}^{K^-\pi^+}$. In the case of the D^+ decays, no appropriate numbers from other analysis are present. Only from the analysis presented in Ref. [43] the fraction of secondary charm mesons in $D^+ \to K^-\pi^+\pi^+$ decays can be estimated to be approximately 2%. Since for the decay $D^+ \to \overline{K}^0\pi^+$ no suitable number can be found, further studies will be necessary which are out of the scope of this thesis. In order to make a conservative estimation, the full 2% are taken as the difference of secondary fractions.

Most of the secondary charm mesons originate from decays of B^+ and B^0 mesons which are the most common B-hadrons at LHCb [44]. The contribution from other mesons or baryons containing a b-quark can be neglected [45]. B^+ and B^0 mesons are produced in the same amount in the LHCb experiment [44] but show different relative branching fractions for the decays into D^+ mesons. The inclusive branching

Table 11.12: Inclusive branching fractions of B-meson to charm-meson decays. The values are taken from Ref. [11].

	$\Gamma(D^+X)/\Gamma[\%]$	$\Gamma(D^-X)/\Gamma[\%]$
B^+	2.5 ± 0.5	9.9 ± 1.2
B^0	2.3 ± 1.2	36.9 ± 3.3

ratios are listed in table 11.12. Assuming that D^{*+} mesons are produced in the same relative fractions as D^+ mesons, the asymmetry of secondary charm mesons can be written as:

$$A_{sec} = \frac{1}{2.5 + 9.9 + 2.3 + 36.9} \left[(2.3 + 36.9) A_{sec}^{B^0} + (2.5 + 9.9) A_{sec}^{B^+} \right], \tag{11.4}$$

where $A_{sec}^{B^0}$ and $A_{sec}^{B^+}$ are the asymmetries of charm production via B^0 and B^+ mesons.

The production asymmetry of B-mesons is measured by the LHCb collaboration to be -0.6 ± 0.6 for B^+ [46] and -0.35 ± 0.8 for B^0 mesons [47]. These asymmetries do not translate directly in the asymmetries of secondary charm but are diluted by two effects. The first is the fact that not only anti-charm mesons but also charm mesons can be produced in B-meson decays, see table 11.12. The second effect which dilutes the B-meson production asymmetries is the mixing of $B^0 \leftrightarrow \overline{B}^0$ mesons. In general, approximately 18.7% of neutral B-mesons decay as a different flavour state as they were produced [11]. This number can be taken as a conservative estimation since the requirements applied in order to select prompt charm mesons allow only secondary charm mesons originating from relatively short lived B-mesons. For these short lived B-mesons, the probability for an oscillation is relatively small. By combining these two effects, the dilution factors for B^+ and B^0 mesons can be calculated to be 0.60 and 0.55, respectively. As an example, the calculation of the dilution factor for B^+ mesons is shown in more detail. Given the asymmetry[1] of produced B^+ mesons,

$$A_{B^+} = \frac{N_{B^-} - N_{B^+}}{N_{B^-} + N_{B^+}}, \tag{11.5}$$

and the fraction of opposite and right sign charm mesons produced in B^+-meson decays, f_{ws} and f_{rs}, the effective production asymmetry of secondary charm mesons stemming from B^+ mesons, $A_{sec}^{B^+}$, can be calculated as:

$$A_{sec}^{B^+} = \frac{f_{rs} N_{B^-} + f_{ws} N_{B^+} - f_{rs} N_{B^+} - f_{ws} N_{B^-}}{N_{B^+} + N_{B^-}} = (1 - 2 f_{ws}) A_{B^+}. \tag{11.6}$$

Here, the relation $f_{ws} + f_{rs} = 1$ is used. By using the values shown in table 11.12, the fraction f_{ws} can be calculated to be:

$$f_{ws} = \frac{2.5\%}{2.5\% + 9.9\%} = 0.20. \tag{11.7}$$

[1] By convention the asymmetries in the B-meson system are defined via the b-quark and not via the charge of the meson.

Therefore, according to equation 11.6, the dilution factor is 0.6 in the case of B^+ mesons. For B^0 mesons, the mixing effect has to be taken additionally into account by an analogous calculation. The final asymmetries for secondary charm mesons can than be calculated:

$$A_{sec} = \frac{1}{52.6}\left[39.2 \times 0.55 \times (-0.35\%) + 12.4 \times 0.60 \times (-0.6\%)\right] = -0.23\%. \quad (11.8)$$

Assuming the same production asymmetry for D^+ and D^{*+} mesons, the systematic shift due to secondary charm mesons can be estimated by equation 11.3:

$$\Delta_{sec} = (0.6\% + 2\%)\left[-0.23\% - (-0.96\%)\right] = 0.019\%. \quad (11.9)$$

This number is taken as a systematic uncertainty and is listed in table 11.13. Compared with the leading sources of systematic uncertainties, the effect by secondary charm mesons is small.

11.10 Neutral kaon asymmetry

In chapter 9, the neutral kaon asymmetry is calculated. The relative systematic uncertainty on the used model is estimated to be 25%. This corresponds to an absolute uncertainty of 0.011%, see table 9.1. Since the neutral kaon asymmetry contributes linearly to the final value of $A_{CP}(K^-K^+)$, this absolute uncertainty is propagated further as an additional systematic uncertainty on $A_{CP}(K^-K^+)$.

11.11 Summary

In this chapter, the different categories of sources of systematic uncertainties are discussed. For each category, a maximal deviation to the default analysis is given. The sources of the systematic uncertainty are summarized in table 11.13. To obtain the final systematic uncertainty on $A_{CP}(K^-K^+)$, the values are quadratically added. The final result is found to be 0.11%.

The weighting procedure is a crucial part of the analysis and also contributes most to the final systematic uncertainty. All other systematic uncertainties, besides the one arising from the chosen D^0 mass window, are at least by a factor of two smaller and, therefore, contribute only little.

Table 11.13: Systematic uncertainties from the different categories. The quadratic sum is given.

Category	**Systematic uncertainty**[%]
Particle identification	0.035
No Hlt1 requirements	0.033
Additional fiducial cuts	0.0018
Multiple candidates	0.037
Weighting configuration	0.070
Weighting simulation	0.030
D^0 mass window	0.044
Fit model	0.025
Peaking background	0.00048
Secondary charm mesons	0.019
Neutral Kaon asymmetry	0.011
Quadratic sum	0.11

Chapter 12

Final result and summary

This thesis presents the determination of the time-integrated CP violation $A_{CP}(K^-K^+)$ in the singly Cabibbo-suppressed decay $D^0 \to K^-K^+$. For this purpose, the full dataset recorded in 2011 and 2012 by the LHCb detector is used. This corresponds to an integrated luminosity of $\mathcal{L} = 3\,\text{fb}^{-1}$. The flavour of the neutral charm meson at production is measured by selecting only D^0 mesons originating from prompt $D^{*+} \to D^0\pi^+_{sl}$ decays. Thereby, the charge of the accompanying slow pion corresponds to the flavour of the charm meson at production.

The central challenge of this analysis is to cancel the effect of the production asymmetry of the D^{*+} meson and the detection asymmetry of the slow pion. For this purpose, the three Cabibbo-favoured decays $D^{*+} \to D^0(K^-\pi^+)\pi^+_{sl}$, $D^+ \to K^-\pi^+\pi^+$ and $D^+ \to \overline{K}^0\pi^+$ are used. Whereas the additional D^0 meson decay is used to cancel the mentioned production and detection asymmetry, the two decays of the D^+ meson are employed to correct for the detection asymmetry arising from the $K^-\pi^+$ meson pair of this additional D^0 meson decay.

After suppressing possible background sources by a cut-based selection, simultaneous binned likelihood fits to both flavour categories are performed to extract the raw asymmetry present in all four channels. Since the nuisance detection and production asymmetries are momentum dependent, it is necessary that the kinematic distributions of the selected decay candidates in the different channels agree. This is guaranteed by a weighting procedure. As a drawback of this weighting, the effective statistical power of the used samples is reduced by up to 79 %.

Finally, the remaining detection asymmetry of the neutral kaon in the decay $D^+ \to \overline{K}^0\pi^+\pi^+$ is calculated candidate by candidate using a simulation of the detector material. This asymmetry is then combined with the measured raw asymmetries of all four channels in order to obtain the final result for $A_{CP}(K^-K^+)$:

$$A_{CP}(K^-K^+) = (0.08 \pm 0.16(stat) \pm 0.11(syst))\%.$$

The quoted systematic uncertainty is the result of systematic studies of, e.g. the impact of the selection or the chosen weighting procedure. The latter is studied in detail since the weighting is a crucial part of this analysis. The obtained total systematic uncertainty is smaller than the statistic uncertainty. Therefore, it is expected that the precision can be increased when using new larger data samples.

As the value of a previous LHCb analysis which uses semileptonic b-meson to

charm meson decays, $A_{CP}(K^-K^+) = -0.06 \pm 0.15(stat) \pm 0.10(syst)$ [4], the obtained value for the time-integrated CP violation is compatible with the hypothesis of no CP violation. It is shown, that the methods used in the case of semileptonic b-meson decays, can be similarly applied to prompt charm decays and a consistent value for $A_{CP}(K^-K^+)$ with comparable precision is obtained. Since the influence of indirect CP violation on the observable $A_{CP}(K^-K^+)$ depends on the mean decay time of the selected D^0 mesons, a determination of this mean decay time is necessary in order to extract values for direct and indirect CP violation.

Beside this, further studies of possible background sources and the impact of secondary charm mesons originating from b-hadrons are necessary as both are not investigated in detail. Together with the ongoing measurement of the difference of CP asymmetries, $\Delta A_{CP} = A_{CP}(K^-K^+) - A_{CP}(\pi^-\pi^+)$, using the same data, a determination of $A_{CP}(\pi^-\pi^+)$ will be possible. These three measurements can then be used to improve the current world average values for mixing and CP violation parameters in the charm system [17].

Appendix A

Details of systematic studies

A.1 Alternative fit models

In this section, definitions of individual components of PDFs that are used for the systematic study presented in chapter 11.1 are given.

- The empirical Δm background model consisting out of a first order polynomial and an exponential part is given by:

$$\mathcal{P}_{bkg}(x|B,C,x_0) \propto B\left(\frac{x}{x_0}-1\right)+\left[1-exp\left(-\frac{x-x_0}{C}\right)\right], \tag{A.1}$$

  with x_0 parametrizing the threshold and B, C being two shape parameters.

- The Crystal Ball function used as an alternative signal model in the m_{D^+} distribution is given by:

$$\mathrm{CB}(x|x_0,\sigma,\alpha,n) \propto \begin{cases} \exp\left(-\frac{(x-x_0)^2}{2\sigma^2}\right) & \text{for } \frac{x-x_0}{\sigma} > -\alpha \\ A\cdot\left(B-\frac{x-x_0}{\sigma}\right)^{-n} & \text{for } \frac{x-x_0}{\sigma} \leq -\alpha \end{cases}, \tag{A.2}$$

  where

$$A = \left(\frac{n}{|\alpha|}\right)^n \exp\left(-\frac{|\alpha|^2}{2}\right), \tag{A.3}$$

$$B = \frac{n}{|\alpha|} - |\alpha|. \tag{A.4}$$

- A second order polynomial is used to describe the background in the m_{D^+} distribution. To ensure a stable performance, a parametrization via so called Chebyshev polynomials [48] is chosen:

$$\mathcal{P}_{bkg}(x|c,s) = c(2x^2-1)+sx+1. \tag{A.5}$$

  The parameters c and s represent the "curve" and "slope" of the function.

- For the description of background originating from $D^0 \to K^-\pi^+\pi^0$ in the Δm distribution, an empirical function consisting out of an exponential, a polynomial and a power law part is used together with a Gaussian distribution. This empirical function is a generalization of the one presented in equation A.1:

$$\mathcal{F}(x|A,B,C,x_0) \propto B\left(\frac{x}{x_0}-1\right)+\left[1-exp\left(-\frac{x-x_0}{C}\right)\right]\left(\frac{x}{x_0}\right)^A. \quad \text{(A.6)}$$

A.2 Fiducial requirements

In this section, the fiducial regions which are excluded as a systematic study presented in chapter 11.3 are given in detail.

- For the kaon in the channels $D^0 \to K^-\pi^+$ and $D^+ \to K^-\pi^+\pi^+$ the regions parametrized by:

$$\begin{aligned} p_z \geq 33\,\text{GeV}/c \wedge |p_x| \leq [5.2\,\text{GeV}/c + (p_z - 33\,\text{GeV}/c) * 4.8/31] \\ \wedge\, |p_x| \geq [3.5\,\text{GeV}/c + (p_z - 33\,\text{GeV}/c) * 6.5/53] \end{aligned} \quad \text{(A.7)}$$

  are excluded.

- For the pion in $D^0 \to K^-\pi^+$ decays and the low momentum pion in $D^+ \to K^-\pi^+\pi^+$ decays the regions parametrized by:

$$\begin{aligned} p_z \geq 33\,\text{GeV}/c \wedge |p_x| \leq [0.6\,\text{GeV}/c + (p_z - 33\,\text{GeV}/c) * 1.4/31] \\ \wedge\, |p_x| \geq 0.6\,\text{GeV}/c \end{aligned} \quad \text{(A.8)}$$

  and

$$|p_x| \geq (p_z - 2\,\text{GeV}/c) * 2/7 \quad \text{(A.9)}$$

  are excluded.

- For the pion in $D^+ \to \overline{K}^0\pi^+$ decays and the high momentum pion in $D^+ \to K^-\pi^+\pi^+$ decays the regions parametrized by:

$$\begin{aligned} p_z \geq 33\,\text{GeV}/c \wedge |p_x| \leq [4.9\,\text{GeV}/c + (p_z - 33\,\text{GeV}/c) * 5.1/31] \\ \wedge\, |p_x| \geq [3.2\,\text{GeV}/c + (p_z - 33\,\text{GeV}/c) * 6.8/53] \end{aligned} \quad \text{(A.10)}$$

  and

$$|p_x| \geq (p_z - 2\,\text{GeV}/c) * 1/3.6 \quad \text{(A.11)}$$

  are excluded.

Appendix B

Detailed fit results

In the following, the values obtained for the parameters of the maximum likelihood fit presented in chapter 7 and 10 are given. The definition of the parameters can be found in the section 7.2. Only the values for the fits to the weighted distributions are given.

Table B.1: Values for the parameters of the maximum likelihood fit to the four different data samples of the channel $D^0 \to K^-K^+$.

	Up 2011	**Down 2011**	**Up 2012**	**Down 2012**
N_{sig}	211620 ± 990	299820 ± 990	542200 ± 1300	561100 ± 1600
N_{bkg}	109500 ± 940	155330 ± 910	303300 ± 1200	318200 ± 1500
A_{raw}	-0.0160 ± 0.0024	0.0023 ± 0.0020	-0.0192 ± 0.0015	0.0009 ± 0.0015
A_{bkg}	-0.0212 ± 0.0035	0.0013 ± 0.0030	-0.0225 ± 0.0021	0.0007 ± 0.0021
μ_1^+	145.44334 ± 0.00095	145.44245 ± 0.00078	145.45042 ± 0.00061	145.44441 ± 0.00059
μ_1^-	145.44564 ± 0.00093	145.44538 ± 0.00078	145.44841 ± 0.00059	145.45076 ± 0.00059
μ_2^+	145.630 ± 0.044	145.600 ± 0.037	145.570 ± 0.020	145.580 ± 0.032
μ_2^-	145.529 ± 0.037	145.572 ± 0.037	145.585 ± 0.022	145.585 ± 0.032
ω	0.9899 ± 0.0053	1.0038 ± 0.0046	0.9905 ± 0.0034	1.0059 ± 0.0034
f_1	0.577 ± 0.020	0.571 ± 0.015	0.542 ± 0.013	0.557 ± 0.016
f_2	0.7979 ± 0.0091	0.8014 ± 0.0072	0.7851 ± 0.0052	0.7982 ± 0.0066
σ_1^+	0.1969 ± 0.0027	0.1924 ± 0.0020	0.1947 ± 0.0017	0.1945 ± 0.0020
σ_2^+	0.386 ± 0.013	0.3837 ± 0.0095	0.3755 ± 0.0072	0.381 ± 0.011
σ_3^+	1.150 ± 0.087	1.183 ± 0.064	1.127 ± 0.039	1.127 ± 0.067
A	0.644 ± 0.025	0.623 ± 0.015	0.640 ± 0.010	0.656 ± 0.011
B	0.0244 ± 0.0055	0.0187 ± 0.0033	0.0168 ± 0.0023	0.0217 ± 0.0025

Table B.2: Values for the parameters of the maximum likelihood fit to the four different data samples of the channel $D^0 \to K^-\pi^+$.

	Up 2011	**Down 2011**	**Up 2012**	**Down 2012**
N_{sig}	264550 ± 700	384110 ± 930	661670 ± 1000	740600 ± 1100
N_{bkg}	69400 ± 550	100340 ± 770	189270 ± 720	213730 ± 860
A_{raw}	-0.0278 ± 0.0020	-0.0128 ± 0.0017	-0.0224 ± 0.0013	-0.0138 ± 0.0012
A_{bkg}	-0.0290 ± 0.0045	-0.0237 ± 0.0037	-0.0357 ± 0.0027	-0.0190 ± 0.0025
μ_1^+	145.44990 ± 0.00085	145.44583 ± 0.00069	145.45689 ± 0.00054	145.44668 ± 0.00051
μ_1^-	145.44972 ± 0.00082	145.45003 ± 0.00068	145.45186 ± 0.00053	145.45604 ± 0.00050
μ_2^+	145.540 ± 0.021	145.550 ± 0.020	145.530 ± 0.015	145.520 ± 0.013
μ_2^-	145.547 ± 0.020	145.571 ± 0.020	145.570 ± 0.016	145.539 ± 0.013
ω	0.9891 ± 0.0044	1.0106 ± 0.0038	0.9927 ± 0.0027	1.0059 ± 0.0027
f_1	0.528 ± 0.021	0.564 ± 0.015	0.543 ± 0.014	0.523 ± 0.014
f_2	0.7997 ± 0.0070	0.8031 ± 0.0059	0.7941 ± 0.0048	0.7987 ± 0.0046
σ_1^+	0.1937 ± 0.0027	0.1951 ± 0.0019	0.1973 ± 0.0017	0.1927 ± 0.0017
σ_2^+	0.3607 ± 0.0093	0.3730 ± 0.0080	0.3703 ± 0.0072	0.3583 ± 0.0065
σ_3^+	1.000 ± 0.038	1.053 ± 0.040	1.029 ± 0.029	0.973 ± 0.026
A	0.652 ± 0.027	0.675 ± 0.025	0.6601 ± 0.0054	0.705 ± 0.011
B	0.0099 ± 0.0059	0.0136 ± 0.0054	0.0014 ± 0.0011	0.0144 ± 0.0023

Table B.3: Values for the parameters of the maximum likelihood fit to the four different data samples of the channel $D^+ \to K^-\pi^+\pi^+$.

	Up 2011	**Down 2011**	**Up 2012**	**Down 2012**
N_{sig}	632700 ± 930	903700 ± 1100	2383900 ± 1800	2481700 ± 1800
N_{bkg}	19240 ± 510	28750 ± 640	76930 ± 970	80770 ± 910
A_{raw}	-0.0235 ± 0.0013	-0.0158 ± 0.0011	-0.01470 ± 0.00067	-0.01916 ± 0.00065
A_{bkg}	-0.026 ± 0.012	-0.007 ± 0.010	-0.0075 ± 0.0062	-0.0071 ± 0.0060
μ^+	1869.469 ± 0.017	1869.403 ± 0.014	1869.3741 ± 0.0083	1869.2590 ± 0.0080
μ^-	1869.463 ± 0.016	1869.512 ± 0.014	1869.2999 ± 0.0081	1869.3889 ± 0.0079
ω	0.9944 ± 0.0024	0.9960 ± 0.0020	0.9935 ± 0.0013	0.9987 ± 0.0012
f_1	0.107 ± 0.015	0.1009 ± 0.0068	0.1029 ± 0.0036	0.0982 ± 0.0031
f_2	0.25 ± 0.17	0.435 ± 0.017	0.427 ± 0.010	0.410 ± 0.012
σ_1^+	5.42 ± 0.50	5.888 ± 0.045	5.868 ± 0.029	5.841 ± 0.033
σ_2^+	7.72 ± 0.37	8.166 ± 0.056	8.128 ± 0.033	8.100 ± 0.034
σ_L^+	15.82 ± 0.81	15.88 ± 0.51	15.92 ± 0.27	16.27 ± 0.25
σ_R^+	12.23 ± 0.25	11.85 ± 0.21	11.99 ± 0.12	12.21 ± 0.11
C	0.01032 ± 0.00058	0.01000 ± 0.00038	0.01009 ± 0.00022	0.00993 ± 0.00021

Table B.4: Values for the parameters of the maximum likelihood fit to the four different data samples of the channel $D^+ \to \overline{K}^0\pi^+$.

	Up 2011	**Down 2011**	**Up 2012**	**Down 2012**
N_{sig}	107880 ± 460	159440 ± 590	363210 ± 760	366600 ± 750
N_{bkg}	10670 ± 340	13290 ± 460	50480 ± 520	48860 ± 490
A_{raw}	-0.0153 ± 0.0033	-0.0074 ± 0.0027	-0.0105 ± 0.0018	-0.0048 ± 0.0018
A_{bkg}	0.020 ± 0.016	-0.009 ± 0.015	0.0131 ± 0.0068	0.0169 ± 0.0070
μ^+	1869.314 ± 0.043	1869.169 ± 0.033	1869.282 ± 0.023	1869.170 ± 0.058
μ^-	1869.323 ± 0.042	1869.309 ± 0.033	1869.230 ± 0.023	1869.269 ± 0.058
ω	1.0054 ± 0.0062	1.0012 ± 0.0052	0.9958 ± 0.0036	1.0012 ± 0.0035
f_1	0.142 ± 0.037	0.090 ± 0.013	0.228 ± 0.014	0.0323 ± 0.0063
f_2	0.087 ± 0.056	0.469 ± 0.050	0.31 ± 0.16	0.5994 ± 0.0025
σ_1^+	4.48 ± 0.71	6.39 ± 0.13	6.17 ± 0.27	6.474 ± 0.052
σ_2^+	7.68 ± 0.27	8.83 ± 0.23	7.37 ± 0.18	10.139 ± 0.060
σ_L^+	14.9 ± 1.5	19.8 ± 1.7	12.70 ± 0.33	22.0 ± 1.4
σ_R^+	13.02 ± 0.98	15.35 ± 0.79	11.31 ± 0.24	6.7 ± 3.7
C	0.00491 ± 0.00051	0.00279 ± 0.00064	0.00335 ± 0.00019	0.00226 ± 0.00026

Appendix C

${}_S$*Plot* technique

The ${}_S$*Plot* technique [39] is a method to statistically unfold the signal and background distribution ($f_S(x)$ and $f_B(x)$) in a given variable x. For this purpose, no knowledge on the shape of these distributions is necessary. Instead, the distributions ($f_S(y)$ and $f_B(y)$) in an additional discriminating variable y are used. The exact shape and yield of the signal and background distribution in the variable y is obtained by a maximum likelihood fit. If the two variables x and y are uncorrelated, the two-dimensional density function can be written as:

$$f_{tot}(x,y) = N_S f_S(x) f_S(x) + N_{bkg} f_B(x) f_B(x), \tag{C.1}$$

where N_S and N_B are the signal and background yield. The aim of the ${}_S$*Plot* technique is to find a weighting distribution $w(y)$ which projects out the signal distribution in the variable x:

$$N_{sig} f_S(x) = \int w(y) f_{tot}(x,y) \mathrm{d}y. \tag{C.2}$$

This means, that $w(y)$ has to be orthogonal to $f_B(y)$ and not orthogonal to $f_S(y)$. The function given by:

$$w(y) = \frac{V_{SS} f_S(y) + V_{SB} f_B(y)}{N_S f_S(y) + N_B f_B(y)}, \tag{C.3}$$

fulfills this requirement and additionally ensures a minimal statistic uncertainty. The parameters V_{ij} are obtained by inverting the matrix given by a sum over the data sample:

$$V_{ij}^{-1} = \sum_{n=1}^{N} \frac{f_i(y_n) f_j(y_n)}{[N_S f_S(y_n) + N_B f_B(y_n)]^2}. \tag{C.4}$$

In principle, the variable x can be multidimensional and the method can, therefore, simultaneously unfold signal and background distributions in several variables.

In the scope of this analysis, the ${}_S$*Plot* technique is predominantly used in order to obtain the signal distributions in several kinematic variables. These distributions are essential for the weighting procedure presented in chapter 8. The mass difference Δm in the case of D^{*+} decays, and the mass of the D^+ meson in the case of D^+ decays are used as discriminating variables x.

Appendix D

Run block definitions

For a consistency check, the analysis was performed independently in bins of the run number, see chapter 10.3. The data taken in 2011 is split in four bins given by the run numbers [87000, 91000, 95000, 101000, 105000]. For the year 2012 six bins are chosen which are specified by the run numbers [111000, 117200, 119000, 125200, 129000, 131000, 135000].

As a second consistency check, the same was done using the kinematic weights of the default analysis. For this purpose the data was split in 56 finer bins which are given by the numbers shown in table D.1.

Table D.1: Definition of run blocks used as a consistency check.

Run block	Run number period	Run block	Run number period
1	87665-90569	29	103391-103556
2	90569-92063	30	103586-103863
3	92063-92560	31	103936-104037
4	92560-92840	32	111440-113150
5	92840-93050	33	114200-114290
6	93050-93166	34	114310-115470
7	93166-93415	35	115510-116195
8	93415-93564	36	116210-117110
9	93564-93993	37	117185-117570
10	93993-94294	38	117620-118295
11	94294-95000	39	118320-118885
12	96214-96642	40	119950-120800
13	96740-97028	41	121705-123803
14	97114-97789	42	123905-124390
15	97805-98002	43	124400-125120
16	98019-98174	44	125560-126215
17	98187-98332	45	126230-126685
18	98369-98656	46	126820-127165
19	98900-100256	47	127185-128115
20	101373-101643	48	128405-128500
21	101665-101862	49	129530-129985
22	101891-102092	50	130310-130645
23	102039-102269	51	130650-130870
24	102291-102452	52	130905-131374
25	102499-102772	53	131375-131945
26	102788-102907	54	131965-132640
27	103031-103186	55	132845-133595
28	103203-103379	56	133615-133790

Bibliography

[1] ATLAS, G. Aad *et al.*, *Observation of a new particle in the search for the Standard Model Higgs boson with the ATLAS detector at the LHC*, Phys. Lett. **B716** (2012) 1, arXiv:1207.7214.

[2] CMS, S. Chatrchyan *et al.*, *Observation of a new boson at a mass of 125 GeV with the CMS experiment at the LHC*, Phys. Lett. **B716** (2012) 30, arXiv:1207.7235.

[3] LHCb, R. Aaij *et al.*, *Evidence for CP violation in time-integrated $D^0 \to h^- h^+$ decay rates*, Phys. Rev. Lett. **108** (2012) 111602, arXiv:1112.0938.

[4] LHCb, R. Aaij *et al.*, *Measurement of CP asymmetry in $D^0 \to K^- K^+$ and $D^0 \to \pi^- \pi^+$ decays*, JHEP **07** (2014) 041, arXiv:1405.2797.

[5] S. Stahl, *Measurement of CP asymmetry in muon-tagged $D^0 \to K^- K^+$ and $D^0 \to \pi^- \pi^+$ decays at LHCb*, ph.d. thesis, Universität Heidelberg, 2014.

[6] G. ALTARELLI, *The Standard model of particle physics*, arXiv:hep-ph/0510281.

[7] Wikipedia, *Standard model of elementary particles*, 2006. URL: https://upload.wikimedia.org/wikipedia/commons/0/00/Standard_Model_of_Elementary_Particles.svg, last visited on 08/08/2015.

[8] LHCb, R. Aaij *et al.*, *Observation of $J/\Psi p$ Resonances Consistent with Pentaquark States in $\Lambda_b^0 \to J/\Psi K^- p$ Decays*, Phys. Rev. Lett. **115** (2015), no. 7 072001, arXiv:1507.0341.

[9] LHCb, R. Aaij *et al.*, *Observation of the resonant character of the $Z(4430)^-$ state*, Phys. Rev. Lett. **112** (2014), no. 22 222002, arXiv:1404.1903.

[10] Planck, P. Ade *et al.*, *Planck 2015 results. XIII. Cosmological parameters*, arXiv:1502.0158.

[11] Particle Data Group, K. A. Olive *et al.*, *Review of Particle Physics*, Chin. Phys. **C38** (2014) 090001.

[12] M. Kobayashi and T. Maskawa, *CP Violation in the Renormalizable Theory of Weak Interaction*, Prog. Theor. Phys. **49** (1973) 652.

[13] L. Wolfenstein, *Parametrization of the Kobayashi-Maskawa Matrix*, Physical Review Letters **51** (1983) 1945.

[14] S. L. Glashow, J. Iliopoulos, and L. Maiani, *Weak interactions with lepton-hadron symmetry*, Phys. Rev. D **2** (1970) 1285.

[15] P. Kooijman and N. Tuning, *Lectures on cp violation*, URL: http://www.nikhef.nl/ h71/Lectures/2015/ppII-cpviolation-29012015.pdf, last visited on 09/08/2015.

[16] U. Nierste, *Three Lectures on Meson Mixing and CKM phenomenology*, in *Heavy quark physics. Proceedings, Helmholtz International School, HQP08, Dubna, Russia, August 11-21, 2008*, pp. 1–38, 2009. arXiv:0904.1869.

[17] Heavy Flavor Averaging Group (HFAG), Y. Amhis *et al.*, *Averages of b-hadron, c-hadron, and τ-lepton properties as of summer 2014, and online update*, arXiv:1412.7515.

[18] M. Gersabeck, *Brief Review of Charm Physics*, Mod. Phys. Lett. **A27** (2012) 1230026, arXiv:1207.2195.

[19] Heavy Flavor Averaging Group, Y. Amhis *et al.*, *Averages of B-Hadron, C-Hadron, and tau-lepton properties as of early 2012*, arXiv:1207.1158.

[20] L. Evans and P. Bryant, *Lhc machine*, Journal of Instrumentation **3** (2008), no. 08 S08001.

[21] ALICE, K. Aamodt *et al.*, *The ALICE experiment at the CERN LHC*, JINST **3** (2008) S08002.

[22] ATLAS, G. Aad *et al.*, *The ATLAS Experiment at the CERN Large Hadron Collider*, JINST **3** (2008) S08003.

[23] CMS, S. Chatrchyan *et al.*, *The CMS experiment at the CERN LHC*, JINST **3** (2008) S08004.

[24] LHCb, A. A. Alves, Jr. *et al.*, *The LHCb Detector at the LHC*, JINST **3** (2008) S08005.

[25] LHCb, *Lhcb webpage*, URL: http://lhcb.web.cern.ch/lhcb/ speakersbureau/html/Material_for_Presentations.html, last visited on 17/08/2015.

[26] LHCb, R. Antunes-Nobrega *et al.*, *LHCb reoptimized detector design and performance: Technical Design Report*, Technical Design Report LHCb, CERN, Geneva, 2003.

[27] J. Luisier, *Performance of LHCb Silicon Tracker Detector in the LHC*, Physics Procedia **37** (2012) 851 , Proceedings of the 2nd International Conference on Technology and Instrumentation in Particle Physics (TIPP 2011).

[28] E. R. Cazaroto, V. P. Goncalves, F. S. Navarra, and M. Nielsen, *Charm production asymmetry at the lhc*, Journal of Physics: Conference Series **458** (2013), no. 1 012014.

[29] LHCb, R. Aaij *et al.*, *Measurement of the $D^{+/-}$ production asymmetry in 7 TeV pp collisions*, Phys. Lett. **B718** (2013) 902, arXiv:1210.4112.

[30] E. Norrbin, *Heavy quark production asymmetries*, in *Proceedings, International Europhysics Conference on High energy physics (EPS-HEP 1999)*, pp. 408–410, 1999. arXiv:hep-ph/9909437.

[31] LHCb, R. Aaij *et al.*, *Measurement of the D_s^+ - D_s^- production asymmetry in 7 TeV pp collisions*, Phys. Lett. **B713** (2012) 186, arXiv:1205.0897.

[32] M. Gersabeck and M. Alexander, *Measurement of the charm mixing and CP violation parameter y_{CP} with 2011 data*, 2014. Linked to LHCb-ANA-2014-016.

[33] J. Brehmer, J. Albrecht, and P. Seyfert, *Ghost probability: an efficient tool to remove background tracks*, Tech. Rep. CERN-LHCb-INT-2012-025, CERN, Geneva, 2012.

[34] W. D. Hulsbergen, *Decay chain fitting with a Kalman filter*, Nuclear Instruments and Methods in Physics Research A **552** (2005) 566, arXiv:physics/0503191.

[35] LHCb, *A search for time-integrated CP violation in $D^0 \to K^-K^+$ and $D^0 \to \pi^-\pi^+$ decays*, 2013. Linked to LHCb-ANA-2012-034.

[36] V. Blobel and E. Lohrmann, *Statistische und numerische Methoden der Datenanalyse*, Teubner Studienbücher Physik, Teubner Verlag, Stuttgart, 1998.

[37] LHCb, R. Aaij *et al.*, *Measurement of the time-integrated CP asymmetry in $D^0 \to K^0_S K^0_S$ decays*, arXiv:1508.0608.

[38] S. Amato *et al.*, *Charge asymmetries induced by PID*, no. CERN-LHCb-INT-2014-049, Geneva, 2014.

[39] M. Pivk and F. R. Le Diberder, *${}_S$Plots: A statistical tool to unfold data distributions*, Nuclear Instruments and Methods in Physics Research A **555** (2005) 356, arXiv:physics/0402083.

[40] J. H. Christenson, J. W. Cronin, V. L. Fitch, and R. Turlay, *Evidence for the 2π decay of the k_2^0 meson*, Phys. Rev. Lett. **13** (1964) 138.

[41] T. Skwarnicki, *A study of the radiative CASCADE transitions between the Upsilon-Prime and Upsilon resonances*, PhD thesis, Cracow, INP, 1986.

[42] A. Carbone, V. Vagnoni, M. Charles, and G. Wilkinson, *Search for time-integrated CP violation in $D^0 \to K^-K^+, \pi^-\pi^+$ in the 2011 data*, 2012. Linked to LHCb-ANA-2011-010.

[43] T. Bauer *et al.*, *Prompt charm production in pp collisions at $\sqrt{s} = 7\ TeV$ in 2010 data*, 2011. Linked to LHCb-ANA-2011-018.

[44] LHCb, R. Aaij *et al.*, *Measurement of B meson production cross-sections in proton-proton collisions at $\sqrt{s} = 7\ TeV$*, JHEP **08** (2013) 117, arXiv:1306.3663.

[45] CMS, S. Chatrchyan *et al.*, *Measurement of the Λ_b cross section and the $\bar{\Lambda}_b$ to Λ_b ratio with $J/\Psi\Lambda$ decays in pp collisions at $\sqrt{s} = 7\ TeV$*, Phys. Lett. **B714** (2012) 136, arXiv:1205.0594.

[46] LHCb, R. Aaij *et al.*, *Measurement of the semileptonic CP asymmetry in $B^0 - \overline{B}^0$ mixing*, Phys. Rev. Lett. **114** (2015) 041601, arXiv:1409.8586.

[47] LHCb, R. Aaij *et al.*, *Measurement of the $\overline{B}^0 - B^0$ and $\overline{B}^0_s - B^0_s$ production asymmetries in pp collisions at $\sqrt{s} = 7\ TeV$*, Phys. Lett. **B739** (2014) 218, arXiv:1408.0275.

[48] E. W. Weisstein, *Chebyshev polynomial of the first kind. From MathWorld—A Wolfram Web Resource*, URL: http://mathworld.wolfram.com/ChebyshevPolynomialoftheFirstKind.html, last visited on 30/7/2015.

Erklärung

Ich versichere, dass ich diese Arbeit selbstständig verfasst habe und keine anderen als die angegebenen Quellen und Hilfsmittel benutzt habe.

Heidelberg, den 29.09.2015 .....